OUKA
The University of Osaka
Institutional Knowledge Archive

Title	Numerical study of flow instability and pattern evolution induced by Marangoni convection in a shallow rectangular cavity and half-zone with various geometrical conditions
Author(s)	Weerakoon Rathnayake, Neranjan Nayanajith
Citation	大阪大学, 2025, 博士論文
Version Type	VoR
URL	https://doi.org/10.18910/101496
rights	
Note	

The University of Osaka Institutional Knowledge Archive : OUKA

https://ir.library.osaka-u.ac.jp/

The University of Osaka

Numerical study of flow instability and pattern evolution induced by Marangoni convection in a shallow rectangular cavity and half-zone with various geometrical conditions

Neranjan Nayanajith Weerakoon Rathnayake

JANUARY 2025

Numerical study of flow instability and pattern evolution induced by Marangoni convection in a shallow rectangular cavity and half-zone with various geometrical conditions

A dissertation submitted to

THE GRADUATE SCHOOL OF ENGINEERING SCIENCE

OSAKA UNIVERSITY

in partial fulfillment of the requirements for the degree of

DOCTOR OF PHILOSOPHY IN ENGINEERING

BY

Neranjan Nayanajith Weerakoon Rathnayake

JANUARY 2025

ABSTRACT

Marangoni convection is critical in various natural and industrial processes, such as film coating, droplets, material fabrication, and crystal growth. However, most of these studies have focused on fixed geometrical settings, neglecting the variability encountered in real-world scenarios. This thesis aims to fill this gap by investigating Marangoni convection under various geometrical conditions relevant to practical processes. It strives to uncover and characterize the novel phenomena that arise when the geometric constraints are altered. Through meticulous numerical simulations and experimental analysis, this research offers a fresh perspective on the complexities of Marangoni convection, providing insights that could revolutionize process optimization in fields where these dynamics are crucial.

Investigating the impact of liquid depth on thermal Marangoni convection stability within a shallow cavity containing silicone oil with a Prandtl number of 6.7, the findings reveal that thinner films exhibit primary instability transitioning from a steady state to a 3D oscillatory pattern. In comparison, thicker films experience secondary instability, shifting from oscillatory to chaotic flow. These behaviors suggest that thinner films benefit applications requiring stable coating processes. In contrast, thicker films might be better suited for applications demanding enhanced mixing, such as lubrication.

The next research delves into the influence of hydro-static free surface deformation on thermo-solutal Marangoni convection in a shallow rectangular cavity under microgravity conditions. The results underscore a crucial point: the volume ratio is a dominant factor for promoting uniform liquid layers and is facilitated by consistent Marangoni flow distribution. This study also explores the interaction between different Prandtl and Schmidt numbers, demonstrating how these properties affect flow, temperature, and concentration distributions, essential for optimizing various industrial processes such as material welding, glass

production, painting, and crystal growth. This emphasis on practical relevance keeps the reader's attention and highlights the importance of the research.

This final investigation focuses on thermo-solutal Marangoni convection in a floating liquid bridge of SiGe, considering variations in volume ratio and gravity. The simulation outcomes indicate that the temperature field in the melt remains unaffected mainly by convective flows, while the concentration field predominantly determines the transport structures. Notably, the transition characteristics and the critical azimuthal wave number are influenced by the volume ratio, with minimal impact from gravitational changes, highlighting the robustness of Marangoni convection under diverse conditions.

These studies offer a deeper understanding of Marangoni convection's complex dynamics and highlight its direct implications for improving processes in various industrial and scientific applications, coating, lubrication, and crystal growth for better design and high-quality production.

CONTENTS

CHAPTER 1

INTRODUCTION

1.1 Background

Marangoni convection usually occurs in a liquid layer due to the spatial variation of surface tension. When the temperature gradient causes the variation in surface tension, the flow in the liquid is called thermal Marangoni convection. Analogous to the thermal Marangoni effect, when the concentration gradient causes it, the flow is called solutal Marangoni convection. The combined flow is called thermo-solutal Marangoni convection in the presence of both temperature and concentration gradients. Due to its complex dynamic behaviors and flow pattern transitions, Marangoni convection is critical for understanding various natural phenomena and industrial processes. This convection is essential in explaining natural occurrences like droplet evaporation [1] and the formation of wine tears [2] and in enhancing theoretical knowledge in industrial applications, including thin-film coating [3, 4], casting solidification [5, 6], and crystal growth [7, 8]. The phenomenon primarily arises along free surfaces, driven by variations in surface tension and influenced by free surface conditions such as the deformation of a crystal's growing surface (Figure 1.1) due to hydrostatic pressure during forced convection [9, 10]. These Marangoni flows, although typically confined to different regions of the melt, exhibit significant interactions, necessitating a more profound exploration to improve both theoretical understanding and practical applications in related fields.

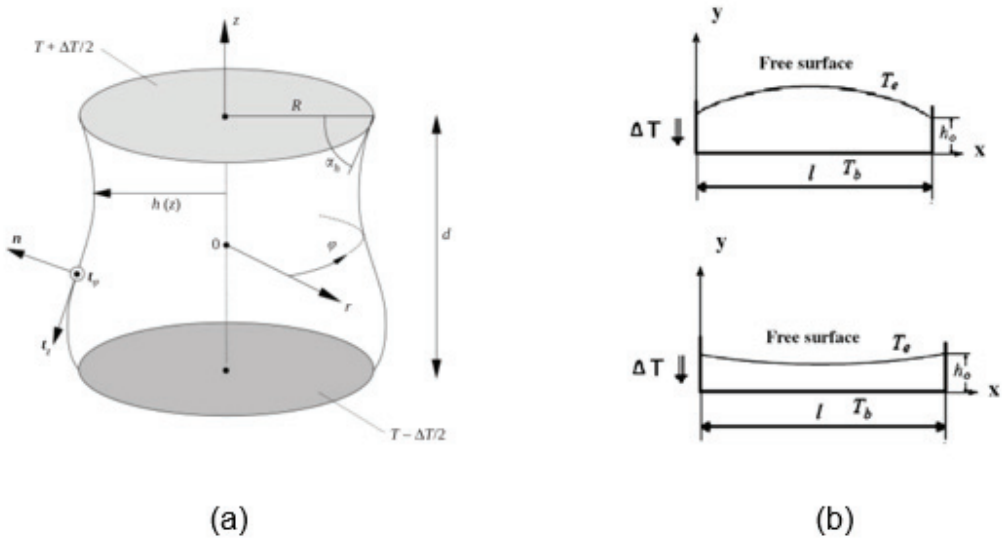

Figure 1.1 (a) 3D Geometry of the liquid bridge with deformed free surface [9] and (b) 2D sketch of liquid layer with curved free surface [45].

1.2 Relevant research and status

Marangoni convection has seen a resurgence of interest due to advancements in space experiment conditions over the past four decades, highlighted by theoretical, experimental, and numerical studies that have elucidated critical parameters influencing flow pattern transitions, bifurcation laws, and structural influences on flow dynamics. In parallel, the shallow rectangular cavity system remains a cornerstone in material welding, glass production, painting, and crystal growth (Figure 1.2 (a)), offering precise control over the growth of thin liquid layers through adjustments in temperature, solution composition, and substrate preparation [11]. Despite its advantages in material customization, complete mastery over the thin fluid layer relationships in industrial applications continues to be elusive, promoting numerical simulations under micro- or zero-gravity conditions as cost-effective methods for in-depth study.

Similarly, the Floating Zone (FZ) technique (Figure 1.2 (b)), which allows for the growth of high-purity crystals without containment, faces challenges due to the high melting points of

materials and limitations in direct observation, compounded by gravitational constraints that limit the size of the crystals grown on Earth. Here, numerical simulations, particularly those employing the half zone model for its computational efficiency, also serve as valuable tools. This model, which simplifies the system to half of a full zone liquid bridge, features a single toroidal vortex between hot and cold zones, enabling a detailed study of the growth processes under varied gravitational conditions [12]. These simulations are instrumental in overcoming practical and experimental limitations, allowing for expanded exploration of thin film applications and FZ techniques.

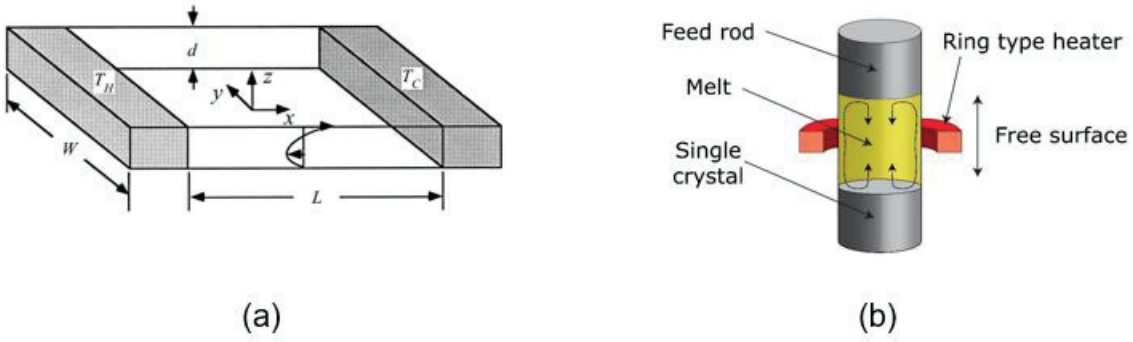

Figure 1.2 (a) Schematic diagram of the shallow rectangular cavity used for thin film application and (b) floating zone method.

1.2.1 Study on pure thermal Marangoni convection

Numerous studies have investigated pure thermal Marangoni convection due to its widespread presence in natural and industrial processes. In an earlier study, Smith and Davis [13] conducted a linear stability analysis of thermal Marangoni convection in an infinitely shallow liquid layer subjected to a horizontal temperature gradient. They identified two types of thermal convection instabilities in the liquid, specifically stationary longitudinal rolls, and oblique hydrothermal waves (HTW), which depend on the working liquid's Prandtl number (*Pr*) and the basic flow pattern. They also determined the corresponding critical Marangoni

number. Subsequent experimental studies also observed stationary longitudinal rolls and HTW.

Li *et al*. [14, 15] performed three-dimensional numerical simulations of thermal Marangoni convection and Marangoni-buoyancy convection in silicon melt and 0.65cSt silicone oil within an annular liquid pool. Their results indicated that the basic flow bifurcates into a three-dimensional steady flow and then transitions into a three-dimensional oscillatory flow as the temperature difference increases. These simulation results were largely consistent with the experimental findings of Azami *et al*. [16] and Schwabe [17]. Burguete *et al*. [18, 19] experimentally investigated natural and thermal Marangoni convection in a rectangular pool and found that Marangoni convection was dominant in a shallow pool, while buoyancy effects were more significant in a deeper pool.

The fluid's properties and the configuration's aspect ratios significantly impact thermal Marangoni convection. Schwabe *et al*. [20, 21] conducted microgravity experiments and numerical simulations to explore thermal Marangoni convection flow characteristics and stability in a cylindrical annulus under various aspect ratios. They verified that the axisymmetric flow disappears and becomes an oscillatory flow with a multi-roll structure when the imposed temperature gradient exceeds a critical value. Additionally, the aspect ratio significantly affects the critical Marangoni number, with the number of azimuthal waves and multicells generally increasing with the aspect ratio. Using linear stability analysis, Liu *et al*. [22] studied the effect of aspect ratio on the instabilities of thermal Marangoni flow. Their results showed that the bifurcation is oscillatory for small aspect ratios, while a stationary bifurcation mode arises for large aspect ratios, revealing different instability mechanisms for each bifurcation mode. Zhang *et al*. [23] conducted numerical simulations to investigate the critical condition for flow destabilization in thermal Marangoni flow at two different aspect ratios, finding that flow loses stability more easily at smaller aspect ratios, and more wave numbers are observed in the oscillatory flow. Liu *et al*. [24] focused on the effect of the Prandtl number ($0.001 > Pr > 6.7$) on thermal Marangoni flow in an annular pool using linear stability analysis, observing five types of instabilities, and systematically discussing the

relationships among the Prandtl number, wave number, and associated instability mechanisms.

Imaishi *et al*. [25] predicted flow bifurcations with increasing temperature differences in a liquid bridge at smaller Prandtl numbers. Li *et al*. [26] investigated three types of oscillatory Marangoni flows in half-zone liquid bridges of low-*Pr* fluids using proper orthogonal decomposition (POD) with the snapshot method, identifying oscillatory disturbances with characteristic eigenfunctions. Li *et al*. [27] also studied changes in the oscillation mode through time evolutions of thermocapillary flows in a short half-zone of molten tin with a low *Pr* number.

1.2.2 Study on thermo-solutal Marangoni convection

Thermal-solutal Marangoni flow, which is complex due to the coupling of thermal and solutal Marangoni effects, is crucial in thin film applications and crystal growth processes. Bergman [28] investigated this phenomenon in a rectangular cavity with opposing, equal-strength thermal and solutal effects, finding that flow occurs and loses stability when the Marangoni number exceeds a critical value despite a zero overall effect. However, the transition mechanism was not detailed. Arafune *et al.* [29–31] used experiments and simulations to study thermal and solutal Marangoni convection in an In–Ga–Sb system, predicting that solutal Marangoni convection could enhance or weaken thermal convection, affecting crystal growth uniformity. Okano *et al.* [32, 33] identified thermal-solutal Marangoni effects as causing oscillatory flow in GaSb/InSb/GaSb alloys, potentially degrading crystal quality. Sheremet and Pop [34] found that strong Marangoni effects reduce heat transfer in a nanofluid-filled porous cavity. Chen et al. [35] analyzed thermal-solutal Marangoni flow in a two-dimensional rectangular cavity, finding that instability transitions to oscillatory flow via Hopf bifurcation, influenced by Lewis and Prandtl numbers. Zhan *et al.* [36] studied three-dimensional thermal-solutal Marangoni convection in a cubic cavity, noting the significant impacts of the Marangoni ratio on heat/mass transfer and flow structures, with transitions from oscillatory to chaotic patterns at higher ratios. Yu *et al*. [37,

38] examined Marangoni convection in an annular pool, highlighting the Marangoni ratio's influence on wave pattern evolution. Agampodi Mendis *et al.* [39] investigated aspect ratio effects on Marangoni instabilities in a liquid bridge, linking critical Marangoni numbers to wave numbers and aspect ratios. Given the dual effects' impact on melt flow and crystal quality, ongoing research focuses on thermal and solutal Marangoni convection in floating zones and rectangular cavities. Mendis *et al.* [40, 41] conducted global linear stability analyses to determine the onset and transition of Marangoni convection in a half-zone liquid bridge. Furthermore, the SiGe growth melt temperature and concentration gradients arise from the density difference between Si and Ge, driven by the applied temperature gradient. These factors collectively influence the development of thermal and solutal Marangoni flows along the free surface of the liquid bridge. Minakuchi *et al*. [42, 43] investigated the relative contributions of thermal and solutal Marangoni convection in the same direction in a half-zone system under zero gravity through numerical simulation. They demonstrated that the co-existence of these two flows significantly affects the flow pattern and azimuthal wave number (m). Augmented effects with m-fold symmetry and an oscillatory rotating tendency were predominantly observed at large Marangoni numbers. Minakuchi *et al*. [44] also conducted a numerical investigation on the hysteresis phenomenon of flow patterns induced by thermal and solutal Marangoni convection in a half-zone system under zero gravity. They found that the hysteresis behavior of the flow field showed about a 24% difference between critical values in the hysteresis diagram. These results and findings are based on the assumption of the same flow direction for both thermal and solutal Marangoni convection.

Past numerical simulations have predominantly explored the effects of thermal-solutal Marangoni flows in liquid bridges and rectangular cavities assuming an undeformed free surface. It must be pointed out that most studies mentioned above considered only the cases of thermal and concentration gradients in a rectangular cavity and liquid bridge. To our knowledge, the case of a deformed free surface has not been considered yet. It would be interesting to investigate since it occurs in some crystal growth processes and thin film applications such as floating zone method, painting and drying.

1.2.3 Effect of free surface deformation on pure thermal Marangoni convection in thin liquid layer

Marangoni convection, driven by variations in surface tension due to temperature and/or concentration gradients across a liquid's free surface, has attracted considerable attention because of its complex dynamic behaviors and the transition of its flow patterns, as noted in studies by Zebib *et al*. [56], Sen and Davis [54], and Zhang *et al*. [63]. Research into these flow patterns is crucial for understanding natural phenomena such as oceanic circulation [46] and the formation of wine tears [47]. Moreover, exploring Marangoni convection involving free surface deformation deepens our comprehension of the fundamental principles vital for numerous industrial uses, such as in the production of thin films [48], solidification in casting and ingots [57], and crystal growth [49, 61]. A thorough understanding of Marangoni convection's evolution under varying free surface configurations is crucial for optimizing these industrial processes.

Smith and Davis [13] investigated thermal Marangoni convection in an infinitely shallow liquid layer with a horizontal temperature gradient. They identified two types of convection instabilities based on the liquid Prandtl number (*Pr*), pinpointing the critical Marangoni numbers for these instabilities [19]. They studied natural and thermal Marangoni convections experimentally in a rectangular pool, noting that Marangoni effects are dominant in shallow pools while buoyancy becomes significant in deeper ones. Xu and Zebib [51] also conducted numerical simulations to assess thermal Marangoni convection flow characteristics and stability. Zhang *et al*. [23] carried out three-dimensional numerical simulations to explore how liquid heat dissipation affects the stability of thermal Marangoni convection, focusing on the mechanisms of instability. Rosenblat *et al*. [52] investigated thermal Marangoni convection in liquid layers with different aspect ratios, examining the effects of lateral slippery boundary conditions and identifying conditions under which time-periodic convection occurs. Schwabe *et al*. [20] and Sim *et al*. [21] used microgravity experiments and numerical simulations to study the flow dynamics and stability of thermal Marangoni convection in a cylindrical annulus, finding that axisymmetric flow shifts to oscillatory flow with multi-roll structures as the temperature gradient surpasses a critical threshold. They also

observed that aspect ratios heavily influence the critical Marangoni number, with larger ratios fostering more azimuthal waves and multi-cells. Ueno *et al*. [59] explored the complete transition from steady to unsteady flow regimes by examining the post-destabilization flow structures via suspended particle motion. Liu *et al*. [24] analyzed the effect of the Prandtl number ($0.001 < Pr < 6.7$) on thermal Marangoni flow within an annular pool, identifying five distinct flow instabilities and exploring the relationships between the Prandtl number, wave number, and instability mechanisms, thus enriching the understanding of thermal Marangoni convection behavior under various experimental conditions. These studies collectively focus on the simple geometries of thermal Marangoni flow, establishing it as a preferred model for researchers investigating the complex interactions between fluid mechanics and heat transfer on a deforming free surface.

Most of the referenced studies have focused primarily on pure thermal Marangoni flow. Yet, the more intricate thermo-solutal Marangoni flow, which encompasses the combined effects of thermal and solutal factors, is also crucial and finds relevance in critical applications like thin film coating and crystal growth. Bergman [28] delved into thermo-solutal Marangoni convection within a rectangular cavity, specifically exploring scenarios where thermal and solutal influences counteracted each other equally. His findings indicated that flow would commence and destabilize once the Marangoni number exceeded a certain critical level, even though the net Marangoni effect was neutral; however, the study could have provided a more thorough exploration of the mechanisms driving observed flow pattern transitions. Arafune and Hirata [30] and Arafune *et al*. [31] conducted experiments and simulations to assess the joint effects of thermal and solutal Marangoni convections in an In–Ga–Sb system, observing that solutal Marangoni convection can either mitigate or enhance thermal Marangoni convection, thereby affecting application uniformity. Chen *et al*. [35] studied the onset of both steady and oscillatory flows in double-diffusive Marangoni convection, focusing on conditions where thermal and solutal effects were in equilibrium. Their research particularly addressed the impacts of the Lewis number, the Prandtl number, and the aspect ratio on flow stability. Likewise, Li *et al*. [60] investigated the transitions to chaotic flow in double-diffusive Marangoni convection within a rectangular cavity under horizontal temperature and

concentration gradients. Zhan *et al*. [36] performed a numerical analysis of three-dimensional double-diffusive Marangoni convection in a cubic cavity with both temperature and solute concentration gradients applied horizontally, discussing how the capillary Reynolds number, the ratio of solutal to thermal Marangoni numbers and the Lewis number affect the flow regime. Moreover, Chen and Chan [64] explored the stability of double-diffusive Marangoni convection in a horizontal fluid layer driven by the combined effects of buoyancy and surface tension, underscoring the complex interactions that govern flow stability in these systems.

Zhang *et al*., [89] executed three-dimensional (3D) numerical analyses to investigate the dynamics of thermal-solutal Marangoni convection on a flat free surface within a shallow cavity. Our current study aims to deepen the physical understanding of Marangoni convection when the free surface is deformed in a shallow cavity, recognizing the importance of free surface configurations in the context of the floating zone [49]. It is important to note that previous studies typically focus on thermo-solutal Marangoni convection without considering free surface or interface deformation, simplifying the modelling process by avoiding the complexities associated with undefined surface shapes. However, this simplification might exclude vital dynamics associated with surface deformation. Thus, a numerical simulation incorporating surface deformation is essential to capture these critical dynamics fully.

The influence of free surface or interface deformation is critical in the dynamics of pure thermocapillary and Marangoni convection, particularly in initiating oscillatory flows. A microgravity experiment by Koster [50] emphasized the need for comprehensive studies on thermocapillary convection in multilayered fluid systems, accounting for finite interface deformations and dynamic contact line conditions. Additionally, several researchers [91, 92] have included the impact of free surface or interface deformation in their numerical simulations of pure thermocapillary convection, highlighting its importance in accurate modelling. Anthony and Clint [53] investigated the effects of surface temperature gradients and, in their analysis, omitted inertia terms in the Navier-Stokes equations. Their results indicated that changes in interface height between two points on the free surface directly

correlate with the temperature differences between these points. Sen and Davis [54] used an asymptotic method to study steady thermocapillary flows in a shallow, two-dimensional slot, focusing on slight deviations from a flat interface. Their findings apply to situations with small deviations in interface shape and are relevant in settings with small aspect ratios, Marangoni numbers, and thermocapillary Reynolds numbers. Chen *et al.* [10] analyzed steady-state free surface flows with mild curvature in configurations with small aspect ratios, using a boundary-fitted curvilinear coordinate system for their studies. Pimputkar and Ostrach [55] considered free surface deformation in their transient analyses of thin liquid layers, disregarding pressure effects due to surface curvature resulting from the small geometry aspect ratio. Zebib *et al*. [56] applied a domain perturbation method to determine interface shapes at very low Capillary numbers by examining high Marangoni convection within a square cavity. Lastly, Cuvelicr and Driessen [57] conducted steady-state analyses of two-dimensional thermocapillary flows, calculating the free surface shape through three different iterative methods within a finite element framework.

Many studies have utilized two-dimensional (2D) numerical simulations to examine steady thermal Marangoni convection, particularly in scenarios involving deformed free surfaces in thin fluid layers. Therefore, incorporating three-dimensional numerical simulations is essential to enhance understanding and offer deeper insights into the related topics.

Yamamoto *et al*. [58] conducted 3D numerical simulations and underscored the significant impact of water film geometry on the direction and intensity of thermal Marangoni flows. This study emphasized how the curvature of the liquid film's free surfaces affects flow characteristics, although it did not account for the solutal Marangoni effect. These results highlight the crucial role of film geometry in comprehending flow dynamics, providing important insights for multiple thin liquid film applications.

Free surface deformation can result in complex patterns of concentration, temperature, and flow velocity within a cavity. Thus, controlling this deformation and examining these properties near the bottom surface are critical for the liquid phase in cavity systems [63]. Nonetheless, numerical studies of static surface deformation in cavity systems have not fully

explored the application of horizontal temperature and concentration gradients in both steady and unsteady Marangoni convective flows with deformed free surfaces.

As a result, variations in temperature and concentration along the curved free surface create conflicting thermo-solutal Marangoni forces. This research utilizes 3D numerical simulations to investigate thermal Marangoni convection and coupled thermo-solutal Marangoni convection in a shallow rectangular cavity with a deformed free surface. Additionally, the model is applied to analyze how volume ratios and the Prandtl number affect steady and unsteady Marangoni flows within the liquid phase.

To our understanding, few studies have addressed the alternative impact of thermo-solutal Marangoni convection with a deformed free surface in a floating zone system [49]. The behavior of thermo-solutal Marangoni convection in the cylindrical system of a floating zone differs significantly from that in a rectangular domain. Therefore, to enhance understanding of this phenomenon, this study conducts simulations in a shallow rectangular cavity with a deformed free surface, incorporating the alternative effect of thermo-solutal Marangoni convection.

1.2.4 Effect of free surface deformation on pure thermal Marangoni convection in a liquid bridge

The floating-zone (FZ) method is a crucial crystal growth technique for producing high-quality silicon (Si) and germanium (Ge) alloy crystals. In this system, a molten zone (liquid bridge) is created by heating a short segment of the feed rod with a ring heater. As the heater moves, the feed material at the top melts and joins the liquid bridge, solidifying the seed material at the bottom. The integrity of the melt/seed crystal interface, which remains flat during the solidification process, highlights the crucible-free nature of FZ, significantly contributing to the production of high-quality crystals.

The size of crystals grown by the FZ method is limited due to the adverse effects of gravity, which can cause the liquid bridge to collapse as its diameter increases. However, this limitation can be mitigated under microgravity conditions, allowing for the growth of larger

crystals. The FZ technique ensures reduced contamination, enhanced homogeneity, and increased purity in the grown crystals. A key feature of FZ is forming a liquid bridge without using a container (crucible), thereby eliminating the risk of container-induced contamination and minimizing heterogeneous nucleation.

Marangoni convection is a flow that arises in a liquid bridge along its free surface due to gradients in surface tension. In the FZ method, these surface tension gradients result from temperature and concentration variations along the free surface of the molten zone. Typically, the development of convective bulk flow (strong natural convection) in liquids is driven by buoyancy and plays a significant role in most crystal growth techniques. However, within the context of FZ crystal growth, Marangoni flow is particularly relevant due to a free surface, especially under microgravity conditions.

In the present numerical simulations, a simple "half-zone model" model is considered. This model consists of a pair of coaxial solid cylindrical disks—cold at the top and hot at the bottom—with a liquid bridge (melt) suspended between them. The half zone's side boundary is the liquid bridge's deformed free surface. The half zone model is adopted due to its simplicity and low computational demands, making it an initial approach to overlook phase complexities and focus on bulk (natural) convection.

Considerable insights into the flow transition from steady to oscillatory states in liquid bridges have been experimentally explored by Kang *et al.* [7] under microgravity conditions. These experiments investigated the instability of Marangoni convection and identified three distinct surface configurations based on the volume ratio. Due to the inherent complexities and high costs, conducting such experiments in space is infrequent and challenging. Therefore, numerical investigations serve as a crucial and cost-effective alternative tool.

The geometrical features are crucial for the stability of thermal Marangoni convection [65]. Two main factors influence this stability: the aspect ratio (A_s) and the volume ratio (S), which represents the shape of the free surface [66, 39, 25, 27]. Regarding the stability of convection

in deformable free-surface liquid bridges, Kozhoukharova and Slavchev [67] calculated steady thermal Marangoni convection in FZ with small free surface deformations. Shevtsova *et al*. [68] found that for $Pr = 1$, thermal Marangoni flow occurs near the cold corner of the liquid bridge across a wide range of contact angles.

Due to hydrostatic pressure effects, a deformed free surface in a cylindrical liquid bridge may also occur if the length scale is sufficiently large. Hu *et al*. [69] and Masud *et al*. [70] experimentally suggest that the critical conditions for the onset of oscillatory flows in high Prandtl number liquid bridges highly depend on the volume ratio.

The numerical results of flow bifurcation in thermal Marangoni convection under microgravity and ground conditions for low *Pr* fluids were tested by Shevtsova [71]. Shevtsova and Legros [72] investigated the flow transition of silicone oil ($Pr = 105$) from steady axisymmetric to oscillatory regimes with significant static deformation of the free surface of a liquid bridge. They predicted buoyant thermal Marangoni instabilities with $m = 0$ for relatively low Marangoni numbers under various gravity levels. The critical Reynolds number and *m* of the first bifurcation in the deformed liquid bridge were found to be highly dependent on the volume ratio, as shown by Chen *et al*. [73] and Lappa *et al*. [74]. The studies by Lappa *et al*. [75] and Li *et al*. [76] considered the significant influence of hydrostatic deformation and heating orientation on the threshold for bifurcation in the liquid bridge with $S = 1$.

Nienhüser and Kuhlmann [9] investigated the combined effect of volume ratio and gravity conditions on the linear stability analyses for the first bifurcation.

Prior research has predominantly examined thermal Marangoni convection in liquid bridges with deformed free surfaces. However, solutal Marangoni convection impacts crystal uniformity in these deformed free-surface liquid bridges. The large separation between the liquidus and solidus curves of Si-Ge results in significant Ge segregation in the melt in front of the solidifying interface during SiGe crystal growth. Consequently, the growth rate and

overall melt mixing are important factors influencing solutal Marangoni convection's intensity. There is a critical need to scrutinize the effects of solutal Marangoni convection, which is a prevailing influence in these scenarios. Additionally, previous studies have established that the volume ratio is an exceedingly sensitive parameter governing the bifurcation of thermal Marangoni flow in a liquid bridge.

However, to our knowledge, a comprehensive analysis of thermal and solutal Marangoni convective flows, including examining the effects of volume ratio and the thermal-solutal Marangoni numbers in a liquid bridge, has yet to be conducted.

1.3 Thesis outline

This thesis aims to further understand the effect of Marangoni flow by considering various geometrical conditions in cases of shallow cavity and half-zone models on the flow instabilities and flow pattern transitions. The chapter outlines the present thesis are stated as follows.

In Chapter 2, the employed numerical methods, including governing equations and numerical schemes for calculating the Marangoni convection in a shallow rectangular cavity and half zone, are introduced. In addition, the numerical method and grid independence are validated to confirm the calculation reliability of the present work.

In Chapter 3, a series of numerical simulations are performed to investigate the pure thermal Marangoni convection with different film thicknesses in non-deformed free surface cavities. For the working fluid, Prandtl number value 6.7 is chosen to examine the effect of film thicknesses. In addition, the computed flow characteristics and temperature distribution are analyzed. This work presented herein provides a better understanding of the effect of a film thickness on Marangoni flow for coating and lubrication applications.

In Chapter 4, numerical simulations are carried out to study thermal-solutal Marangoni convection in a shallow rectangular cavity under the effect of deformed free surfaces to shed

further light on improving the uniformity of the thin liquid layer. Also, the alternative contribution of thermal and solutal Marangoni effects on the Schmidt number and Prandtl number fluid induced by temperature and concentration distribution is systematically investigated. Furthermore, the effect of concave, convex and flat free surface configurations on the characteristic of steady and unsteady Marangoni flow is qualitatively studied.

In Chapter 5 investigates the cases of gravity and microgravity conditions of deformed free surfaces in the half zone model. It also determines the critical conditions for three volume ratios under normal gravity conditions. Based on concentration distribution with respect to volume ratio and gravity condition, stability curves of base flow have been developed. The results of the present study would be beneficial for making predictions in industrial processes such as Si-Ge crystal growth of floating zones.

In Chapter 6, the results obtained in this thesis are summarized and concluded, and perspectives for future works are described as an extension of this work.

CHAPTER 2

NUMERICAL METHODS

In many industrial processes, Marangoni convection significantly influences the quality of final products. In this chapter, the author discusses pure thermal Marangoni convection and thermal-solutal Marangoni convection with and without deformed free surfaces in a zero gravity and normal gravity conditions. The governing equations for calculating the Marangoni flow and the relevant assumptions are introduced. All the governing equations associated with the present numerical simulation were solved using the open-source software OpenFOAM.

2.1 Pure thermal Marangoni flow

In most studies, the investigation of Marangoni convection has involved various geometries. For the present study, we have chosen a rectangular model with different thicknesses. This is because the rectangular configuration, unlike the cylindrical case, is more applicable to practical processes such as painting and dying, epitaxial crystal growth, lubrication, and mixing. In our study, we have specifically focused on the thermal Marangoni effect, and to do so, we have deliberately neglected the buoyancy force throughout the system. Additionally, we have adopted a shallow rectangular cavity without deformed free surface to further enhance our understanding of this effect.

The numerical domain configuration is a rectangular cavity filled with silicone oil [98], as shown in Figure 2.1. The top boundary is the flat free surface and adiabatic, while the other are solid cavity walls. The fluid motion in a three-dimensional rectangular cavity with a free surface at the top, as shown in Figure 2.1 (a), is considered in the Cartesian coordinate system. The length, width, and three different thicknesses of the cavities are L, L, and $0.082L$, $0.0615L$, and $0.041L$, respectively. High and low-temperature values, T_h and T_l, are specified at the four side walls, and the constant thermal boundary condition is applied, as shown in Figure

2.1 (b). Due to the imposed temperature difference, the surface tension gradient drives the Marangoni convection along the free surface.

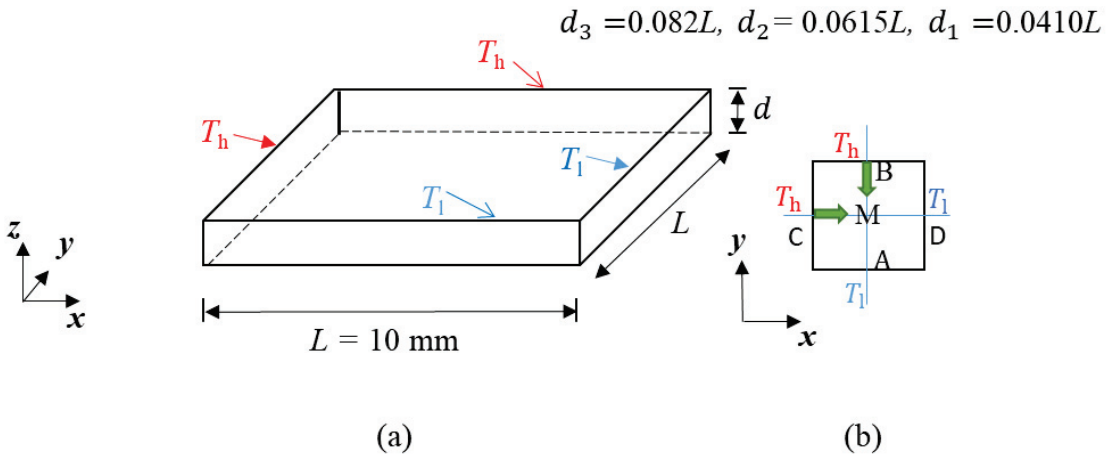

Figure 2.1 (a) Top view of the numerical simulation domain with the prescribed boundary conditions. (b) Near bottom surface boundary conditions (z = 0.0001) and AB, CD lines show at x = 0.5, y = 0.5 and M is a sampling point (0.5, 0.5, 0.0001). The green arrows indicate the direction of thermal Marangoni flows.

In the simulation model, we make the following assumptions:

i. The free surface does not deform under the effect of fluid flow.
ii. The fluid is incompressible, Newtonian, and has constant physical properties except for surface tension.
iii. The no-slip boundary condition on flow velocity is applied along boundaries except for the top free surface, and the thermal Marangoni force is considered along the free surface.

The governing equations of the fluid flow in the cavity are written in dimensionless forms. Being L is the characteristic scale for length, the coordinates (x, y, z) are defined as (x*, y*, z*)/L. In addition, L^2/v and L/v are used as the characteristic time and velocity, respectively;

the dimensionless governing equations are the conservation of mass, momentum, and mass transfer:

$$\boldsymbol{\nabla} \cdot \boldsymbol{V} = 0 \tag{2.1}$$

$$\frac{\partial \boldsymbol{V}}{\partial \tau} + \boldsymbol{V} \cdot \boldsymbol{\nabla} \boldsymbol{V} = -\boldsymbol{\nabla} P + \nabla^2 \boldsymbol{V} \tag{2.2}$$

$$\frac{\partial \Theta}{\partial \tau} + \boldsymbol{V} \cdot \boldsymbol{\nabla} \Theta = \frac{\mathbf{1}}{Pr} \nabla^2 \Theta \tag{2.3}$$

where $\boldsymbol{V} = (V_x, V_y, V_z)$ is the dimensionless velocity vector, the dimensionless temperature is defined as $\Theta = (T\text{-}T_l)\ (T_h\ \text{-}T_l)$, τ and P are respectively the dimensionless time and pressure. $Pr = \nu/\alpha$ is the Prandlt number, where is the ν fluid's kinematic viscosity and α is its thermal diffusivity. In this study, the computations have been performed for the fluid with $Pr = 6.7$, respectively.

The ratio of Marangoni number to Grashof number (Ma_T/Gr_d) was introduced to compare the relative contributions of Marangoni and natural convections. In case of $\frac{Ma_T^{2/3}}{Gr_d^{1/2}} > 1$, the effect of Marangoni convection is dominant compared with that of natural convection [77]. The values of this ratio in thick and thin films are $\frac{Ma_T^{2/3}}{Gr_d^{1/2}} = 16.4$, and $\frac{Ma_T^{2/3}}{Gr_d^{1/2}} = 46.3$, respectively, which indicate that the contribution of buoyancy can be neglected in this study, while that of the Marangoni force is dominant.

The free surface boundary conditions are as follows:

$$V_z = 0 \tag{2.4}$$

$$\frac{\partial V_x}{\partial z} = -Ma_T \left| \frac{\partial \Theta}{\partial x} \right| \tag{2.5}$$

$$\frac{\partial V_y}{\partial z} = -Ma_{\mathrm{T}} \left|\frac{\partial \Theta}{\partial y}\right| \tag{2.6}$$

$$\frac{\partial \Theta}{\partial z} = 0 \tag{2.7}$$

wherein, the thermal Marangoni numbers are defined as:

$$Ma_{\mathrm{T}} = -\frac{\partial \sigma}{\partial T}\frac{(T_{\mathrm{h}} - T_{\mathrm{l}})L}{\mu \nu} \tag{2.8}$$

where μ is the viscosity of the fluid, and $\frac{\partial \sigma}{\partial T} < 0$ is the surface tension coefficients of temperature, respectively.

2.2 Thermo-solutal Marangoni flow

The coupling effect of thermal and solutal Marangoni flows driven by gradients in temperature and concentration plays a critical role in various material processing techniques, including crystal growth, film coating, and microfluidics. This study focuses on the complex interactions of thermal and solutal Marangoni convection in systems with deformed free surfaces under microgravity and gravity conditions, specifically in the cavity and liquid bridge configurations.

2.2.1 Rectangular cavity configuration with deformed free surface

In the numerical simulation model, we consider a cavity filled with a fluid in the absence of gravity effect, as shown Figure 2.2.1. The top boundary is the deformed free surface, which is adiabatic, while the other boundaries are the solid cavity walls.

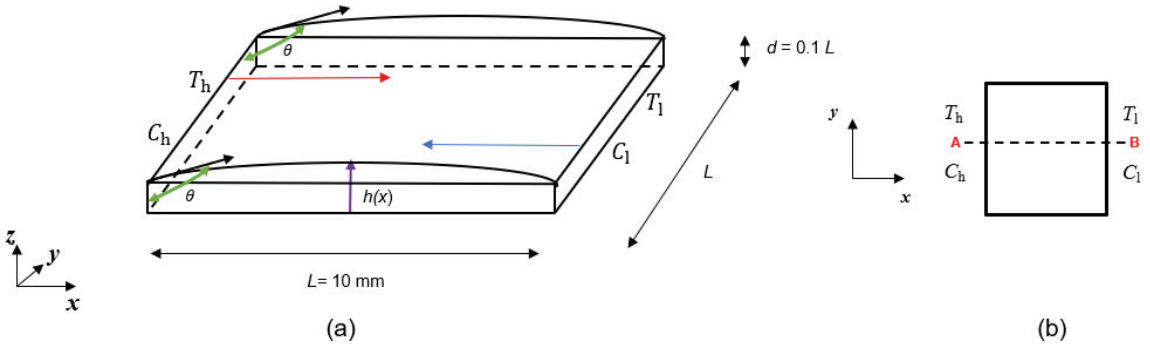

Figure 2.2.1 (a) Top view of the numerical simulation domain with the prescribed boundary conditions. The red and blue arrows indicate the direction of thermal and solutal Marangoni flows. (b) Near bottom surface boundary conditions (z = 0.1 mm) and AB line shows at y = 5 mm.

Concerning the computations, the free surface shape is assumed independent of the fluid flow, temperature and concentration fields. However, it depends on the fluid volume and the hydro-static pressure difference. In this study the maximum Capillary number (Ca) is 2.04 $\times 10^{-4}$. Therefore, we assume the Ca number is low enough to support the assumption that dynamic surface deformation can be neglected [61, 62]. The different free surface shapes represent the corresponding volume ratios. The top boundary is the free surface, and its vertical coordinate is a function of x only ($h(x)$). The assumed hydrostatic shape of the free surface is governed by the Gauss-Laplace equation under no gravity, relating its mean curvature to the pressure jump along the liquid-gas interface:

$$\Delta p = \sigma \left(\frac{1}{R_1} + \frac{1}{R_2} \right) \tag{2.9}$$

where R_1 and R_2 denote the principal radii of curvature at each point of the free surface.

Along the boundary condition that the liquid is attached to the solid boundaries (no-slip), we have,

$$h(0) = d, \quad h(L) = d \tag{2.10}$$

where h is a function of the x direction coordinate and prescribed volume (V) is given by:

$$\int_0^L h(x)\ dx = V = \text{const.} \qquad (2.11)$$

The Cartesian coordinate system is adopted. The cavity's length, width, and depth are L, L, and $0.1L$, respectively. The dimension value of the length of the rectangular cavity is L = 10 mm. Different temperatures and concentrations are specified at the left (T_h, C_h) and right (T_l, C_l) vertical walls, where $T_h > T_l$ and $C_h > C_l$, and zero heat and mass fluxes are imposed on the remaining boundaries, respectively.

Marangoni convection is commonly associated with buoyancy-driven bulk convection, arising from temperature and/or concentration gradients within the liquid volume. Consequently, the convective flow is influenced not only by surface tension gradients but also by the buoyancy. However, the impact of buoyancy diminishes in systems with small dimensions or under microgravity conditions [10]. In thin film configurations characterized by a large surface-to-volume ratio, Marangoni convection along the free surface of the liquid film becomes predominant over natural convection (buoyancy driven). This dominance intensifies as the films decrease in depth.

The ratio of the Marangoni and Grashof numbers in the study is 3.5. This indicates that the contribution of buoyancy can be neglected in this study, while that of the Marangoni force is dominant [77].

For simplification, we assume,

i. The fluid is incompressible and Newtonian.
ii. Physical properties do not change with temperature and concentration except for surface tension.
iii. The no-slip boundary condition is applied except for the top free surface, while the thermal and solutal Marangoni forces are considered on the free surface.

The governing equations of the fluid flow in the cavity are written in dimensional forms.

The dimensional governing equations of the fluid obtained from the overall conservation of mass, the balances of momentum and energy, and the conservation of species mass transfer equations under zero gravity are presented below:

$$\boldsymbol{\nabla} \cdot \boldsymbol{u} = 0 \tag{2.12}$$

$$\frac{\partial \boldsymbol{u}}{\partial t} + (\boldsymbol{u} \cdot \boldsymbol{\nabla})\boldsymbol{u} = -\frac{1}{\rho}\boldsymbol{\nabla} p + \nu \Delta \boldsymbol{u} \tag{2.13}$$

$$\frac{\partial T}{\partial t} + (\boldsymbol{u} \cdot \boldsymbol{\nabla})T = \alpha \Delta T \tag{2.14}$$

$$\frac{\partial C}{\partial t} + (\boldsymbol{u} \cdot \boldsymbol{\nabla})C = D \Delta C \tag{2.15}$$

where $\boldsymbol{u} = (u_x, u_y, u_z)$, represents the fluid flow velocity vector, t is the time, p is the pressure, ΔT and ΔC are the temperature and concentration differences between left and right walls, while ν, α, and D are the kinematic viscosity, thermal diffusivity, and the diffusion coefficient of C in the fluid, respectively.

Free surface boundary conditions are expressed as follows,

$$u_n = 0 \tag{2.16}$$

$$\mu \frac{\partial u_\tau}{\partial n} = -\sigma_T \frac{\partial T}{\partial \tau} - \sigma_C \frac{\partial C}{\partial \tau} \tag{2.17}$$

$$\mu \frac{\partial u_y}{\partial n} = -\sigma_T \frac{\partial T}{\partial y} - \sigma_C \frac{\partial C}{\partial y} \tag{2.18}$$

$$\frac{\partial T}{\partial n} = 0, \quad \frac{\partial C}{\partial n} = 0 \tag{2.19}$$

where the thermal Marangoni number shows 2.8 and solutal Marangoni number is respectively defined as,

$$Ma_{\mathrm{C}} = \frac{\partial \sigma}{\partial C} \frac{(C_{\mathrm{h}} - C_{\mathrm{l}})L}{\mu \nu} \tag{2.20}$$

where $\frac{\partial \sigma}{\partial T} < 0, \frac{\partial \sigma}{\partial C} > 0$ are the surface tension coefficient of temperature and concentration and μ is the viscosity of the fluid. τ and n are the tangential direction coordinate and normal direction of the free surface. The thermal and solutal Marangoni forces are in the opposite directions, as shown by red and blue arrows in Figure 2.2.1. *Sc* (*Sc* = *v*/*D*) is the Schmidt number and *Pr* (*Pr* = *v*/α) is the Prandlt number, and the aspect ratio (A_s = *d*/*L*) of the cavity is 0.1, respectively. The non-dimensional cavity volume ratio is defined as $S = V/V_0$ where $V_0 = L^2 d$.

Here the molten silicon (*Pr* = 0.011) [80, 90] is considered as the low *Pr* number fluid and silicone oil (*Pr* = 6.7) [98] is considered as the high *Pr* number fluid.

2.2.2 Half zone configuration with deformed free surface

The schematic view of the half-zone model configuration (computational domain) is shown in Figure 2.2.2. Temperatures on the upper and lower boundaries are prescribed as a cold boundary on top and a hot boundary at the bottom. The side boundary of the domain is the deformed free surface of the molten zone. All the boundaries of the model domain, including the deformed free surface, are fixed.

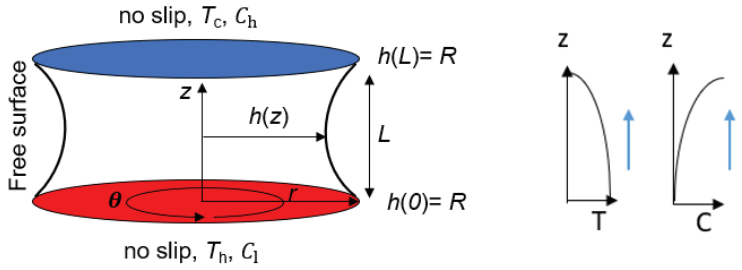

Figure 2.2.2 Description of the half-zone model domain with a deformed free surface. The imposed boundary conditions are also shown in the figure. The blue arrows on the right represent the directions of Marangoni forces driven by temperature and concentration gradients along the free surface.

The cylindrical computational domain dimensions are given in the figure: radius R = 10 mm, half zone height L = 5 mm. The cylindrical coordinate system (with radial (r), azimuthal (θ), and vertical (z) coordinates) is placed at the center of the bottom boundary of the computational domain.

We assume for the simplification,

i. Mixture of silicon and germanium and is assumed to be a Newtonian and incompressible fluid in the model.
ii. The physical properties of the mixture remain unchanged with concentration and temperature but change with surface tension. Boussinesq approximation is adopted for buoyancy in the melt.
iii. The free surface is assumed to be adiabatic. Concerning the computations, the free surface shape is independent of the fluid flow, temperature, and concentration fields but depends on the volume of the liquid, the hydrostatic pressure difference, and gravity.

The maximum Capillary number (Ca) in this study is 7.5×10^{-5}. Therefore, we assume the Ca number is low enough to support the assumption that dynamic surface deformation can be neglected [61, 62].

The free surface is an axisymmetric boundary with three shapes representing a corresponding volume ratio. Assuming the interface is fixed and axisymmetric concerning the z-axis in the half-zone domain, the radial coordinate is a function of z only (i.e., $r = h(z)$). The shape of the free surface is governed by the Gauss-Laplace equation, which relates its mean curvature to the pressure jump across the liquid-gas interface.:

$$\Delta p + \rho g z = \sigma \left(\frac{1}{R_1} + \frac{1}{R_2} \right) \tag{2.21}$$

where R_1 and R_2 denote the principal radii of curvature at each point of the free surface. Along the boundary condition that the liquid is attached to the solid boundaries (no-slip), we have,

$$h(0) = R, \quad h(L) = R \tag{2.22}$$

where h is a function of the vertical coordinate z.

Regarding governing equations for the growth melt include overall mass conservation, energy balance, and species mass transfer conservation shown in previous section (2.2.1). Applied the Boussinesq approximation in the momentum balance is presented as follows:

$$\frac{\partial \boldsymbol{u}}{\partial t} + (\boldsymbol{u} \cdot \boldsymbol{\nabla})\boldsymbol{u} = -\frac{1}{\rho}\boldsymbol{\nabla} p + \nu \boldsymbol{\nabla^2 u} + g\left(\beta_{\mathrm{T}}(T - T_{\mathrm{c}}) - \beta_{\mathrm{C}}(C - C_{\mathrm{l}})\right) e_z \tag{2.23}$$

where, $\boldsymbol{u} = (u_r, u_\theta, u_z)$ represents melt flow velocity, and C and C_{l} are the molar fraction and minimum molar fraction of silicon in the SiGe melt. g is the gravitational acceleration, $\boldsymbol{e}_{\mathrm{z}}$ is unit vector in a vertical direction, β_{T} and β_{C} are the thermal and solutal expansion coefficients, respectively.

On the top and bottom boundaries of the domain, we assume the no-slip condition on flow velocity ($u = 0$). The Marangoni convection condition is used along the free surface ($r = h(z)$). A higher temperature (T_h) value is imposed on the bottom plane, and a lower temperature (T_c) value is set on the top plane. The condition of pure silicon concentration ($C_h = 1$) is imposed on the top boundary ($z = 5$ mm) while the pure germanium concentration ($C_l = 0$) condition is prescribed on the bottom boundary ($z = 0$ mm). The surface tension is taken as the function of concentration and temperature only. The boundary conditions along the free surface ($r = h(z)$) are given as follows:

$$u_r = 0 \tag{2.24}$$

$$\mu\left[r\frac{\partial}{\partial n}\left(\frac{u_\theta}{r}\right)\right] = -\frac{1}{r}\left(\frac{\partial\sigma}{\partial T}\frac{\partial T}{\partial\theta} + \frac{\partial\sigma}{\partial C}\frac{\partial C}{\partial\theta}\right) \tag{2.25}$$

$$\mu\frac{\partial u_n}{\partial n} = -\left(\frac{\partial\sigma}{\partial T}\frac{\partial T}{\partial\tau} + \frac{\partial\sigma}{\partial C}\frac{\partial C}{\partial\tau}\right) \tag{2.26}$$

$$\frac{\partial T}{\partial n} = 0, \quad \frac{\partial C}{\partial n} = 0 \tag{2.27}$$

where the thermal and solutal Marangoni numbers defined in previous section (2.2.1) and the thermal and solutal Rayleigh numbers are respectively defined as,

$$Ra_T = \frac{g\beta_T L^3 \Delta T}{\nu\alpha} \tag{2.28}$$

$$Ra_C = \frac{g\beta_C L^3 \Delta C}{\nu\alpha} \tag{2.29}$$

The thermal and solutal Marangoni forces are in the same direction, as shown by blue arrows in Figure 2.2.2. In the present study $Sc = 14$ and $Pr = 6.37 \times 10^{-3}$, respectively, and the aspect ratio ($A_s = L/R$) of the liquid bridge is 0.5. The physical parameters used in the simulation are

taken from [78, 79]. The nondimensional liquid bridge volume ratio is defined as $S = V/V_0$ where $V_0 = \pi R^2 L$.

2.3 Numerical method and validation

The governing equations are discretized using the Finite Volume Method (FVM) and solved with the PISO algorithm in the OpenFOAM software. FVM, a technique for representing and evaluating partial differential equations as algebraic equations, is known for its precision. It calculates values at discrete points on a meshed geometry, with each node in the mesh surrounded by a small finite volume. In FVM, volume integrals containing a divergence term in a partial differential equation are converted to surface integrals using the divergence theorem. These terms are then evaluated as fluxes at the surfaces of each finite volume. The method's inherent conservation property, where the flux entering one volume equals the flux leaving the adjacent volume, further enhances its reliability.

The PISO algorithm (Pressure Implicit with Splitting of Operator) operates without iterations, using large time steps and requiring less computational effort. It extends the SIMPLE algorithm used in computational fluid dynamics (CFD) to solve the Navier-Stokes equations. Originally developed for non-iterative computation of unsteady compressible flow, PISO has been successfully adapted for steady-state problems. It involves one predictor step and two corrector steps, designed to ensure mass conservation through predictor-corrector steps.

The computation is carried out using the open-source software OpenFOAM. The governing equations adopt the Euler, QUICK, and Gauss linear schemes for terms involving time derivative, divergence, and Laplacian.

To ensure the hydrostatic deformation of the free surface was correctly calculated, we also compared the results with those of Lappa [80] as a benchmark work, as shown in Figure 2.3.

The details of the validation of the solver using OpenFOAM can be found in the previous researchers [89, 93].

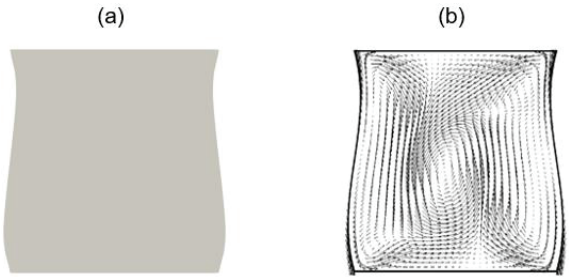

Figure 2.3 Validation for free surface deformation for $S = 1$ with $A_s = 1$ under normal gravity at the vertical r-z plane (a) using present the surface curvature code, (b) result of Lappa [80].

2.4 Grid independence and validation

The uniform grids near all the boundaries resolve the thin boundary layers. Meanwhile, simulation results with different grids are compared to verify the grid dependency in the case of pure thermal Marangoni convection without deformed free surface. Table 2.4.1 shows the dimension velocities on the free surface sampling points P (x, y, z) = (0.5, 0.5, 0.082), Q (x, y, z) = (0.5, 0.5, 0.0625), R (x, y, z) = (0.5, 0.5, 0.041) and the near bottom surface sampling point M (x, y, z) = (0.5, 0.5, 0.0001) at different thickness values. The maximum deviations of velocities are less than 2% between two fine grids, so the grids of 140×140×30, 140×140×25, 140×140×20 are chosen for the high-accuracy simulation in the cases of difference thicknesses (d_3 = 0.082, d_2 = 0.0625, and d_1 = 0.041) for Pr = 6.7, respectively.

Table 2.4.1 Comparison of velocity magnitude at P, Q, R with M points in the cases of thicker film (d_3), middle range of film thickness (d_2), and thinner film (d_1) at pure thermal Marangoni convection without deformed free surface. $N_x \times N_y \times N_z$ are the numbers of grids in x, y, and z directions.

Film thickness (d_3) = 0.082 for $Ma_{\mathrm{T}} = 2 \times 10^3$

Mesh ($N_x \times N_y \times N_z$)	**Velocity (m/s) at P point**	**Velocity (m/s) at M point**
120 ×120× 30	-0.001647	0.00005768
140 ×140× 30	**-0.001643**	**0.00005324**
160 ×160× 30	-0.001640	0.00005310

Film thickness (d_2) = 0.0625 for $Ma_{\mathrm{T}} = 2 \times 10^3$

Mesh ($N_x \times N_y \times N_z$)	**Velocity(m/s) at Q point**	**Velocity(m/s) at M point**
120 ×120× 25	-0.001544	0.00006614
140 ×140× 25	-0.001542	0.00006607
160 ×160× 25	-0.001540	0.00006602

Film thickness (d_1) = 0.0410 for $Ma_{\mathrm{T}} = 2 \times 10^3$

Mesh ($N_x \times N_y \times N_z$)	**Velocity (m/s) at R point**	**Velocity (m/s) at M point**
100 ×100× 20	0.001000810	0.00005497
120 ×120× 30	0.001000150	0.00005493
140 ×140× 20	0.000999739	0.00005490
160 ×160× 20	0.000999465	0.00005490

In the case of deformed shallow cavity case, Figure 2.4.1 shows a sample computational grid. A finite volume method with uniform grids was applied to discretize the governing equation and boundary conditions. Meanwhile, simulation results with four different grids are

compared to verify the grid dependency in the case of convex free surface (volume ratio (S) = 1.2) with thermal Marangoni convection and thermo-solutal Marangoni convection. Table 2.4.2 shows the convex free surface's sampling point and maximum velocity at different Schmidt and Prandtl number values. The maximum deviation of the velocities less than 4% between two fine grids. Therefore, grids of 80×80×40 and 120×120×40, 120×120×40 and 140×140×40 are chosen for the high-accuracy simulation in the cases of Pr = 0.011, 6.7 and Sc = 4.85, Pr = 0.011, and Sc = 4.85, Pr = 6.7, respectively.

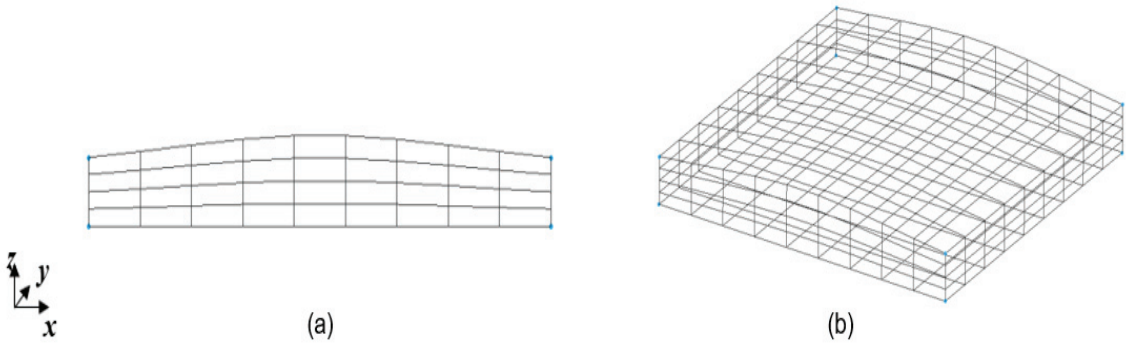

Figure 2.4.1 The computational mesh used in the simulations: (a) the grid at the x-z plane; (b) the 3D grid configuration.

Table 2.4.2 Comparison of sample velocity and maximum velocity in four different cases for thermal Marangoni convection and thermo-solutal Marangoni convection with deformed free surface (S = 1.2). $N_x \times N_y \times N_z$ are the numbers of grids in x, y, and z directions.

$Pr = 0.011$, $S = 1.2$ for $Ma_{\mathrm{T}} = 5 \times 10^4$

Mesh ($N_x \times N_y \times N_z$)	***x*- velocity (m/s) (0.5 *L*, 0.5 *L*, 0.1 *L*)**	**Maximum velocity (m/s)**
Mesh 1. 80 × 80 × 30	0.0022987	0.0336079
Mesh 2. 80 × 80× 35	0.0028452	0.0339838
Mesh 3. 80 × 80 × 40	**0.0033003**	**0.0342388**
Mesh 4. 80 × 80 × 45	0.0036119	0.0344335

$Pr = 6.7$, $S = 1.2$ for $Ma_{\mathrm{T}} = 5 \times 10^3$

Mesh ($N_x \times N_y \times N_z$)	***x*- velocity (m/s) (0.5 *L* , 0.5 *L*, 0.13 *L*)**	**Maximum velocity (m/s)**
Mesh 1. 120 × 120 × 30	0.00398613	0.015896
Mesh 2. 120 × 120 × 35	0.00402663	0.016885
Mesh 3. 120 × 120 × 40	**0.00405717**	**0.0176872**
Mesh 4. 120 × 120 × 45	0.00408041	0.0183532

Sc = 4.85, *Pr* = 0.011, *S* = 1.2 for $Ma_{\mathrm{C}} = 1 \times 10^4$, $Ma_{\mathrm{T}} = 5 \times 10^3$

Mesh ($N_x \times N_y \times N_z$)	***x*- velocity (m/s) (0.5 *L*, 0.5 *L*, 0.13 *L*)**	**Maximum velocity (m/s)**
Mesh 1. 120 × 120 × 30	0.00123534	0.00071
Mesh 2. 120 × 120 × 35	0.00124776	0.00076
Mesh 3. 120 × 120 × 40	**0.00125746**	**0.00080**
Mesh 4. 120 × 120 × 45	0.00126441	0.00083

Sc = 4.85, *Pr* = 6.7, *S* = 1.2 for $Ma_{\mathrm{C}} = 3 \times 10^3$, $Ma_{\mathrm{T}} = 2 \times 10^3$

Mesh ($N_x \times N_y \times N_z$)	***x*- velocity (m/s) (0.5 *L*, 0.5 *L*, 0.13 *L*)**	**Maximum velocity (m/s)**
Mesh 1. 140 × 140 × 30	0.0012883	0.00251
Mesh 2. 140 × 140 × 35	0.0013013	0.00269
Mesh 3. 140 × 140 × 40	**0.00130946**	**0.00284**
Mesh 4. 140 × 140 × 45	0.00131757	0.00295

In the case of half zone model with deformed free surface, Figure 2.4.2 shows a sample computational grid. Meanwhile, simulation results with four different grids are compared to verify the grid dependency in the case of convex free surface (volume ratio (*S*) = 1.1) with thermo-solutal Marangoni convection. Table 2.4.3 shows the convex free surface's maximum vertical velocity at *Sc* = 14 and *Pr* = 6.37× 10^{-3} value. The maximum deviation of the

velocities less than 5% between two fine grids. Therefore, grids of 45×180×60 is chosen for the high-accuracy simulation in the case, respectively.

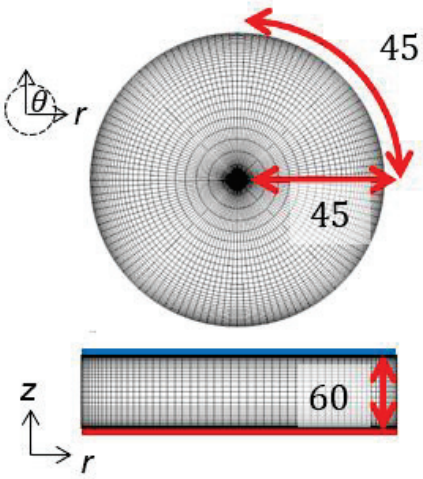

Figure 2.4.2 Computational mesh is used in the simulations. The mesh numbers in the r, θ, z directions are 45, 180, and 60, respectively. The total mesh number is 486000.

Table 2.4.3 Comparison of maximum vertical velocity in four different cases thermo-solutal Marangoni convection with deformed free surface (S = 1.1). $N_r \times N_\theta \times N_z$ are the numbers of grids in r, θ, and z directions.

Sc = 14, Pr = 6.7× 10^{-3}, S = 1.1 for Ma_C = 1072, Ma_T = 1750, Ra_T= 239

Mesh ($N_r \times N_\theta \times N_z$)	**Maximum vertical velocity (m/s)**
1. 35 × 35 × 40	3.36× 10^{-3}
2. 40 × 40× 50	3.49× 10^{-3}
3. 45 × 45 × 60	3.61× 10^{-3}
4. 55 × 55 × 70	3.78× 10^{-3}

CHAPTER 3

STUDY OF THE EFFECT OF LIQUID DEPTH ON THE STABILITY OF THERMAL MARANGONI CONVECTION IN A SHALLOW CAVITY

In the fast-drying process, reaction-hardening of thin films is achieved through heat treatment. The sharp decrease in solvent concentration near the layer surface induces a significant temperature gradient. This study presents a series of three-dimensional numerical simulations of thermal Marangoni convection instabilities in a non-deformed free surface shallow cavity filled with silicone oil subjected to perpendicular temperature gradients. The effects of film thickness on the occurrence of instabilities, mixing efficiency in the film, and lubrication performance are discussed. Additionally, the evaluation of computed flow patterns for different film thicknesses is presented.

3.1 Basic flow pattern

At relatively small thermal Marangoni numbers, the flow in the cavity is steady. This steady flow regime is referred to as "basic flow". Figure 3.1 shows computed streamlines (left) and isothermal lines (right) of a typical basic flow for the film thicknesses of 0.041 (Figure 3.1 (a) and (b)) and thickness 0.082 (Figure 3.1 (c) and (D)). Due to the small temperature gradient, the basic flow appears as a single roll in the C-D plane of the cavity, as shown in Figure 2.1 at different thickness values. The surface flow is from the high-temperature region to the low-temperature region. The return flow develops near the bottom. Therefore, the maximum fluid flow velocity decreases from the top free surface to the bottom surface. When considering the same thermal Marangoni number for both thinner and thicker films, the maximum fluid flow velocity is nearly the same on the top free surface in both cases. However, the maximum velocity is greater for a thinner film near the bottom surface than that for a thicker film. The results indicate that the velocity near the bottom surface has an important role in flow stabilization.

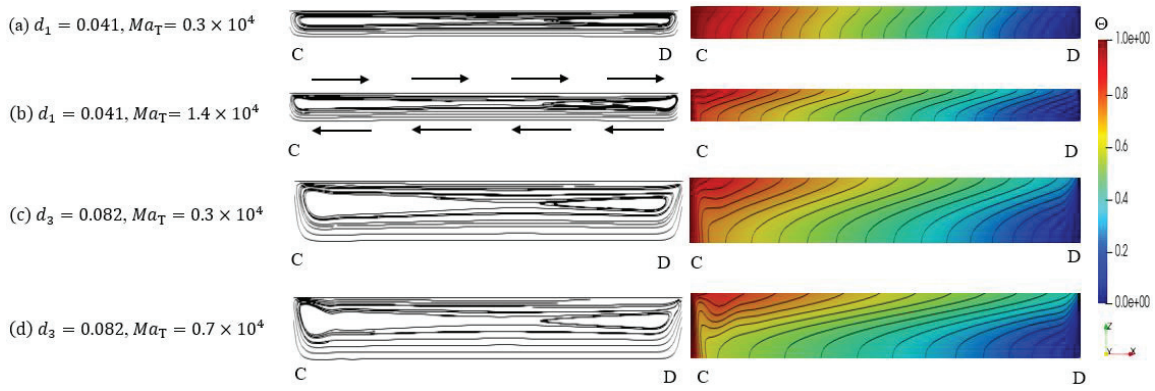

Figure 3.1 Streamlines (left) and isothermal lines (right) of the basic flow in the C-D plane at z = 0.0001 corresponding to the thickness and thermal Marangoni numbers.

When the thermal Marangoni number is relatively small, the temperature boundary layer appears near the side walls of a thicker film, as shown in Figure 3.1 (c) and (d). Figure 3.2 shows the computed temperature distribution across the free surface near the bottom at different thermal Marangoni numbers and film thicknesses. Large temperature gradient drops can be observed in the temperature boundary layers near the sidewalls with high temperature so that the effective temperature gradient in the middle part of the bottom surface is smaller than that near the sidewalls. Furthermore, it was found that the temperature gradient drop increases with the film thickness. The temperature boundary layer thickness decreases with the thermal Marangoni number, as indicated in Figure 3.2.

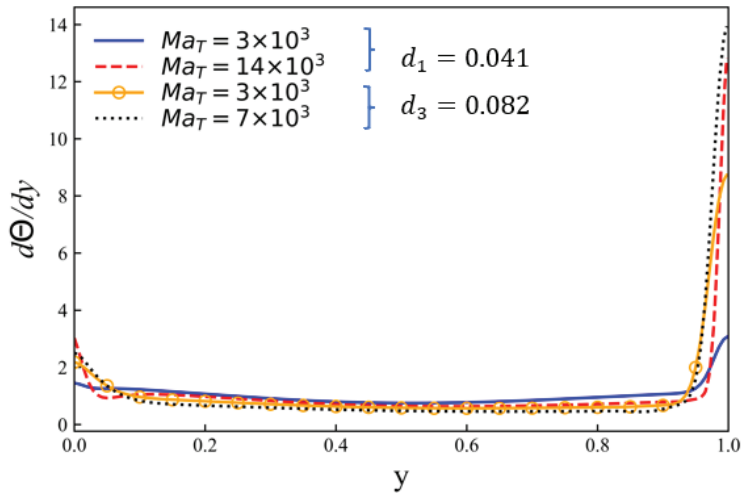

Figure 3.2 Temperature gradient distribution along the A-B plane shown in Figure 2.1 (b) at z = 0.0001.

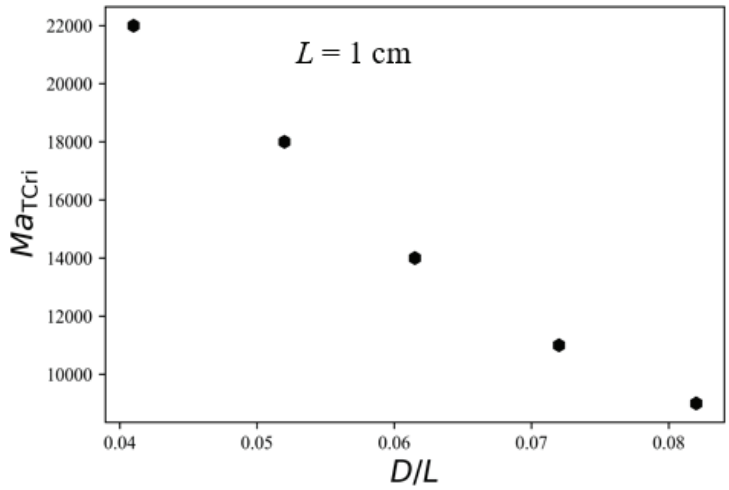

Figure 3.3 Stability curve between non- dimensional thicknesses and thermal Marangoni numbers.

3.2 Critical thermal Marangoni number

When the thermal Marangoni number exceeds a specific critical value, referred to as the "critical" thermal Marangoni number ($Ma_{\mathrm{T,Cri}}$), the basic flow becomes unsteady and bifurcates into three-dimensional oscillatory flows. The $Ma_{\mathrm{T,Cri}}$ was obtained as 2.2×10^4, 1.4×10^4 and 0.9×10^4 for three different cavity heights: 0.041, 0.0615, and 0.082, respectively, using the dynamic mode decomposition method (DMD) [39]. According to Figure 3.3, the critical thermal Marangoni number is relatively small for thicker films than that for thinner films. Thus, the flow easily losses its stability when the height of the rectangular cavity increases. The steady flow regime becomes stable for a wide range of thermal Marangoni numbers for small film thickness. In a thinner liquid layer, the basic flow appears in an extensive range of temperature differences. Additionally, this laminar flow enhances flow uniformity in the entire liquid film; thus, such a uniform flow distribution provides better surface uniformity. Therefore, the present results indicate that a thinner film layer is useful for achieving smooth surfaces in the extensive range of temperature differences. These results imply that thinner liquid layers are suitable for high-quality polishing applications. A similar flow behavior is observed in the experimental work of paint color of Curak *et.al* [81] for thicker films, where various Marangoni cells were observed with fluid motion. As a result, color changes occurred. Furthermore, they did not observe oscillatory flow patterns in the case of thinner films, and no color change occurred due to uniform fluid motion.

3.3 Three-dimensional oscillatory flow

When the thermal Marangoni number is above the critical value, the steady flow in the cavity destabilizes and bifurcates to a three-dimensional oscillation flow. Figure 3.4 shows periodic oscillation patterns of flow velocity magnitude and temperature with time at the monitoring point (M) (x, y, z) = (0.5, 0.5, 0.0001) when $Ma_{\mathrm{T}} = 2.4\times10^4$ in the thinner film (0.041). The oscillation flow pattern depends on the dynamic equilibrium between the thermal Marangoni flow and its inertial effect. Because of the existence of flow inertia, there is a fixed phase lag between temperature and flow velocity oscillations, as shown in Figure 3.4. Therefore, the coupling effect leads to the development of instabilities in the form of

HTW near the bottom surface. Furthermore, the oscillatory phase difference between temperature and velocity is similar to the phase difference between concentration and velocity values of the hydrosolutal waves (HSW) in the case of solutal Marangoni flow. According to the simulation results of (M. K. Smith and S. H. Davis [13]; Li *et.al* [82]), and Shi and Imashi *et.al* [83] on the HTW, it is suggested that the mechanism responsible for the instability of the HTW at high Prandtl number values is similar to that of the instability of HSW observed at high Schmidt numbers [84, 85].

For the case of a thicker film (0.082), three different oscillatory flow patterns were observed at different thermal Marangoni numbers (Ma_{T} = 1.2×10^4, 1.5×10^4, and 2.4×10^4), as shown in Figure 3.5. At a small thermal Marangoni number (Ma_{T} = 1.2×10^4), the amplitude of the temperature oscillation is constant, and two significant harmonics appear with a fundamental frequency of F = 55, as shown in Figure 3.5 (a). When the thermal Marangoni number is sufficiently large (Ma_T = 1.5×10^4), the temperature oscillation shows complex frequency spectra as shown in Figure (b). At a higher thermal Marangoni number, Ma_{T} = 2.4×10^4, a dominant frequency cannot be detected in the temperature oscillation spectrum, as shown in Figure 3.5 (c), and the Marangoni flow becomes completely chaotic.

Flow oscillation with high frequency enhances mixing efficiency, and chaotic advection increases the spread performance. The chaotic flow possesses the maximum fluid velocity with streamwise vorticity motion in the fluid layer, and this turbulent motion produces spontaneous lateral spreading at the free surface. Furthermore, the source of streamwise vorticity is driven in the entire bulk fluid and strengthens the spreading performance without an external force. Mixing and spreading properties are vital for lubrication applications. For thicker films, chaotic flow patterns appear at Ma_{T} = 2.4×10^4 while the thinner film shows a laminar flow behavior. Thus, the results of oscillation flows suggest that the thicker films are more appropriate for lubrication and mixing applications. The experimental results of Hu *et.al* [86] show that the frequency-dependent mixing efficiency reached the maximum in the presence of sufficiently strong Marangoni convection with chaotic motion at a higher frequency.

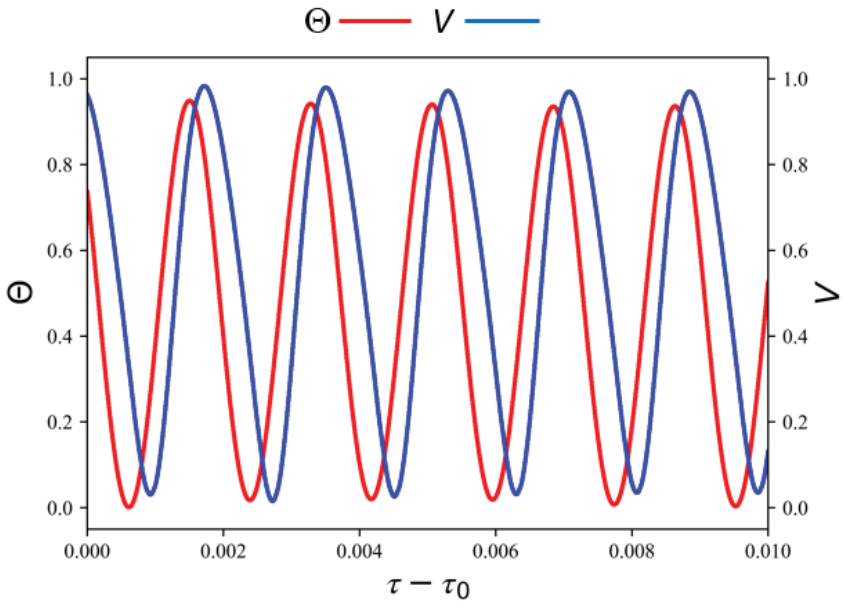

Figure 3.4 Periodic oscillation of velocity V and temperature with time at the monitoring point M, ((x, y, z) = (0.5,0.5,0.0001)) when $Ma_T = 2.4\times10^4$.

To extract the three-dimensional disturbances, a fluctuation measure is introduced as follows:

$$\delta W(x,y,z,\tau) = W(x,y,z,\tau) - \frac{1}{\tau}\int_{\tau_0}^{\tau_0+\tau_P} W(x,y,z,\tau)d\tau \qquad (3.1)$$

where, W represents temperature or velocity.

Figure 3.6 presents the computed streamlines (left), snapshots of the computed surface temperature at z = 0.0001 (middle), and snapshots of the velocity fluctuations at z = 0.0001 (right). In the case of a thickness of 0.041 and in the range of $2.2\times10^4 < Ma_T < 3.1\times10^4$, an oscillation flow pattern is observed, as seen in Figure 3.6 (a) and (b). For small thermal Marangoni numbers, HTW propagates toward the lower right wall and its direction changes toward the upper left wall as the thermal Marangoni number increases, as described by white arrows in Figure 3.6 (a) and (b). In the case of HTW, the spatial phase change between the

surface temperature oscillation and the velocity oscillation is maintained by the coupling between the thermal Marangoni effect and kinetic energy of the return flow, letting the waves travel in the transverse direction. Under the high thermal Marangoni condition, this close coupling between the thermal Marangoni effect and kinetic energy to form the HTW seems like a different way of relaxation, i.e., alternative change in the flow direction of the HTW. The mechanism of instability in the flow pattern is shown on the left side of the streamlines in Figure 3.6 (a) and (b) and the corresponding *x*-component velocity on the right side of Figure 3.6 (a) and (b). Chaotic flow patterns were not overserved at the small thickness values and considered range of thermal Marangoni numbers.

For larger film thickness (0.082) in the range of thermal Marangoni numbers $1\times10^4 < Ma_T < 1.7\times10^4$, the flow exhibits a three-dimensional wave-type oscillation, as shown in Figure 3.6 (c). As shown in Figure 3.6 (c), the flow cell and temperature fluctuation with the periodic oscillation move in the same direction of the temperature gradient. The fundamental frequency ($F = 55$) and the harmonic frequencies ($2F \approx 120$, $3F \approx 180$) shown in Figure 3.5 (a) represent this oscillation. As the Marangoni number increases, the periodic oscillation of flow cell changes to chaotic behavior. Moreover, heat spots appear near the bottom, and they move randomly, as shown in Figure 3.6 (d). This chaotic behaviour is responsible for the random peaks shown in Figure 3.5 (c). The more complex flow structure shown in Figure 3.6 (d) induces velocity fluctuations unevenly in the entire liquid film, which is beneficial in enhancing the mixing and lubricating performances.

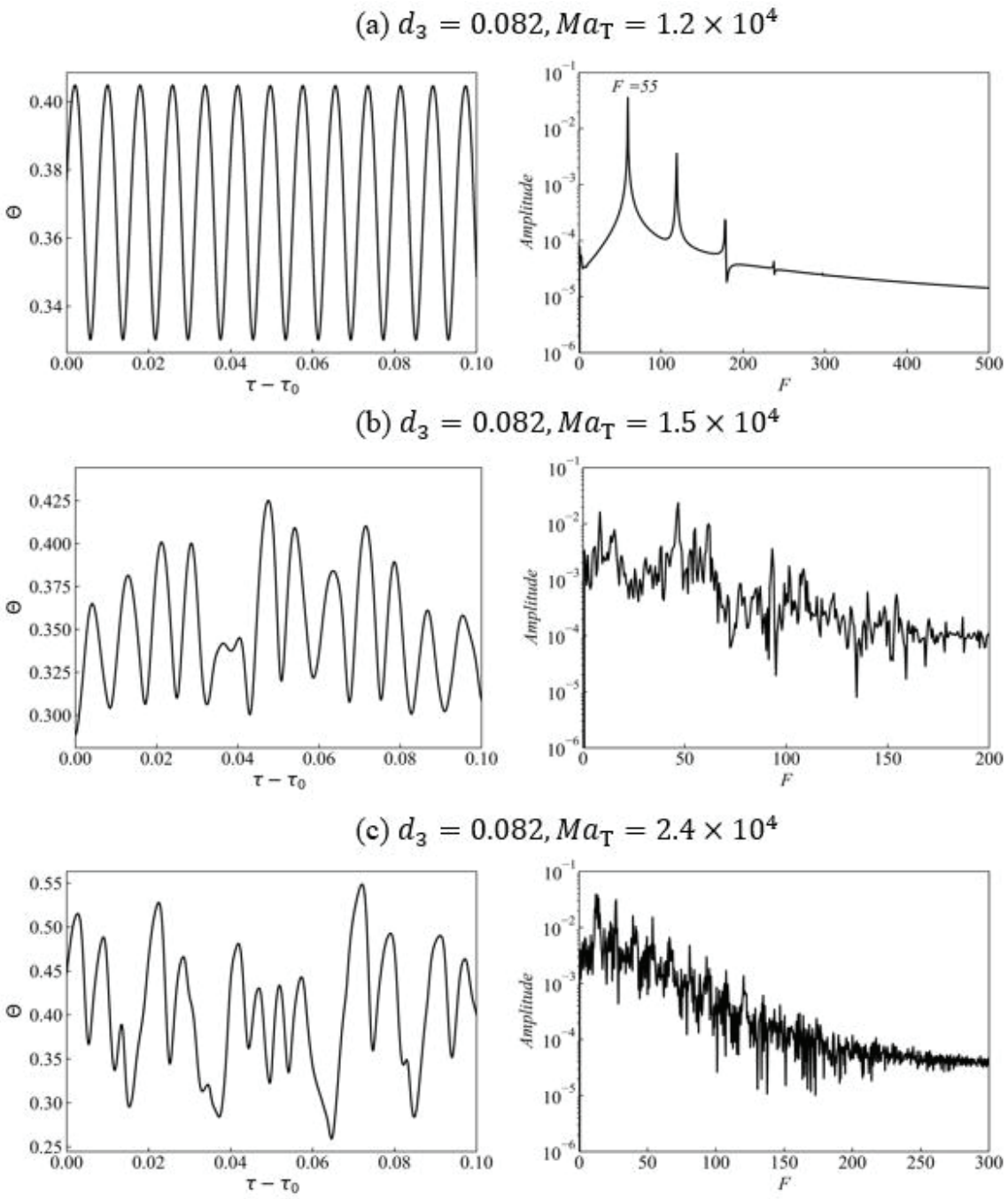

Figure 3.5 Variation in temperature at the sampling point M, ((*x*, *y*, *z*) = (0.5,0.5,0.0001)) with time and frequency spectra.

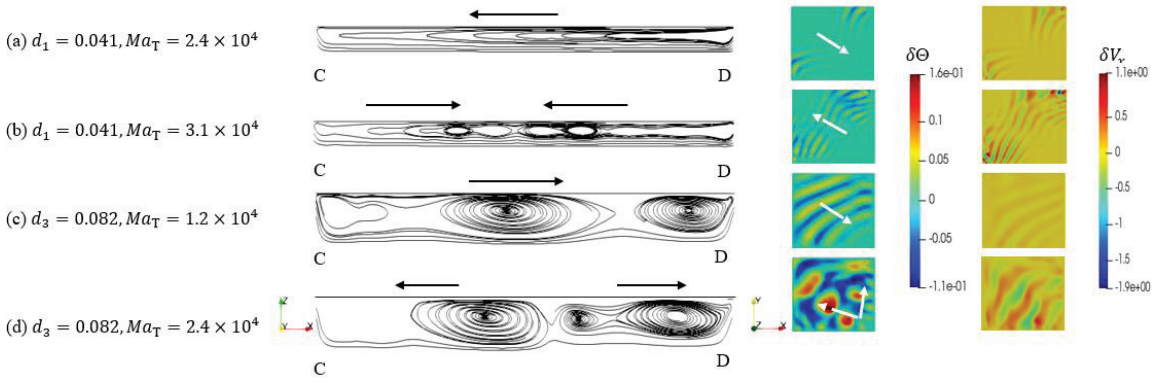

Figure 3.6 Streamlines in the C-D plain (left), snapshots of the temperature fluctuation on the *x*-*y* plain (middle), and *x*-direction velocity fluctuation on the *x*-*y* plain (right) at $z = 0.0001$.

CHAPTER 4

STUDY OF THE EFFECT OF DEFORMED FREE SURFACE ON THE THERMO-SOLUTAL MARANGONI CONVECTION IN A SHALLOW CAVITY

Free surface deformation can lead to various issues, including complex concentration, temperature, and flow distribution. Managing this surface deformation is crucial for optimizing the quality and performance of the thin liquid films grown on substrates. Consequently, temperature and concentration variations exist along the curved free surface, leading to opposing thermo-solutal Marangoni forces in microgravity. This study employs 3D numerical simulations to explore thermal Marangoni convection and the alternative effect of thermo-solutal Marangoni convection within a rectangular cavity featuring a deformed free surface in microgravity conditions. We further utilize the model to examine the impact of volume ratio and Prandtl numbers on steady and unsteady Marangoni flows in the shallow rectangular cavity system.

4.1 Effect of volume ratio under thermal Marangoni convection for low *Pr* number fluids

Considering the relatively small thermal Marangoni numbers (Ma_{T}) the flow within the cavity exhibits steadiness, referred to as the "basic flow" regime. Figure 4.1 shows computed isotherm lines of the basic flow near the bottom surface (z = 0.1 mm) at Ma_{T} = 5×10^3 exhibit parallelism between the sidewalls for all three volume ratios since the heat transfer occurs by diffusion in a low Prandtl number fluid (Pr = 0.011).

As shown in Figure 4.1 (a-c), the uniform distance between isotherms lines is almost maintained in all three cases. Figure 4.1 (d) shows the temperature distribution when a temperature difference of ΔT = 0.5 K is applied between sidewalls. The temperature decrease follows a linear trend at S = 1. In contrast, in the cases of S = 0.8 and S = 1.2, temperature

slightly bends towards the opposite side; this bending angle of the temperature drop gives rise to a non-uniform temperature distribution. However, the effect of the volume ratio on temperature distribution is small due to the low *Pr* number. Figure 4.2 shows the effect of volume ratio on the *x*-direction flow velocity near the bottom surface ($z = 0.1$ mm). As shown in Figure 4.2 (d), the effect of volume ratio on the flow velocity is significant near the cold wall. Figure 4.3 shows the effect of volume ratio on streamlines. When the cavity is shallow, the width of streamlines becomes narrower, and the flow velocity becomes faster in the middle part of the liquid. Due to the satisfaction of momentum balance, the flow near the cold wall becomes slower as seen in Figure 4.2 (d).

When the thermal Marangoni number exceeds the critical value $Ma_{\mathrm{T,Cri}}$, the steady thermal Marangoni flow transits into an unsteady flow regime. Under unsteady conditions ($Ma_{\mathrm{T}} = 1.5\times10^5$), the volume ratio affects the temperature field, and the isotherm lines near the bottom surface deform for all volume ratios as shown in Figure 4.4 (a-c). The isotherms lines' deformation increases in the cases of $S = 0.8$, $S = 1$, and then $S = 1.2$, respectively. As shown in Figure 4.4 (d), it is noticed that a linear temperature decrease is observed for the case of $S = 1$ and bending towards the opposite side in the cases of $S = 0.8$ and $S = 1.2$. This variation in temperature distribution is due to the effect of free surface shape. When comparing Figure 4.1 and Figure 4.4, a more uniform temperature distribution is seen in the steady Marangoni condition than in the unsteady Marangoni condition. Figure 4.5 shows the effect of volume ratio on the flow field in unsteady conditions. As shown in Figure 4.5 (d), sharp velocity peaks appear near the cold wall, and the peak becomes higher (as shown in Figure 4.5 (d)), and the higher flow velocity regime becomes wider (Figure 4.5 (a-c)) as *S* increases. These peaks are due to vortices near the cold wall shown in Figure 4.6 (a-c). These vortices are almost stationary but changing in size. Therefore, it is evident that the *x*-direction flow velocity becomes unsteady, and the value of velocity fluctuation insufficiently to vortices movement for all volume ratio, as shown in Figure 4.6 (d-f).

This section concludes that the volume ratio plays a significant role in determining the flow strength and promotes steeper temperature gradients in unsteady Marangoni conditions. The

following section discusses the effect of volume ratio on thermo-solutal Marangoni convection.

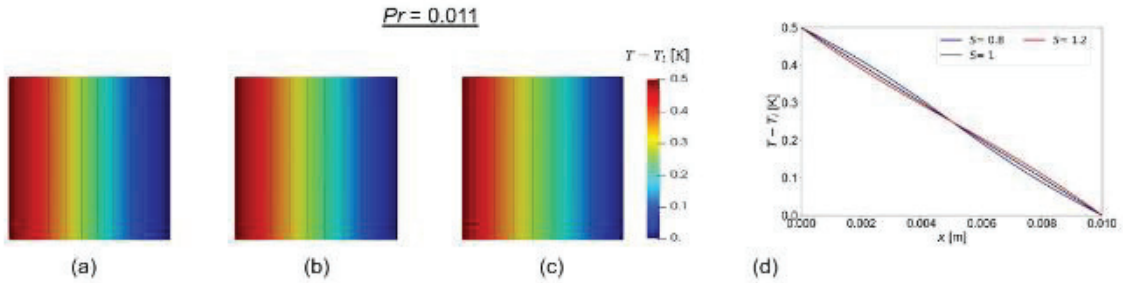

Figure 4.1 The isotherms lines for (a) S = 0.8 (b) S = 1 (c) S = 1.2 and (d) temperature distribution along the AB line for all volume ratios at the x-y plane near the bottom surface (z = 0.1 mm) at (Ma_{T} = 5 × 10^3).

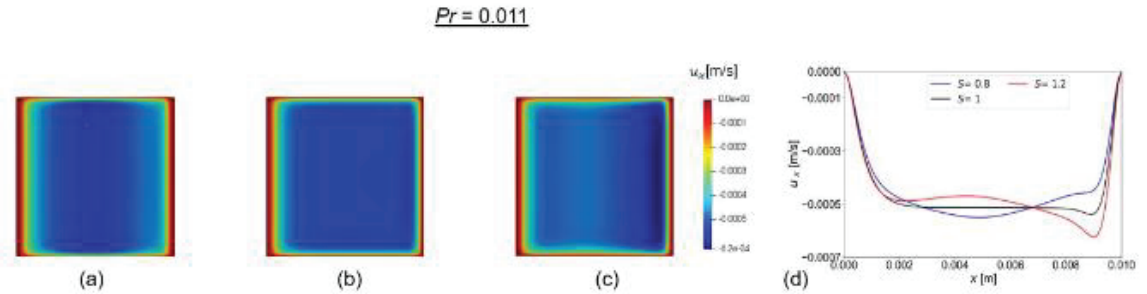

Figure 4.2 The x-direction flow velocity for (a) S = 0.8 (b) S = 1 (c) S = 1.2 and (d) the x-direction velocity distribution along the AB line for all volume ratios at the x-y plane near the bottom surface (z = 0.1 mm) at (Ma_{T} = 5 × 10^3).

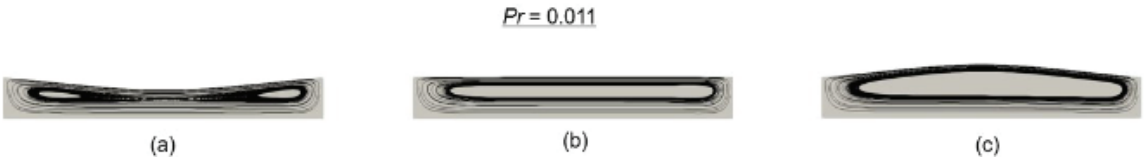

Figure 4.3 The streamlines for (a) S = 0.8 (b) S = 1 (c) S = 1.2 at the x-z plane along AB line (y = 5 mm) at (Ma_{T} = 5 × 10^3).

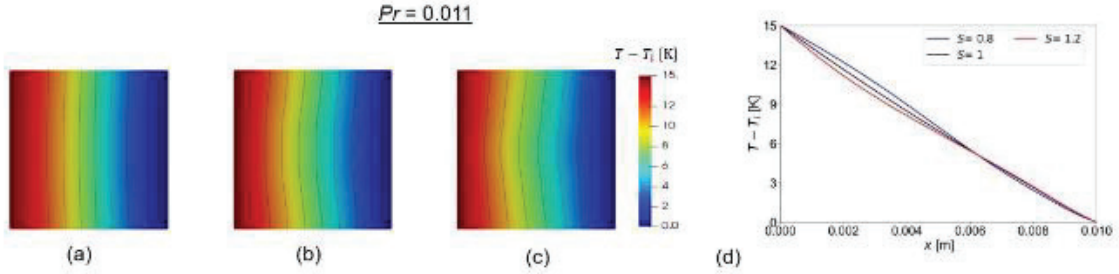

Figure 4.4 Snapshots of isotherms lines for (a) S = 0.8 (b) S = 1 (c) S = 1.2 and (d) temperature distribution along the AB line for all volume ratios at the x-y plane near the bottom surface (z = 0.1 mm) at ($Ma_{\mathrm{T}} = 1.5 \times 10^5$).

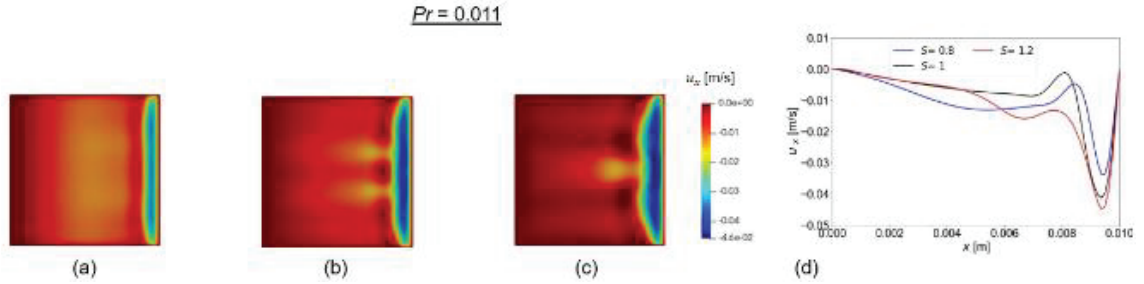

Figure 4.5 Snapshots of the x-direction flow velocity for (a) S = 0.8 (b) S = 1 (c) S = 1.2 and (d) the x-direction velocity distribution along the AB line for all volume ratios at the x-y plane near the bottom surface (z = 0.1 mm) at ($Ma_{\mathrm{T}} = 1.5 \times 10^5$).

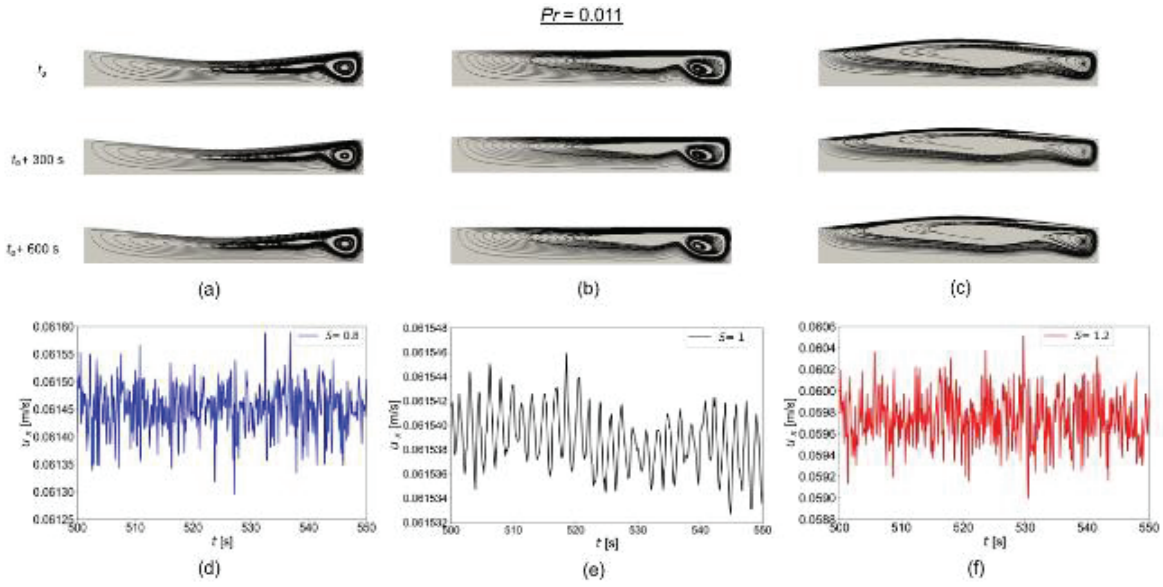

Figure 4.6 Snapshots of streamlines for (a) S = 0.8 (b) S = 1 (c) S = 1.2 at the x-z plane along AB line (y = 5 mm) and (d), (e), (f) the x-direction flow velocity at free surface sampling points for three

volume ratios ((S = 0.8; 5 mm, 5 mm, 0.7 mm), (S = 1; 5 mm, 5 mm, 1 mm), (S = 1.2; 5 mm, 5 mm, 1.3 mm)) in time difference (from (t_0 + 300 s) to (t_0 + 600 s)) at ($Ma_T = 1.5 \times 10^5$).

4.2 Effect of volume ratio under the thermo-solutal Marangoni convection for low *Pr* number fluids

Figure 4.7 shows the effect of volume ratio on the iso-concentration lines near the bottom surface (z = 0.1 mm) when $Ma_C = 1\times10^4$, $Ma_T = 5\times10^3$, Pr = 0.011 and Sc = 4.85. In this case, the flow is under steady conditions. As shown in Figure 4.7, the width of iso-concentration lines near the right wall (low concentration) becomes narrower as the volume ratio increases.

Figure 4.8 shows the effect of volume ratio on concentration distribution and that the concentration drop between the left-side wall and the middle region is approximately the same for all volume ratios. On the other hand, the linear decrease of the concentration drop occurs on the opposite side between the middle region and the right-side wall and is strongly affected by the volume ratio. Further, it is noted that concentration gradient deformation increased in opposite directions when increasing concave and convex free surface shapes with respect to the flat free surface as shown in Figure 4.8. As a result, there is an increase in non-uniform concentration distribution with increasing concavity and convexity shapes of the free surface. When Figure 4.1 (a-c) is compared with Figure 4.7 (b, d, f) for the low Pr number fluid in the same Ma_T value ($Ma_T = 5\times10^3$), iso-concentration lines deform more than isotherms lines. This result shows that the effect of volume ratio on concentration distribution is higher than that on temperature distribution in the liquid (Figure 4.1 (d) and Figure 4.8).

Figure 4.9 shows the effect of volume ratio on the x-direction flow velocity distribution. The flow direction is from the low concentration region to the high concentration region on the free surface; after that, the return flow develops in the direction from the high concentration region to the low concentration region near the bottom surface (due to the mass conservation) since the flow is confined within the cavity [94]. This return flow was observed in all volume

ratios near the bottom surface with positive velocity values, as illustrated in Figure 4.9. Figure 4.10 shows x-direction flow velocity distribution near the bottom surface, and Figure 4.11 shows the streamlines in the liquid. As shown in Figure 4.10, velocity near the bottom decreases as S increases because the width of streamlines increases as S increases as shown in Figure 4.11. Also, streamlines in Figure 4.11 are deformed by solutal effect compared with those in Figure 4.3 (pure thermal case). As shown in Figure 4.11, the deformation rate shows the minimum when $S = 1$. Consequently, the x-direction velocity becomes uniform, as shown in Figure 4.9 and 4.10.

Figure 4.12 shows effect of volume ratios on the x-direction flow velocity distribution under unsteady condition. That result shows more uniform flow distribution appears when $S = 1$ compared with those when $S = 0.8$ and $S = 1.2$.

Figure 4.13 shows time dependency of velocity at each sampling point. Table 4.1 shows the average frequency and amplitude corresponding to Figure 4.13. The concave shape ($S = 0.8$) leads to high inertia, resulting in a low amplitude with a high frequency of flow velocity fluctuations and more irregular patterns. Increasing volume ratio, lower frequency and higher amplitude might cause more significant but less frequent velocity variations. Therefore, higher amplitudes at larger volume ratios could introduce more significant velocity gradients, affecting process stability.

Figure 4.14 shows the effect of volume ratio on iso-concentration under an unsteady concentration field near the bottom surface in the case of higher Marangoni numbers ($Ma_{\mathrm{C}} = 3\times10^4$ and $Ma_{\mathrm{T}} = 1\times10^4$). As shown in Figure 4.14 the iso-concentration lines' deformation decrease in the cases of $S = 0.8$, $S = 1$, and then $S = 1.2$, respectively. Figure 4.15 shows the time dependency of concentration at each sampling point. Table 4.2 shows the average frequency and amplitude corresponding to Figure 4.15. A concave free surface shape ($S = 0.8$) leads to high frequency and lower amplitude, creating rapid disturbances that could promote the non-uniform solute distribution seen in the figure. At the large volume ratio, lower frequency and higher amplitude result in less solute distribution changes. Higher

amplitudes at the large volume ratio may introduce more uniform concentration gradients, affecting the growth process's stability. When compared with Figure 4.13 and Figure 4.15, at the free surface, Marangoni effects can drive significant fluid motion and contribute to high velocity fluctuations, this, in turn, leads to smoother concentration profiles due to better mixing. On the other hand, near the bottom surface, the bottom wall surface effects (no-slip condition) reduce the fluid's mobility, leading to lower flow velocity fluctuations but higher concentration fluctuations due to mass transport balance, enhancing the non-uniform mixing. Therefore, these effects on flow velocity are induced by concentration variations.

Figure 4.16 shows the effect of volume ratio on the flow structure under unsteady conditions. Although the number of vortices changes with time, the vortex cells in the liquid phase are observed in cases of different *S*, as shown in Figure 4.16. Vortices are often associated with complex flow phenomena and flow strength. As the number of vortices increases, a more uneven and irregular flow field is observed [63]. Therefore, Figure 4.16 shows the streamlines showing multiple vortices with less organized flow patterns for the concave free shape (S = 0.8), which indicates stronger local instabilities and complex Marangoni flow (Figure 4.16 (a)). The streamlines are more organized, with fewer vortices for the flat free shape (S = 1), which indicates a more balanced and stable flow (Figure 4.16 (b)). For the convex free shape (S = 1.2), the streamline size becomes large, well-defined vortices with organized flow patterns, indicating a stable and dominant flow structure than concave shape (Figure 4.16 (c)). Figure 4.16 shows that across all volume ratios, vortex cells have a more dynamic movement in the upper region compared to the lower region, with streamlines appearing denser in the upper region. This suggests high fluctuations in velocity and larger average velocity amplitudes at the free surface compared to the near the bottom (detailed in Table 4.1 and Figure 4.13). Forming pronounced streamline configurations and vortex formations at the free surface enhances mixing efficiency. Consequently, this enhanced mixing leads to a more homogenized concentration distribution at the free surface than near the bottom surface (detailed in Table 4.2 and Figure 4.15).

These observations highlight the critical role of volume ratio and free surface shape in determining the stability and dynamics of both concentration and velocity fields in Marangoni convection systems.

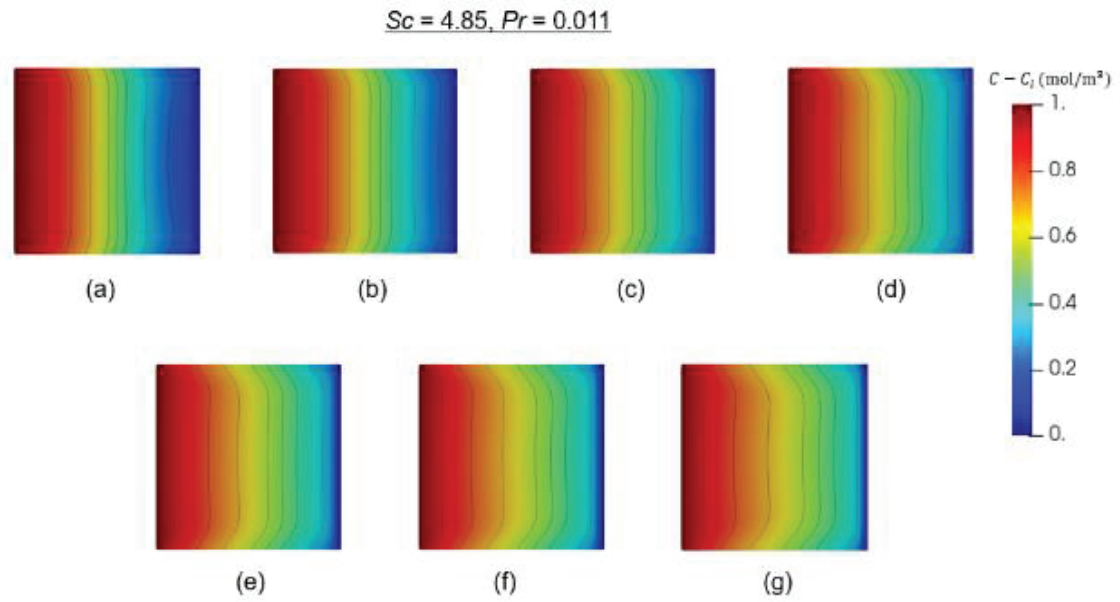

Figure 4.7 The iso-concentration lines for (a) $S = 0.7$ (b) $S = 0.8$ (c) $S = 0.9$ (d) $S = 1$ (e) $S = 1.1$ (f) $S = 1.2$ (g) $S = 1.3$ at the x-y plane near the bottom surface ($z = 0.1$ mm) at $(Ma_C, Ma_T) = (1 \times 10^4, 5 \times 10^3)$.

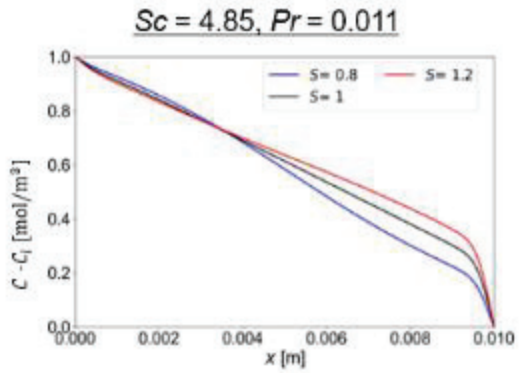

Figure 4.8 Concentration distributions for all volume ratios along the AB line at the x-y plane near the bottom surface ($z = 0.1$ mm) at $(Ma_C, Ma_T) = (1 \times 10^4, 5 \times 10^3)$.

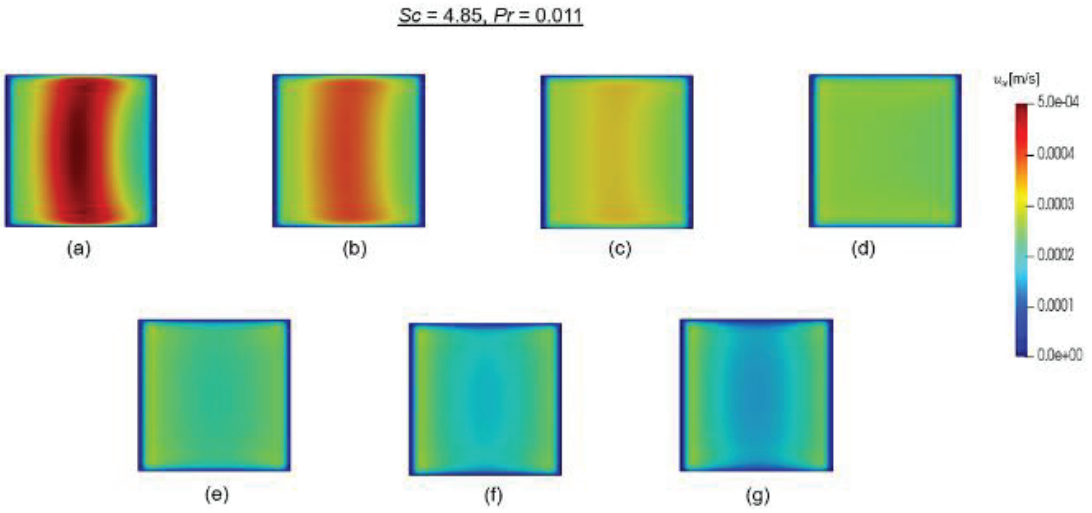

Figure 4.9 The *x*-direction flow velocity for (a) $S = 0.8$ (b) $S = 1$ (c) $S = 1.2$ and (d) the *x*-direction velocity distribution along the AB line for all volume ratios at the *x*-*y* plane near the bottom surface ($z = 0.1$ mm) at $(Ma_C, Ma_T) = (1 \times 10^4, 5 \times 10^3)$.

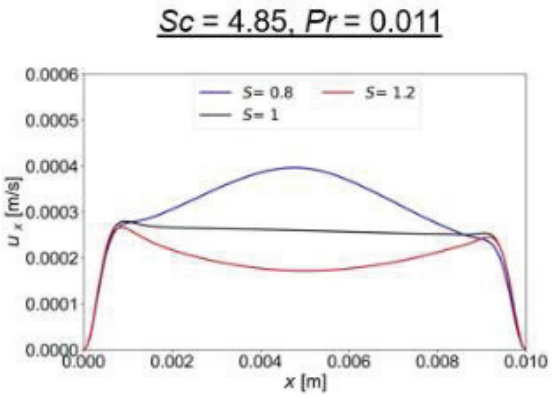

Figure 4.10 The *x*-direction flow velocity distribution respect with the flat shape along the AB line at the *x*-*y* plane near the bottom surface ($z = 0.1$ mm) at $(Ma_C, Ma_T) = (1 \times 10^4, 5 \times 10^3)$.

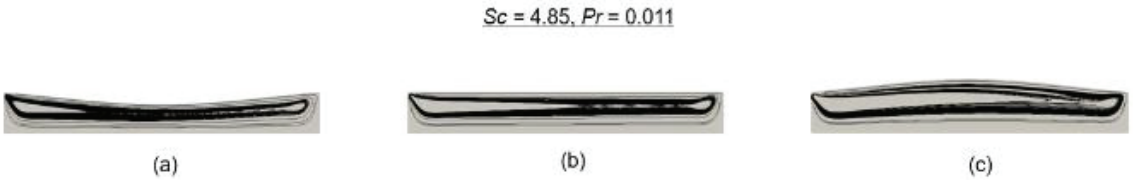

Figure 4.11 The streamlines for (a) S = 0.8 (b) S = 1 (c) S = 1.2 at the x-z plane along AB line (y = 5 mm) at (Ma_C, Ma_T = 1×10^4, 5×10^3).

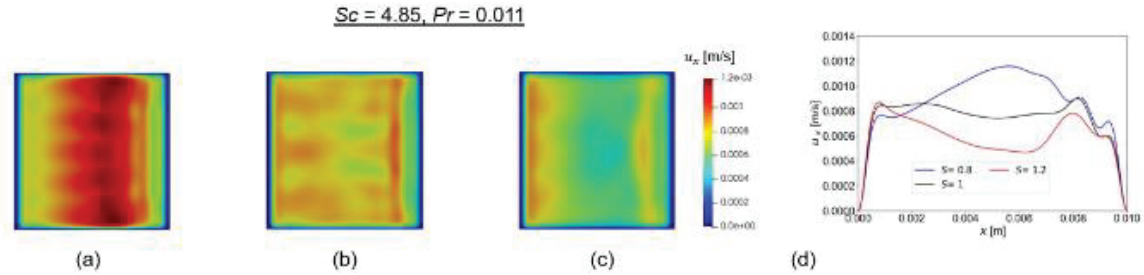

Figure 4.12 Snapshots of the x-direction flow velocity for (a) S = 0.8 (b) S = 1 (c) S = 1.2 and (d) the x-direction velocity distribution along the AB line for all volume ratios at the x-y plane near the bottom surface (z = 0.1 mm) at (Ma_C, Ma_T) = (3×10^4, 1×10^4).

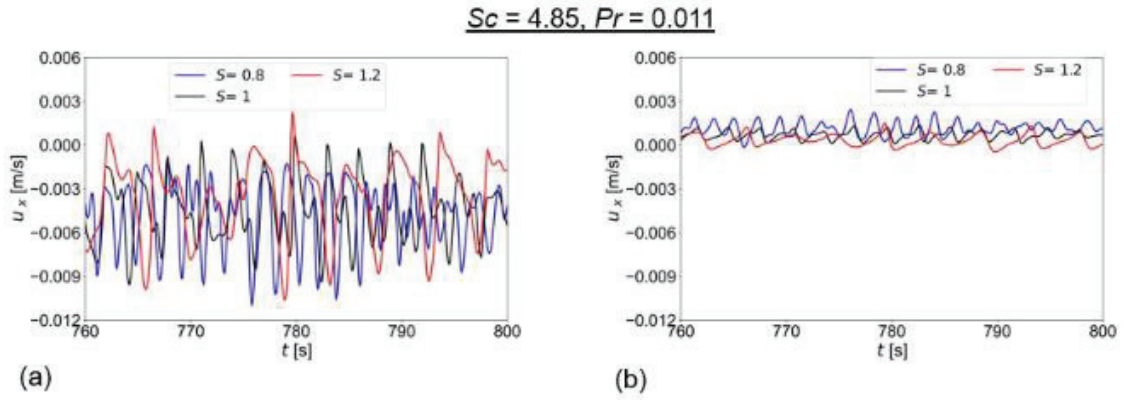

Figure 4.13 The x-direction flow velocity distribution at (Ma_C, Ma_T) = (3×10^4, 1×10^4) for three volume ratios (S), (a) free surfaces sampling points; ((S = 1.2; 5 mm, 5 mm, 1.3 mm), (S = 1; 5 mm, 5 mm, 1 mm), (S = 0.8; 5 mm, 5 mm, 0.7 mm)) and (b) near the bottom surfaces sampling point; (5 mm, 5 mm, 0.1 mm).

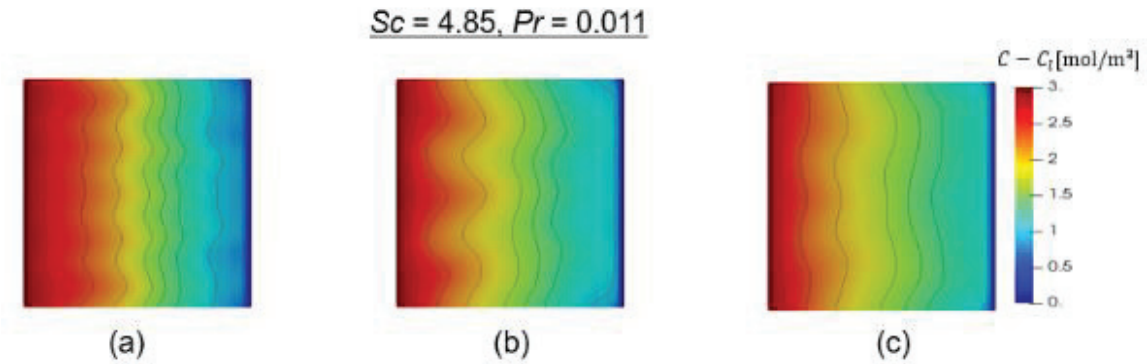

Figure 4.14 Snapshots of iso-concentration lines for (a) $S = 0.8$ (b) $S = 1$ (c) $S = 1.2$ at the x-y plane near the bottom surface ($z = 0.1$ mm) at $(Ma_C, Ma_T) = (3 \times 10^4, 1 \times 10^4)$.

Table 4.1 Average frequency (f_{avg}) and amplitude (a_{avg}) of velocity variation in free surface and near bottom sampling points corresponding to Figure 4.13.

Free surface	$S = 0.8$	$S = 1$	$S = 1.2$
(a) f_{avg} (Hz)	0.49000	0.32800	0.22500
(b) a_{avg}(m/s)	0.00314	0.00364	0.00430
Near bottom surface			
(a) f_{avg} (Hz)	0.51000	0.32900	0.22900
(b) a_{avg}(m/s)	0.00059	0.00047	0.00062

Table 4.2 Average frequency (f_{avg}) and amplitude (a_{avg}) of velocity variation in free surface and near bottom sampling points corresponding to Figure 4.15.

Free surface	$S = 0.8$	$S = 1$	$S = 1.2$
(a) f_{avg} (Hz)	0.55000	0.31300	0.22000
(b) a_{avg} (mol/m^3)	0.05700	0.07500	0.12200
Near bottom surface			
(a) f_{avg} (Hz)	0.49000	0.30700	0.21700
(b) a_{avg} (mol/m^3)	0.16700	0.20400	0.27000

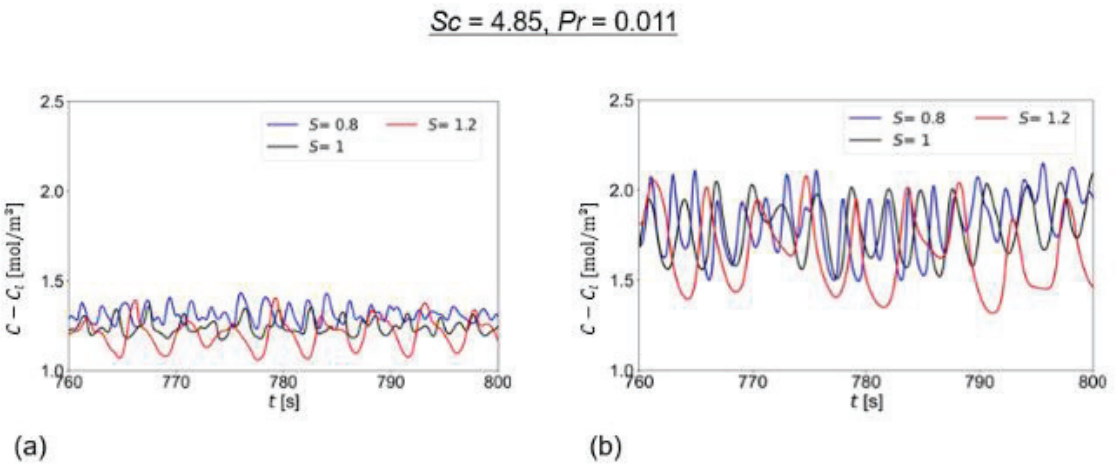

Figure 4.15 Concentration distribution at (Ma_C, Ma_T) = (3 × 10^4, 1 × 10^4) for three volume ratios (S), (a) free surfaces sampling points; ((S = 1.2; 5 mm, 5 mm, 1.3 mm), (S = 1; 5 mm, 5 mm, 1 mm), (S = 0.8; 5 mm, 5 mm, 0.7 mm)) and (b) near the bottom surfaces sampling point; (5 mm, 5 mm, 0.1 mm).

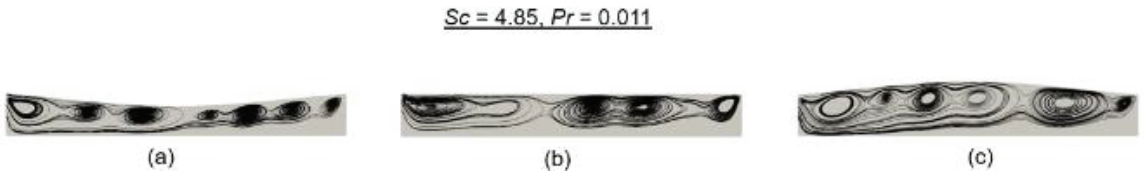

Figure 4.16 Snapshots of streamlines for (a) S = 0.8 (b) S = 1 (c) S = 1.2 at the x-z plane along AB line (y = 5 mm) at (Ma_C, Ma_T) = (3 × 10^4, 1 × 10^4).

4.3 Effect of volume ratio under thermal Marangoni convection for high *Pr* number fluids

Figure 4.17 shows the effect of volume ratio on the iso-thermal lines near the bottom surface and temperature distribution under steady conditions (Ma_T = 5×10^3). Because of the high Pr number, temperature distribution strongly depends on S compared with that in Figure 4.1.

Figure 4.18 shows the effect of volume ratio on the flow field, the x-direction flow velocity. For all volume ratios, the x-direction flow velocity values are negative, indicating a return flow of the thermal Marangoni convection near the bottom surface. The S = 0.8 and S = 1.2

cases lead to the x-direction non-uniform flow velocity distribution due to the developing uneven temperature gradient within curvature regions, as shown in Figure 4.18 (a-c). Furthermore, the maximum return flow velocity is observed in the middle region, and low velocity values observed near the side walls in the $S = 0.8$ case, as shown in Figure 4.18 (a). However, in the $S = 1.2$ case a low velocity return flow is observed in the middle region, and a high velocity flow is observed near the side wall, as shown in Figure 4.18 (c). Figure 4.18 (d) displays the deviations in the velocity distribution at the x-directional flow depending on the volume ratio. It is clearly seen that the flow strength variations occur due to deformed free surfaces. Figure 4.19 shows the streamlines in each case. For a high-volume ratio, streamlines expand across the domain.

Figure 4.20 (a-c) shows the effect of volume ratio on iso-thermal lines near the bottom surface ($z = 0.1$ mm) under the unsteady condition ($Ma_{\mathrm{T}} = 1.5\times10^{4}$). Under unsteady conditions, the spatial period of temperature fluctuations varies with volume ratio due to changes in temperature gradient and free surface shape. The isotherms are closer in the case of $S = 0.8$ (concave), indicating a steep gradient and frequent fluctuations with a shorter spatial period. The isotherms are moderately spaced at $S = 1$ case (flat free surface), reflecting a balanced gradient and intermediate fluctuations. The isotherms are further apart for $S = 1.2$ case (convex), indicating a shallow gradient and less frequent fluctuations with a longer spatial period. These differences are driven by the varying flow stability and local instabilities influenced by the free surface shape at each volume ratio. Additionally, Figure 4.20 (d) illustrates the temperature distribution (T) between the side walls. The temperature distribution deformation increases in the cases of $S = 0.8$, $S = 1$, and then $S = 1.2$, respectively. When isotherms are relatively closer, indicating a steeper temperature gradient, creating a more linear and uniform temperature distribution for $S = 0.8$ cases. This is due to the stronger influence of thermal Marangoni convection, which stabilizes the temperature field. The linear temperature trend disappears in the middle region for the $S = 1$, then $S = 1.2$ cases under unsteady conditions. In conclusion, the volume ratio affects the temperature field, causing non-uniform temperature distributions (variation in temperature distribution) in the liquid.

Figure 4.21 shows the effect of volume ratio on the x-direction flow velocity at Ma_{T} = 1.5 $\times 10^4$ near the bottom surface (z = 0.1 mm). Figure 4.21 (a-c) shows that the x-direction velocity in all cases is of non-uniform distribution, promoting uneven temperature gradient along the free surface in the unsteady condition. Moreover, Figure 4.21 (a) shows the maximum flow velocity in the middle region, with lower velocity flow near the right-side wall in the case of S = 0.8, consistent with the steady condition scenario. However, the non-uniform return flow increases at the higher volume ratio (Figure 4.21 (b) and (c)). Figure 4.21 (d) illustrates the unsteady x-directional flow distribution in the cases of S = 0.8 and S = 1.2 compared to the case S = 1 near the bottom surface. Flow deflection is observed near the hot wall for all volume ratios and increases with the volume ratio. Notably, the x-direction flow velocity oscillatory fluctuation decreases towards the cold wall for the case of S = 1 compared to the case of S = 1.2 in the middle region. In the case of S = 1.2, the flow becomes further non-uniformed compared to the cases of S = 0.8 and S = 1. The differences in flow patterns among the cases of S = 0.8, S = 1.0, and S = 1.2 are due to the influence of free surface shape on local instabilities and temperature distribution. At S = 1.2, we observe stronger temperature gradients, enhanced local instabilities and a stronger Marangoni convection, resulting in dynamic and irregular flow patterns in the cavity. Conversely, in the cases of concave (S = 0.8) and flat free surfaces (S = 1) we see weaker temperature gradients and more stable flow patterns. These observations are crucial for understanding the impact of surface shape on flow dynamics in the case of unsteady thermal Marangoni convection.

Figure 4.22 shows the effect of volume ratio on streamlines under unsteady condition (Ma_{T} = 1.5×10^4) for Pr = 6.7 fluid. The number of vortex cells are different at different volume ratios. As a result, the high volume ratio makes the flow more complex and increases the flow strength.

When comparing low and high Pr fluids under unsteady Marangoni conditions, the non-uniform temperature and velocity distributions are more pronounced at the low Marangoni numbers in high Pr fluids than in low Pr fluids (Figures 4.20, 4.21, 4.4, 4.5).

Since the volume ratio affects flow velocity and temperature distributions under both steady and unsteady conditions, it must also affect the concentration distribution under the same conditions. Thus, the following section discusses the effect of volume ratio on thermo-solutal Marangoni convection in high *Pr* number fluids.

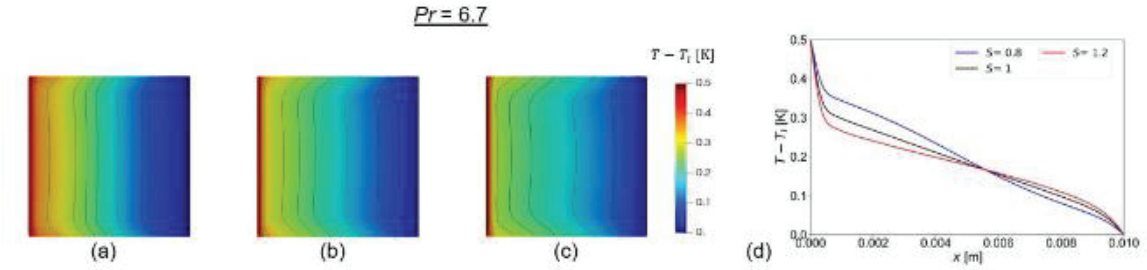

Figure 4.17 The isotherms lines for (a) S = 0.8 (b) S = 1 (c) S = 1.2 and (d) temperature distribution along the AB line for all volume ratios at the x-y plane near the bottom surface (z = 0.1 mm) at (Ma_{T} = 5 × 10^3).

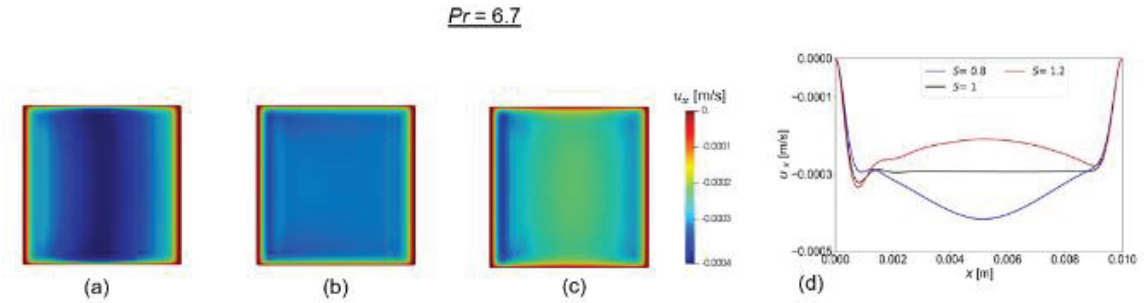

Figure 4.18 The x-direction flow velocity for (a) S = 0.8 (b) S = 1 (c) S = 1.2 and (d) x-direction velocity distribution along the AB line for all volume ratios at the x-y plane near the bottom surface (z = 0.1 mm) at (Ma_{T} = 5 × 10^3).

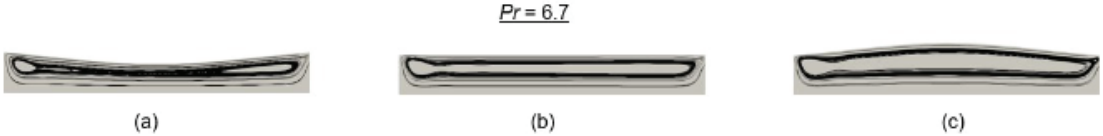

Figure 4.19 The streamlines for (a) S = 0.8 (b) S = 1 (c) S = 1.2 at the x-z plane along AB line (y = 5 mm) at (Ma_{T} = 5 × 10^3).

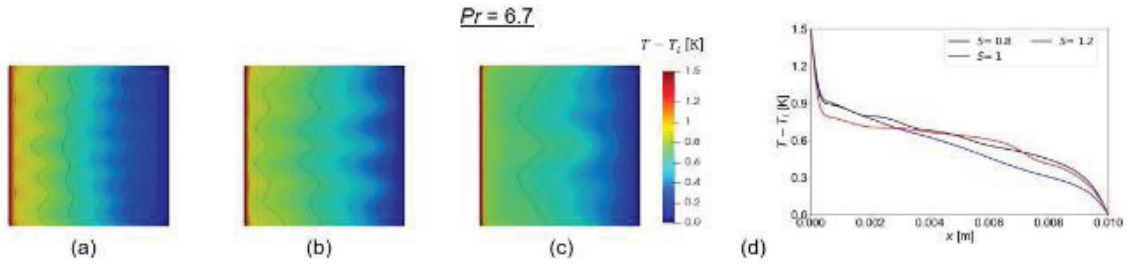

Figure 4.20 Snapshots of isotherms lines for (a) S = 0.8 (b) S = 1 (c) S = 1.2 and (d) temperature distribution along the AB line for all volume ratios at the x-y plane near the bottom surface (z = 0.1 mm) at ($Ma_{\mathrm{T}} = 1.5 \times 10^4$).

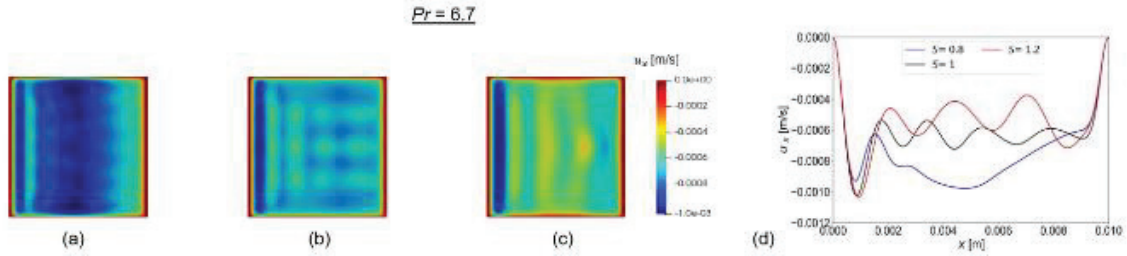

Figure 4.21 Snapshots of the x-direction flow velocity for (a) S = 0.8 (b) S = 1 (c) S = 1.2 and (d) the x-direction velocity distribution along the AB line for all volume ratios at the x-y plane near the bottom surface (z = 0.1 mm) at ($Ma_{\mathrm{T}} = 1.5 \times 10^4$).

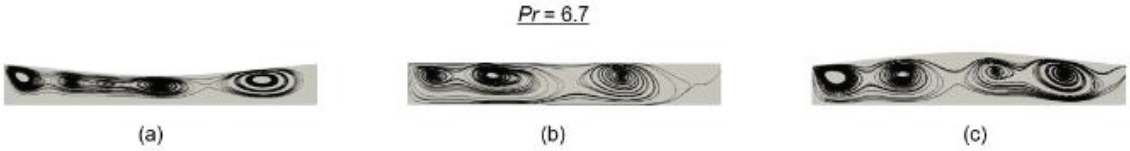

Figure 4.22 Snapshots of streamlines for (a) S = 0.8 (b) S = 1 (c) S = 1.2 at the x-z plane along AB line (y = 5 mm) at ($Ma_{\mathrm{T}} = 1.5 \times 10^4$).

4.4 Effect of volume ratio under the thermo-solutal Marangoni convection for high *Pr* number fluids

Figure 4.23 (a-c) shows the effect of volume ratio on solutal Marangoni flow in the high *Pr* number fluids in a steady condition (Ma_C = 1×10^4, Ma_T = 5×10^3). The snapshots of iso-concentration lines of the basic flow are shown for all volume ratios near the bottom surface (z = 0.1 mm).

Furthermore, Figure 4.23 (d) shows a drop in concentration between the side walls for the *Pr* = 6.7 (with *Sc* = 4.85) fluid. A bending angle of concentration drop occurs in the cases of *S* = 0.8, *S* = 1.2, and a linear decrease is seen in the case of *S* = 1 in the middle region. When comparing temperature and concentration distributions in a high *Pr* fluid with the same Ma_T value (Ma_T = 5×10^3), Figure 4.17 (a-c) and Figure 4.23 (a-c) show isotherms lines and iso-concentration lines with deformation in opposite directions due to the development of concentration and temperature return flows near the bottom surface.

Figure 4.24 (a-c) shows the effect of volume ratio on the x-direction flow velocity distribution at Ma_C = 1×10^4, Ma_T = 5×10^3 under the steady condition near the bottom surface (z = 0.1 mm). Figure 4.24 (d) illustrates that a non-uniform flow distribution is observed, varied between side walls. Furthermore, it promotes variations in the flow strength as shown in the cases of *S* = 0.8 and *S* = 1.2. Comparison of the flow velocity distributions in Figure 4.24 (a-c) and Figure 4.18 (a-c) shows that the solutal Marangoni effect weakens thermal Marangoni flow and flow direction becomes opposite due to high Ma_C value. In Figure 4.24 (d) and Figure 4.18 (d), the positive and negative valued *x*-direction flow velocity indicate a return flow with a direction change between the solutal and thermal Marangoni flows near the bottom surface. Therefore, we can conclude that the effect of volume ratio plays a vital role in flow velocity distribution in the case of *Sc* = 4.85 with *Pr* = 6.7 fluid under the steady Marangoni condition. Figure 4.25 shows streamlines in the middle region in each case, and the distribution of streamlines changes with the volume ratio.

Figure 4.26 shows the effect of volume ratio on the x-direction flow velocity under unsteady conditions (Ma_C = 3×10^4, Ma_T = 1×10^4). The flow fluctuations seen in Figure 4.26 (d) are due to the effect of volume ratio. A uniform flow distribution is observed in the case of flat free surface (S = 1), compared with the large volume ratio (S = 1.2). Furthermore, in sampling points of the x-direction flow velocity distribution at the free surface and near the bottom surface, the flow velocity exhibits an oscillatory pattern in the case of Pr = 6.7 with Sc = 4.85 number fluid in each sampling point for all three volume ratios, as shown in Figure 4.27. The amplitude and frequency of flow velocity fluctuations are significantly influenced by the volume ratio (S). Table 4.3 presents the average frequency and amplitude corresponding to Figure 4.27. Results reveal that the high amplitude and lower frequency flow velocity distributions occur in the cases higher values of (S). The lower frequency and high amplitude observed near the bottom surface and at the free surface in the cases of S = 1 and S = 1.2 indicate stronger flow velocity gradients. In contrast, the concave shape at S = 0.8 leads to a strong local Marangoni convection that rapidly dissipates flow velocity fluctuations, giving rise to higher frequency and lower amplitude fluctuations. Higher amplitudes in the cases of larger volume ratios could introduce stronger velocity gradients and affect the process stability. One then can conclude that the selection of proper volume ratio is essential in maintaining stability and achieving high-quality thin films. Furthermore, comparing Figure 4.13 and Figure 4.27, the significant change in the Prandtl number implies a substantial difference in thermal diffusivity relative to momentum diffusivity. Figure 4.13 shows that the flow velocity profiles across all volume ratios exhibit more pronounced fluctuations over time, suggesting a more complex quasi-periodic flow structure. Figure 4.27 shows that the fluctuations in velocity profiles appear dampened compared to Figure 4.13, which might be due to the high Prandtl number. This indicates a fluid with a tendency to oscillatory flow and more stable velocity fluctuation. A higher Prandtl number fluid (Table 4.3) generally corresponds to slightly lower frequencies at equivalent volume ratios than a low Prandtl number fluid (Table 4.1). This supports observing more uniform flow fluctuation with reducing flow disturbances, as shown in Figure 4.27.

Figure 4.28 shows snapshots of iso-concentration lines in an unsteady condition near the bottom surface (z = 0.1 mm) at $Ma_C = 3\times10^4$, $Ma_T = 1\times10^4$. The concentrations at the free surface sampling points of ((S = 1.2; 5 mm, 5 mm, 1.3 mm), (S = 1; 5 mm, 5 mm, 1 mm), (S = 0.8; 5 mm, 5 mm, 0.7 mm)) and near bottom surface sampling point (5 mm, 5 mm, 0.1 mm) are examined. The concentration fluctuations become oscillatory as seen in Figure 4.29. Comparing Figure 4.27 and Figure 4.29, we see that the flow velocity fluctuations are induced by concentration variations near the bottom and top free surfaces. The same is observed in the case of *Sc* = 4.85 with *Pr* = 0.011 fluid as mentioned in Section 4.2. Table 4.4 presents the average frequency and amplitude values corresponding to Figure 4.29. It reveals that the stronger local Marangoni convection in the case of S = 0.8 leads to steeper concentration gradients. These gradients, however, are rapidly dissipated, resulting in higher frequency and lower amplitude fluctuations. For the higher volume ratios, the balanced Marangoni convection maintains significant concentration gradients without dissipating them rapidly. This leads to lower frequency and high amplitude fluctuations as the system tries to equilibrate the concentration distribution. Higher amplitudes in the cases of S = 1 and S = 1.2 could introduce more significant concentration gradients. These uniformly distributed concentration gradients may affect the process stability more than that in S = 0.8. The higher amplitude fluctuations are observed on both the top free surface and near the bottom surface in both cases of S = 1 and S = 1.2. This implies that the volume ratio impacts the concentration distribution with more pronounced uniform fluctuations on the top free surface and near the bottom surface in the unsteady Marangoni convection. When comparing concentration distributions in Figure 4.15 and Figure 4.29, the low *Pr* number fluids show more complex flow structures than those in high *Pr* number fluids. However, in both cases, the higher average amplitudes are observed as the volume ratio increases, regardless of the Prandtl number. This indicates that at the high-volume ratio uniform concentration gradients are maintained (Table 4.2 and Table 4.4). The difference observed in the cases of low and high Prandtl number fluids (between Figure 4.15 and Figure 4.29) shows that the flow pattern change is due to changing heat transfer relative to momentum transfer. A high *Sc* and high *Pr* number fluid develops a weaker heat transfer with an efficient solute transport, leading to

a homogeneous concentration distribution. Therefore, the average amplitude is higher (higher Prandtl number) in Table 4.4, allowing for significant variations leading to uniform flow fluctuations.

Figure 4.30 shows streamlines under unsteady conditions (Ma_C = 3×10^4, Ma_T = 1×10^4) for *Pr* = 6.7 with *Sc* = 4.85 fluid a low number of vortex cells appeared in the flow structure in all volume ratios in the case of *Pr* = 6.7 with *Sc* = 4.85 fluid. This is a snapshot of the flow structure, and the number of vortex cells must be changed as a function of time. Therefore, less complex flow phenomena appeared in the case of *Pr* = 6.7 with *Sc* = 4.85 fluid. Comparing solutal Marangoni flows in Figure 4.16 and Figure 4.30, the low *Pr* number fluid shows more non-uniform and complex flow patterns, while the high *Pr* number fluid in more organized and stable flow fluctuations in the unsteady Marangoni condition. Also, the volume ratio impacts these structures by either enhancing local flow instabilities (lower volume ratios) or stabilizing the flow (flat and high volume ratios).

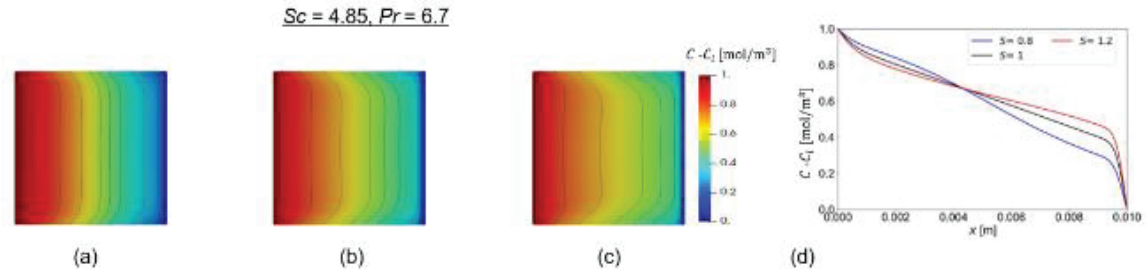

Figure 4.23 The iso-concentration lines for (a) *S* = 0.8 (b) *S* = 1 (c), *S* = 1.2 and (d) concentration gradient along the AB line for all volume ratios at the *x*-*y* plane near the bottom surface (*z* = 0.1 mm) at (Ma_C = 1 × 10^4, Ma_T = 5 × 10^3).

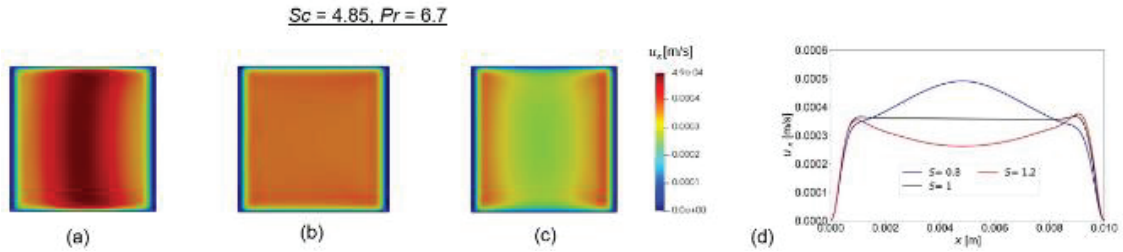

Figure 4.24 The *x*-direction flow velocity for (a) S = 0.8 (b) S = 1 (c) S = 1.2 and (d) *x*-direction velocity distribution along the AB line for all volume ratios at the *x-y* plane near the bottom surface (z = 0.1 mm) at (Ma_{C} = 1 × 10^4, Ma_{T} = 5 × 10^3).

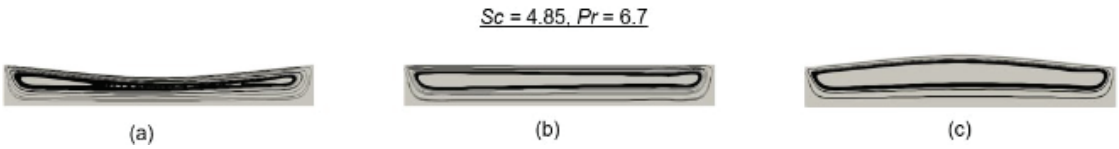

Figure 4.25 The streamlines for (a) S = 0.8 (b) S = 1 (c) S = 1.2 at the *x-z* plane along AB line (y = 5 mm) at (Ma_{C}, Ma_{T}) = (1 × 10^4, 5 × 10^3).

Table 4.3 Average frequency (f_{avg}) and amplitude (a_{avg}) of velocity variation in free surface and near bottom sampling points corresponding to Figure 4.27.

Free surface	S = 0.8	S = 1	S = 1.2
(a) f_{avg} (Hz)	0.4130	0.3180	0.2890
(b) a_{avg} (m/s)	0.0030	0.0035	0.0043
Near bottom surface			
(a) f_{avg} (Hz)	0.4100	0.3158	0.2920
(b) a_{avg} (m/s)	0.0005	0.0006	0.0007

Table 4.4 Average frequency (f_{avg}) and amplitude (a_{avg}) of velocity variation in free surface and near bottom sampling points corresponding to Figure 4.29.

Free surface	S = 0.8	S = 1	S = 1.2
(a) f_{avg} (Hz)	0.4280	0.3100	0.2910
(b) a_{avg} (mol/m^3)	0.0756	0.1536	0.1340
Near bottom surface			
(a) f_{avg} (Hz)	0.4290	0.3100	0.2920
(b) a_{avg} (mol/m^3)	0.1950	0.2660	0.2400

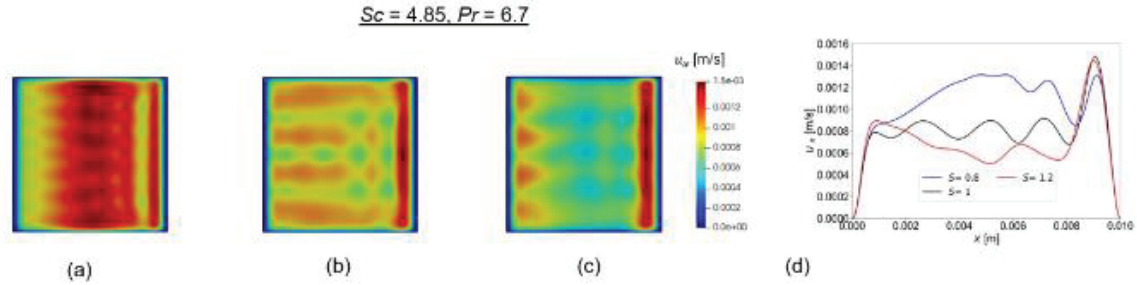

Figure 4.26 Snapshots of the x-direction flow velocity for (a) $S = 0.8$ (b) $S = 1$ (c) $S = 1.2$ and (d) the x-direction velocity distribution along the AB line for all volume ratios at the x-y plane near the bottom surface ($z = 0.1$ mm) at ($Ma_C = 3 \times 10^4$, $Ma_T = 1{\times}10^4$).

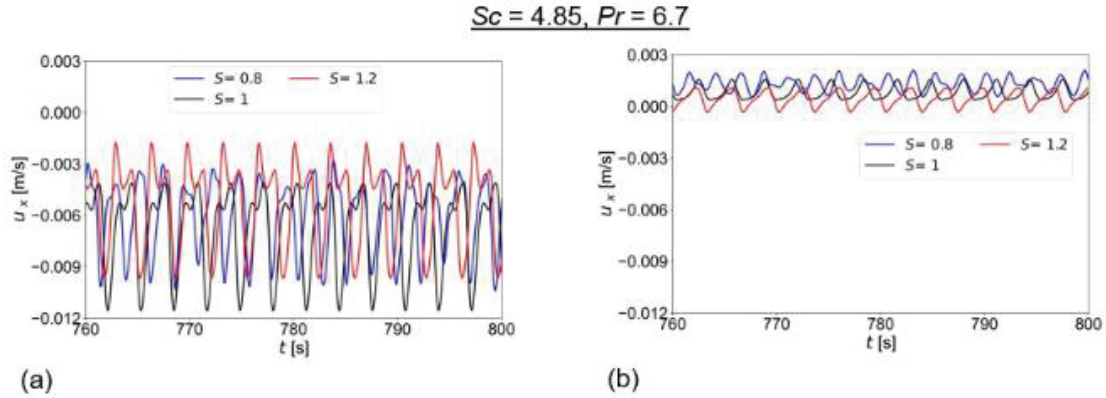

Figure 4.27 the x-direction flow velocity distribution at ($Ma_C = 3 \times 10^4$, $Ma_T = 1{\times}10^4$) for three volume ratios (S), (a) free surfaces sampling points; (($S = 1.2$; 5 mm, 5 mm, 1.3 mm), ($S = 1$; 5 mm, 5 mm, 1 mm), ($S = 0.8$; 5 mm, 5 mm, 0.7 mm)) and (b) near the bottom surfaces sampling point; (5 mm, 5 mm, 0.1 mm).

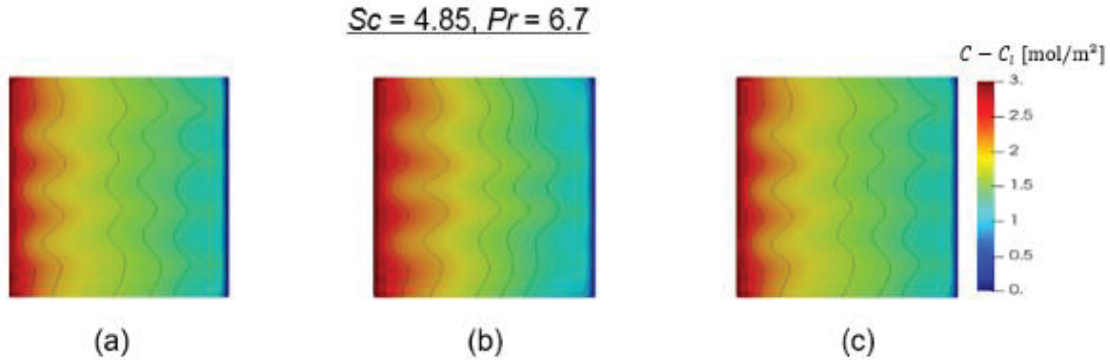

Figure 4.28 Snapshots of iso-concentration lines for (a) $S = 0.8$ (b) $S = 1$ (c) $S = 1.2$ at the x-y plane near the bottom surface ($z = 0.1$ mm) at ($Ma_C = 3 \times 10^4$, $Ma_T = 1{\times}10^4$).

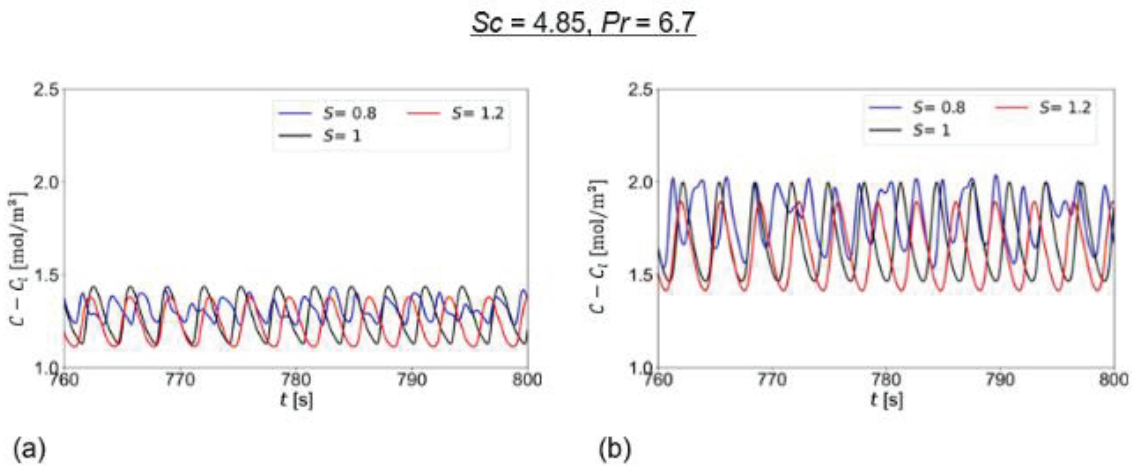

Figure 4.29 Concentration distribution at (Ma_C = 3 × 10^4, Ma_T = 1×10^4) for three volume ratios (S), (a) free surfaces sampling points; ((S = 1.2; 5 mm, 5 mm, 1.3 mm), (S = 1; 5 mm, 5 mm, 1 mm), (S = 0.8; 5 mm, 5 mm, 0.7 mm)) and (b) near the bottom surfaces sampling point; (5 mm, 5 mm, 0.1 mm).

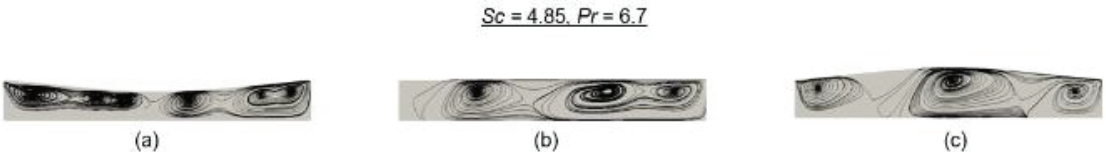

Figure 4.30 Snapshots of streamlines for (a) S = 0.8 (b) S = 1 (c) S = 1.2 at the x-z plane along AB line (y = 5 mm) at (Ma_C, Ma_T) = (3 × 10^4, 1 × 10^4).

CHAPTER 5

THE EFFECTS OF ZONE VOLUME AND GRAVITY ON THERMO-SOLUTAL MARANGONI CONVECTION INSTABILITY IN A HALF-ZONE MODEL OF FLOAT-ZONE GROWTH OF SiGe

In this chapter, numerical simulation of thermal and solutal Marangoni convection in a floating half zone with deformed free surface under normal gravity and zero gravity has been performed. The critical conditions of Marangoni convection for volume ratios under normal and zero gravity conditions are compared.

5.1 Relative contributions of thermal and solutal natural convective flows

In crystal growth from the liquid phase (melt and solution), the convective flows driven by temperature and concentration gradients in the liquid phase are called "thermal and solutal convections" respectively. Since the thermal convection is dominant, it is called simply "natural convection". If both gradients are present, the convective flow is called "thermo-solutal convection". These flows play an important role in crystal growth; beneficial or adverse, depending on the system. In most cases their adverse effects must be minimize for the growth of high-quality crystals. In SiGe growth by FZ, both convective flows are present. In this section, we examine their relative contributions by examining the associated dimensionless numbers. This is important to have a comprehensive understand of the transport structures in the FZ melt.

Here we focus on the solutal Rayleigh number, particularly examining its low value (Ra_{C} = 80) in the context of solutal natural convection in the absence of Marangoni flows (Ma_{C} = 0, Ma_{T} = 0) and also in their presence at the values of (Ma_{C} = 714, Ma_{T} = 1750), for comparison. The snapshots of the computed concentration field for S = 1.1 are depicted in Figure 5.1 (a-b). Results show that the solutal concentration distribution in the absence of Marangoni convection is negligible compared with the case where the Marangoni convection

is present. We also examine the case at a higher solutal Rayleigh number (Ra_C = 160). The computed concentration results, that are given in Figure 5.1 (c-d), show that the concentration distribution still remains negligible in the absence of Marangoni convection (Ma_C = 0, Ma_T = 0), but it is notable at the Marangoni convection conditions of (Ma_C = 1428, Ma_T = 3500).

Next we study the effect of pure thermal natural convection (Ma_C = 0, Ma_T = 0) by examining the snapshots of the computed concentration field for S =1.1 at a low thermal Rayleigh number (Ra_T = 239) under pure thermal natural convection (Ma_C = 0, Ma_T = 0) and also at the Marangoni convection conditions of (Ma_C = 714, Ma_T = 1750). The concentration distribution is notably weaker in the case of pure thermal natural convection compared to that of the Marangoni case of (Ma_C = 714, Ma_T = 1750), as illustrated in Figure 5.2 (a-b). At the high thermal Rayleigh number (Ra_T = 477.9), the concentration distribution is less pronounced in the case pure thermal natural convection (Ma_C = 0, Ma_T = 0) compared to the case at the Marangoni convection conditions of (Ma_C = 1428, Ma_T = 3500), as shown in Figure 5.2 (c-d). Figure 5.3 (a-b) presents the computed flow velocity under a low solutal Rayleigh number (Ra_C = 80). In the case of pure solutal natural convection (Ma_C = 0, Ma_T = 0) at a low solutal Rayleigh number, the strength of the flow velocity field is minimum in compared to that in the case where Marangoni convection is present (Ma_C = 714, Ma_T = 1750). Similarly, the flow velocity magnitude under a high solutal Rayleigh number (Ra_C = 160) is negligible in the case of pure solutal natural convection (Ma_C = 0, Ma_T = 0), but it is stronger in the presence of Marangoni convection (Ma_C = 1428, Ma_T = 3500) as shown in Figure 5.3 (c-d).

The flow velocity magnitude shown in Figure 5.4 (a-b) is for the case of a low thermal Rayleigh number (Ra_T = 239). As seen from the figure, at the low thermal Rayleigh number, the flow velocity magnitude is smaller in the case of pure thermal natural convection (Ma_C = 0, Ma_T = 0) compared that at the Marangoni convection condition of (Ma_C = 714, Ma_T = 1750). Figure 5.4 (c-d) illustrates the flow velocity field at a high thermal Rayleigh number (Ra_T = 477.9). In this case, the condition of pure thermal natural convection (Ma_C = 0, Ma_T

= 0) leads to weaker flow velocity strength compared to that in the case of Marangoni convection at (Ma_C = 1428, Ma_T = 3500).

Furthermore, the strength of buoyancy is measured by the dynamic Bond number (Bo_{dyn}). The small dynamic Bond number indicates that Marangoni forces are dominant with respect to buoyancy. Thus, in the presence of thermal natural convection cases, the calculated value of Bo_{dyn} = 0.1 shows that the flow is still dominated by Marangoni convection [9, 95].

We then conclude that the Marangoni forces dominate the flow strength in all three cases of volume ratios considered here, and the contribution of buoyancy is less significant. The strength of solutal natural convection appears negligible compared to that of Marangoni convection. Similarly, thermal natural convection has less impact on Marangoni convection than solutal natural convection. These findings are crucial for understanding and optimizing convective processes, especially in scenarios where Marangoni convection is a dominant factor influencing fluid dynamics. Therefore, the following results are obtained by considering only thermal natural convection together with Marangoni convection. The contribution of the solutal natural convection is not taken in account.

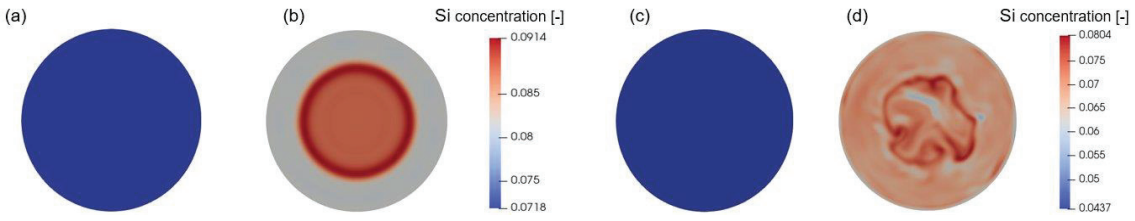

Figure 5.1 Snapshots of computed Si concentration distribution for S = 1.1 in the r-θ plane at z = 2.5 mm: (a) (Ma_C, Ma_T, Ra_C) = (0, 0, 80), (b) (Ma_C, Ma_T, Ra_C) = (714, 1750, 80), (c) (Ma_C, Ma_T, Ra_C) = (0, 0, 160), (d) (Ma_C, Ma_T, Ra_C) = (1428, 3500, 160).

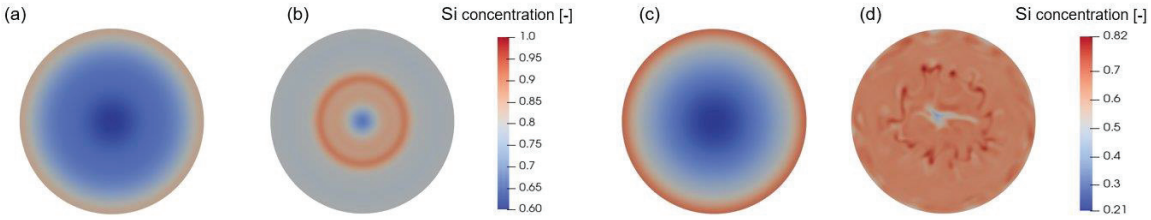

Figure 5.2 Snapshots of computed Si concentration distribution for S = 1.1 in the r-θ plane at z = 2.5 mm: (a) (Ma_{C}, Ma_{T}, Ra_{T}) = (0, 0, 239), (b) (Ma_{C}, Ma_{T}, Ra_{T}) = (714, 1750, 239), (c) (Ma_{C}, Ma_{T}, Ra_{T}) = (0, 0, 477.9), (d) (Ma_{C}, Ma_{T}, Ra_{T}) = (1428, 3500, 477.9).

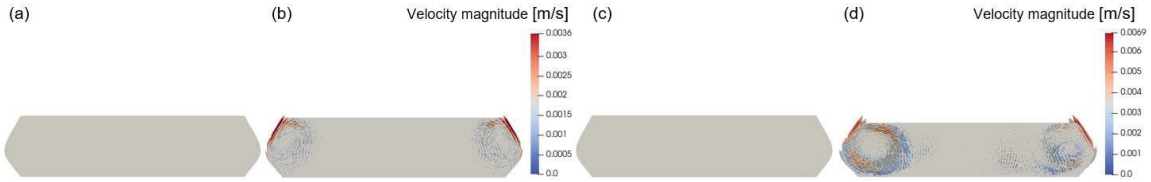

Figure 5.3 Snapshots of flow velocity magnitude at S = 1.1 in the r-z plane: (a) (Ma_{C}, Ma_{T}, Ra_{C}) = (0, 0, 80), (b) (Ma_{C}, Ma_{T}, Ra_{C}) = (714, 1750, 80), (c) (Ma_{C}, Ma_{T}, Ra_{C}) = (0, 0, 160), (d) (Ma_{C}, Ma_{T}, Ra_{C}) = (1428, 3500, 160).

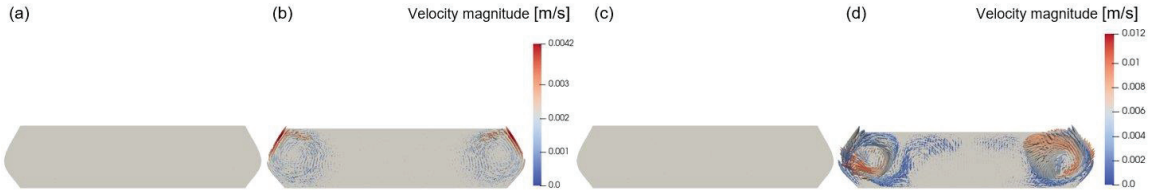

Figure 5.4 Snapshots of flow velocity magnitude at S = 1.1 in the r-z plane: (a) (Ma_{C}, Ma_{T}, Ra_{T}) = (0, 0, 239), (b) (Ma_{C}, Ma_{T}, Ra_{T}) = (714, 1750, 239), (c) (Ma_{C}, Ma_{T}, Ra_{T}) = (0, 0, 477.9), (d) (Ma_{C}, Ma_{T}, Ra_{T}) = (1428, 3500, 477.9).

5.2 Flow regimes under various volume ratios

The computed flow regimes are summarized in Figure 5.5 (a-c) with respect to volume ratios at different thermal and solutal Marangoni numbers. The flow patterns in these

diagrams are identified by the time variation of concentration and temperature values in the r-θ plane at the z = 2.5 mm under 1-g. In the figures, we present specific thermal Marangoni numbers (presented along the horizontal axis) by varying the solutal Marangoni numbers (presented along the vertical axis). Generally, for increasing Ma_{C} values at a low and middle range of Ma_{T} values, the flow patterns constantly change from steady to oscillatory and then to quasi-periodic in all volume ratios. At high Ma_{T} values, random-periodic flow patterns appear only at the high-volume ratio (S = 1.1). The critical stability region is a decreasing function of the volume ratio. Within this range, it reaches a maximum at S = 0.9 and a minimum at S = 1.1. Therefore, one can conclude that the effect of the volume ratio is significant.

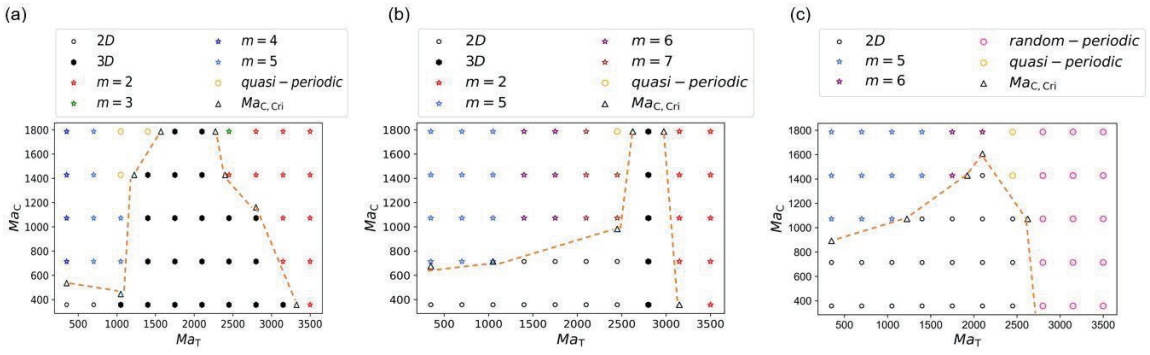

Figure 5.5 Stability curves of the base flow in (Ma_{T}, Ma_{C}) (dash lines) under (1-g) (a) S = 0.9 (b) S = 1 (c) S = 1.1.

5.3 Steady flow pattern

When the Marangoni number is relatively small, the thermal-solutal Marangoni convection is steady, called the "steady flow" hereafter. Figure 5.5 (a-c) shows the 2D steady axisymmetric flow regime that is observed for all three volume ratios considered. At the higher volume ratio, the 2D steady axisymmetric flow region becomes larger, while the

region of 3D steady flow decreases as seen from Figure 5.5. When the Ma_C increases for a given Ma_T, the flow pattern transits from 2D steady axisymmetric or 3D steady to oscillatory depending on volume ratios ($S = 0.9$, $S = 1$ and $S = 1.1$). This primary 2D steady axisymmetric flow described above breaks the spatial axial symmetry of the basic solution. It replaces this solution of maximum symmetry with another steady flow with a different symmetry pattern. The numerical solution can be azimuthally shifted with respect to each other but remains the same; that is the feature of the final stationary supercritical state called "3D steady flow".

5.4 Critical Marangoni number

As mentioned above, at a particular Ma_T, the flow pattern transits from 2D steady axisymmetric or 3D steady to an oscillatory mode as Ma_C increases, the solutal Marangoni number exceeds a critical value, called "the critical solutal Marangoni number" ($Ma_{C,Cri}$), and the steady flow becomes unsteady and bifurcates into three-dimensional oscillatory flows called “primary bifurcation”. The $Ma_{C,Cri}$ values were obtained for each volume ratio by the global linear stability analysis method, which has shown high accuracy in our previous studies [88].

In the present study, for $S = 0.9$ (concave shape), the 2D steady axisymmetric flow becomes 3D oscillatory when Ma_C increases at a given Ma_T value for all Ma_T values for the range of $Ma_T < 1050$.

For the cases of $1050 \leq Ma_T < 3150$, the 3D steady flow becomes 3D oscillatory as the primary bifurcation. For all cases that $Ma_T > 3150$, the flow is of a 3D oscillatory pattern with increasing Ma_T at a fixed Ma_C. At $S = 0.9$, the critical wave numbers (m_{Cri}) are 2, 4 and 5 with increasing Ma_T as shown in Figure 5.5 (a).

For $S = 1$, in all cases with $Ma_C > 0$, the 2D steady axisymmetric flow becomes 3D oscillatory as the primary bifurcation with increasing Ma_C at a fixed Ma_T for $Ma_T < 2800$. For the cases for $Ma_T > 3150$, the flow pattern becomes 3D oscillatory with increasing Ma_T for a fixed

Ma_C. For S = 1, the m_{Cri} values are 2, 5, 6, and 7 with increasing Ma_T as shown in Figure 5.5 (b).

For S = 1.1 (convex shape), in all cases with $Ma_C > 0$, the 2D steady axisymmetric flow becomes 3D oscillatory as the primary bifurcation with increasing Ma_C at a fixed Ma_T for $Ma_T < 2800$. For the cases of $Ma_T > 2800$, the flow pattern is random-periodic with increasing Ma_T at a fixed Ma_C. For S = 1.1, the m_{Cri} values are 5 and 6 with increasing Ma_T for the range of thermal-solutal Marangoni numbers considered in the present study, as seen in Figure 5.5 (c).

Our simulation results, as also supported by previous analyses, could explain the stabilization and destabilization mechanisms mentioned earlier [96, 97]. For the Marangoni convection rolls, the degree of freedom is reduced for the case of S = 0.9. In this case, in fact, due to the concave shape of the free surface, Marangoni convection rolls prevent mutual interference and strengthen the constraints for the flow field, leading to large values of the critical Marangoni numbers. Thus, as seen from Figure 5.5 (a), the critical solutal Marangoni numbers tend to be higher in the case of S = 0.9. On the other hand, for the case of S = 1.1, the degree of freedom is enhanced for the Marangoni convection rolls due to the convex shape of the free surface. It becomes pervasive throughout the system, lowering the stability threshold as shown in Figure 5.5 (c).

However, another earlier research work [9] has pointed out that two different mechanisms are responsible for this inertial instability of Marangoni flow, and investigated the critical Reynolds numbers. The Reynolds number (*Re*), which represents the ratio of inertial forces to viscous forces, is a critical parameter influencing inertial instability. The maximum *Re* number in our research is 2682.4. Therefore, higher Reynolds numbers indicate stronger inertial effects (straining and/or centrifugal mechanisms) and an increased likelihood of instability.

The first contribution is the strain in the vortex center near the free surface. The second contribution is due to the centrifugal effect due to the shape of the liquid bridge. For a small volume ratio (S = 0.9), the enhanced strain on the Marangoni convection roll due to the concave shape leads to a high contribution of the strain-induced mechanism instability mechanism. On the other hand, for a high-volume ratio (S = 1.1), the convection roll becomes more circular, indicating less strain, and the centrifugal mechanism becomes more critical due to the convex shape.

Both mechanisms are present for the volume ratio (S = 1), leading to an optimum critical Marangoni number.

5.5 Effect of volume ratio under normal (1-g) gravity condition

The effect of gravity is due to three factors in the liquid bridge. The first factor is the hydrostatic pressure, which breaks the mirror symmetry of the free surface with respect to the mid vertical plane. The second factor is the buoyancy force in the bulk, which increases with the Grashof number ($Gr \neq 0$). The third factor is the way of heating the liquid bridge. In the present cases, the heating orientation is kept in the same direction while a higher temperature is adopted at the bottom horizontal boundary and a lower temperature is imposed on the upper boundary of the liquid bridge, as shown in Figure 2.2.2.

At Ma_{C} = 714, Ma_{T} = 1400 and Ra_{T} = 191, the snapshot of the computed concentration field shown in Figure 5.6 (a) exhibits a 3D steady flow pattern for S = 0.9, and a 2D steady axisymmetric structure observed in Figure 5.6 (b) and (c) corresponding to the cases of S = 1, and S = 1.1. Moreover, comparing concentration flow patterns in both the r-θ plane and the r-z plane, the concentration distribution is more uniform for the cases of S = 1 and S = 1.1 for low Marangoni and thermal Rayleigh numbers as shown in the snapshots of Figure 5.6 (b-c).

Figure 5.7 (a-c) shows snapshots of flow velocity magnitude at Ma_{C} = 714, Ma_{T} = 1400 and Ra_{T} = 191. For all three volume ratios, there are two Marangoni convection rolls near the

free surface, and the flow along the free surface is from bottom to top. The shapes of Marangoni convection rolls are significantly different in each case of volume ratios.

For S = 1.1 (convex shape), the Marangoni convection roll becomes more circular, indicating less strain as shown in the snapshot of Figure 5.7 (c). However, the Marangoni flow stretched to the central region and towards the cold wall at the small volume ratio in the half-zone liquid bridge as shown in the snapshot of Figure 5.7 (a).

Furthermore, the steady Marangoni convection roll becomes more stretched at the small volume ratio, but it becomes more circular at the high-volume ratio. Both effects are present for Marangoni convection rolls in the case of S = 1 as shown in the snapshot of Figure 5.7 (b).

When the solutal Marangoni number exceeds the critical value $Ma_{\mathrm{C,Cri}}$, the thermal-solutal Marangoni flow bifurcates into the unsteady flow. When Ma_{C} = 1428, Ma_{T} = 2450 and Ra_{T} = 334.5, the snapshots of concentration field is shown in Figure 5.8 (a-c). In the cases of S = 0.9 and S = 1, it exhibits an oscillatory pattern with different azimuthal wave numbers, where the lower wave number (m = 2) is for S = 0.9 and the higher value found (m = 7) is for the volume ratio of S = 1 as shown in the snapshots of Figure 5.8 (a-b). The snapshot of Figure 5.8 (c) shows the case of S = 1.1, where the pattern behaves quasi-periodic, which corresponds to the appearance of the rotating traveling wave in the concentration field in the azimuthal direction. At the high-volume ratio (S = 1.1), the wave number disappeared, and there was a transition to quasi-periodic (Figure 5.8 (c)). This shows that the instability of thermal-solutal Marangoni convection is enhanced at the higher volume ratio.

Figure 5.9 (a-c) show snapshots of flow velocity magnitude, representing an unsteady flow at Ma_{C} = 1428, Ma_{T} = 2450 and Ra_{T} = 334.5 for different volume ratios. For the thermal-solutal Marangoni forces being in the same direction, at S = 0.9, the Marangoni convection roll center is shifted radially inward and displaced toward the cold wall as shown in the snapshot of Figure 5.9 (a). The enhanced strain on the Marangoni convection roll due to the

geometrical constraints (i.e., free surface being concave) leads to the convection roll's flow to the middle region than that of the convex shape as shown in the snapshots of the Figure 5.9 (a) and Figure 5.9 (c).

At the higher volume ratio, the Marangoni convection roll becomes more circular, indicating less strain. The Marangoni convection roll center is shifted radially outward and towards the mid-plane for the convex free surface. The centrifugal effect and the roll's mobility area become high due to the high-volume ratio; therefore, increased local driving force promotes the circular Marangoni convection roll as shown in the snapshot of the Figure 5.9 (c).

The snapshot of Figure 5.9 (b) shows that (at $S = 1$), both conditions are present and lead to the optimum condition for the Marangoni convection rolls. However, the snapshots of Figure 5.9 (a-c) show if the Ma_{T} and Ma_{C} numbers are sufficiently large, the total thermal-solutal Marangoni convection becomes stronger, and circulation extends with a high-velocity to the liquid bridge's central region at all three volume ratios compared with the snapshots of Figure 5.7 (a-c).

The time dependency of concentration at the sampling point (8.8 mm, 0 rad, 2.5 mm) for all volume ratios is shown in Figure 5.10. As seen in Figure 5.10 for $S = 0.9$ and $S = 1$, the concentration pattern exhibits periodic fluctuations, and the time period of concentration fluctuation decreases with time. This means that it oscillates with higher frequencies. On the other hand, the concentration fluctuation in the case of a high-volume ratio ($S = 1.1$) exhibits almost a quasi-periodic pattern over time. We can state that the concentration fluctuations will become more complex and will exhibit violent fluctuations at the high-volume ratio ($S = 1.1$) compared to those of the low-volume ratio. This illustrates that the increase in the volume ratio can destabilize flow structures and lead to more complex transport structures in the melt.

3D random-periodic flows with time-dependent irregular azimuthal wave develops at high Ma_{T} only for $S = 1.1$ (Figure 5.5 (c)). These random-periodic flows tend to rotate when

Ma_T > 2800 at all Ma_C values. The computed random-periodic concentration pattern and the fluid flow velocity magnitude for S = 1.1 are shown in Figure 5.11 (a-c). The strong nonuniformity in concentration distribution is obvious at this high-volume ratio. The random-periodic flow behavior represents a qualitative enlargement in the free surface area (convex shape).

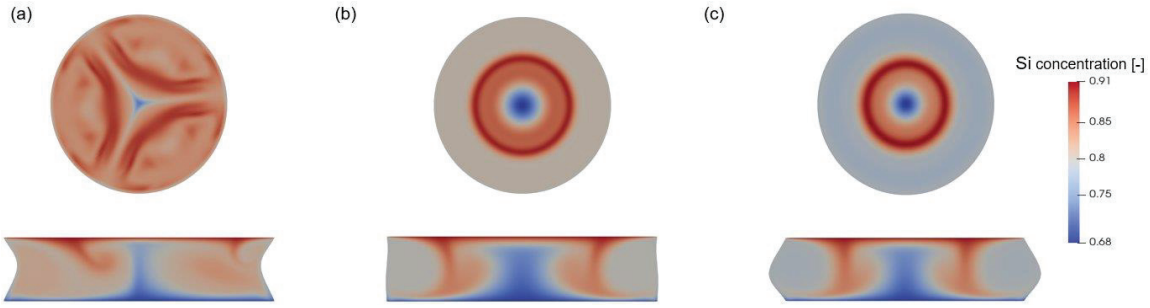

Figure 5.6 Snapshots of computed Si concentration distribution at (Ma_C, Ma_T, Ra_T) = (714, 1400, 191) in the *r*-θ plane at z = 2.5 mm and the vertical *r*-*z* plane at: (a) S = 0.9, (b) S = 1 and (c) S =1.1.

Figure 5.7 Snapshots of flow velocity magnitude at (Ma_C, Ma_T, Ra_T) = (714, 1400, 191) in the vertical *r*-*z* plane at: (a) S = 0.9, (b) S = 1 and (c) S =1.1.

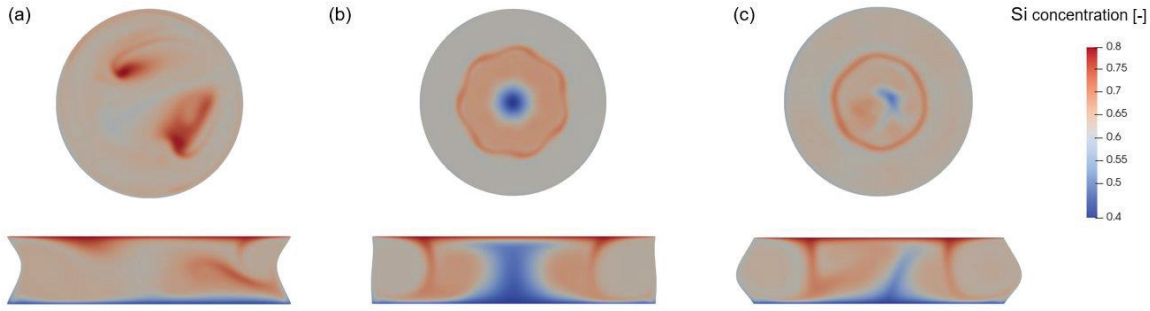

Figure 5.8 Snapshots of computed Si concentration distribution at (Ma_C, Ma_T, Ra_T) = (1428, 2450, 334.5) in the *r*-θ plane at z = 2.5 mm and the vertical *r*-*z* plane at: (a) S = 0.9, (b) S = 1 and (c) S = 1.1.

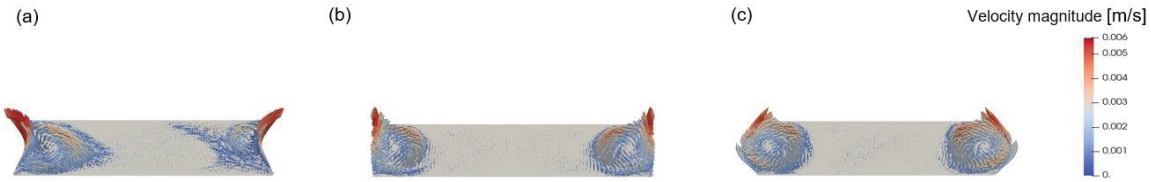

Figure 5.9 Snapshots of flow velocity magnitude at (Ma_C, Ma_T, Ra_T) = (1428, 2450, 334.5) in the vertical *r*-*z* plane at: (a) S = 0.9, (b) S = 1 and (c) S = 1.1.

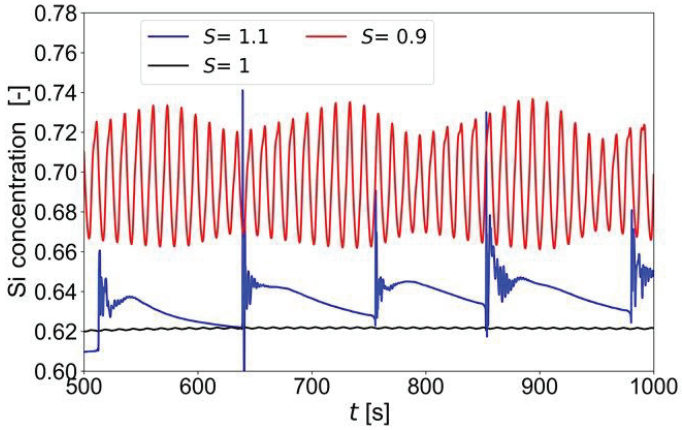

Figure 5.10 Si concentration distribution at (Ma_C, Ma_T, Ra_T) = (1428, 2450, 334.5) for three volume ratios (S) at the sampling point (8.8 mm, 0 rad, 2.5 mm).

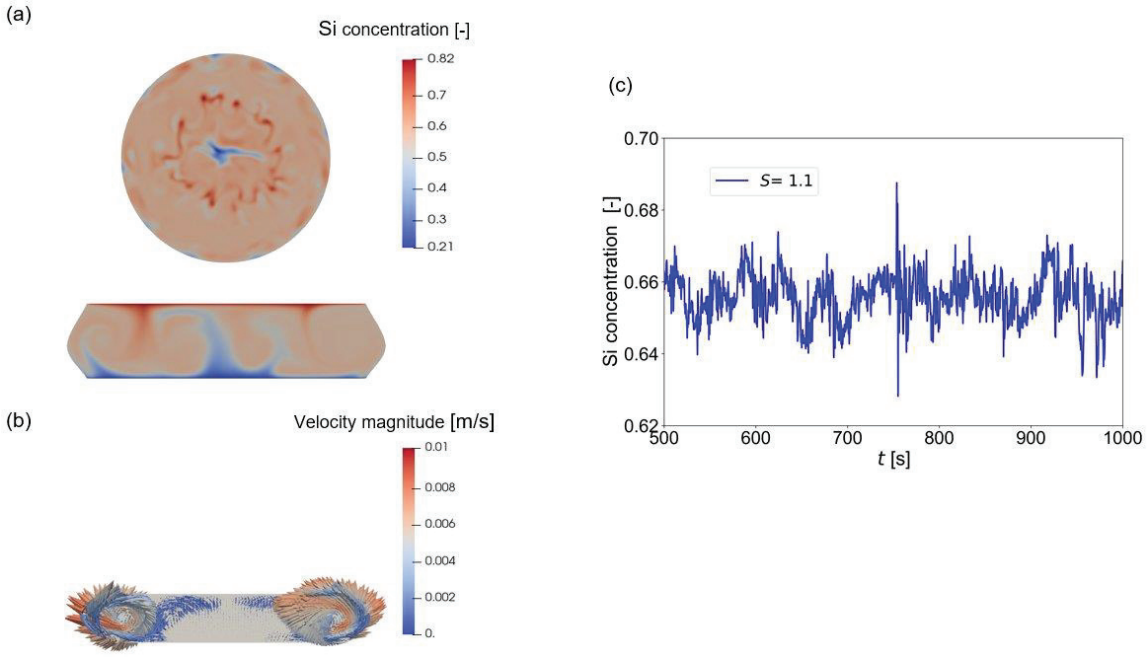

Figure 5.11 (a) Snapshots of computed Si concentration distribution for S = 1.1 in the r-θ plane at z = 2.5 mm and the vertical r-z plane (b) Flow velocity magnitude in the vertical r-z plane (c) Si concentration distribution at sampling point (8.8 mm, 0 rad, 2.5 mm) for (Ma_C, Ma_T, Ra_T) = (1428, 3500, 477.9).

5.6 Effect of volume ratio under zero (0-g) gravity condition

Under the zero-gravity condition, the free surface deformation is symmetric with respect to the middle axis. The top and bottom contact angles are equal, and the volume ratio becomes higher as the contact angle increases. The computed snapshots of concentration distribution are shown in Figure 5.12 and Figure 5.13.

When we compare the concentration patterns under steady conditions for S = 1.1 at Ma_C = 714, Ma_T = 1750 under normal gravity (Ra_T = 239) and zero gravity conditions (Ra = 0), we observe the same patterns (2D steady axisymmetric) as seen in Figure 5.12 (a-b). The snapshots of Figure 5.12 (c-d) show concentration distribution for the case of S = 1.1 under the unsteady condition at the Ma_C = 1428, Ma_T = 1750 under normal (Ra_T = 239) and zero

gravity (Ra = 0). The concentration patterns exhibit oscillatory behavior with the same azimuthal wave number (m = 6).

The snapshots of Figure 5.13 (a-b) for S = 1 at Ma_{C} = 357, Ma_{T} = 1050 under normal (Ra_{T} = 143.37) and zero gravity (Ra_{T} = 0) conditions show a steady case. We observe the concentration patterns of 2D steady axisymmetric behavior and unsteady at Ma_{C} = 1428, Ma_{T} = 1050 under normal (Ra_{T} = 143.37) and zero gravity (Ra_{T} = 0) conditions with oscillatory behavior with the same azimuthal wave number (m = 5) as shown in the snapshots of Figure 5.13 (c-d).

The gravity is in the opposite direction of the Marangoni forces. Hence, for small thermal Rayleigh numbers, the thermal-solutal Marangoni forces under 1g are dominant for both volume ratios S = 1.1 and S = 1. Under this condition, the associated concentration distribution structure remains the same under 1-g and 0-g conditions.

Figure 2 in [40], which shows the stability curve of the axisymmetric base flow on thermal-solutal Marangoni convection driven by the forces in the same direction for S = 1 under 0-g. Comparing Figure 2 of [40] and Figure 5.5 (b) of the present work shows that the onset of thermal-solutal Marangoni convection is approximately the same under 0-g and 1-g conditions for the case of S = 1. Since the curves in these two figures do not differ much, we conclude that the major factor determining the change in stability is the volume ratio under both 1-g and 0-g conditions.

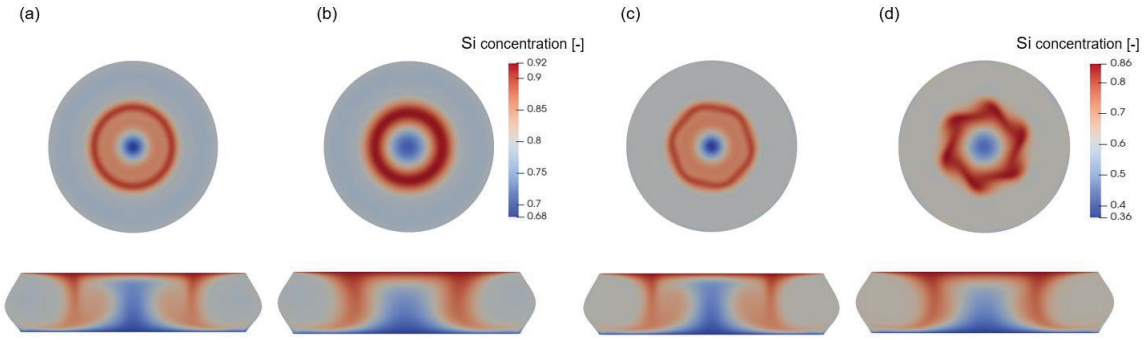

Figure 5.12 Snapshots of computed Si concentration distribution for S = 1.1 in the r-θ plane at z = 2.5 mm and the vertical r-z plane: (a) (Ma_{C}, Ma_{T}, Ra_{T}) = (714, 1750, 239), (b) (Ma_{C}, Ma_{T}, Ra_{T}) = (714, 1750, 0), (c) (Ma_{C}, Ma_{T}, Ra_{T})= (1428, 1750, 239), (d) (Ma_{C}, Ma_{T}, Ra_{T})= (1428, 1750, 0).

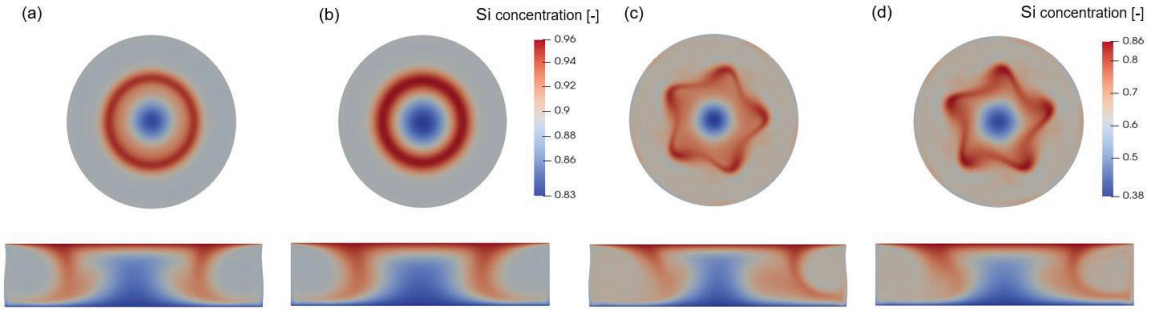

Figure 5.13 Snapshots of computed Si concentration distribution for S = 1 in the r-θ plane at z = 2.5 mm and the vertical r-z plane: (a) (Ma_{C}, Ma_{T}, Ra_{T}) = (357, 1050, 143.37), (b) (Ma_{C}, Ma_{T}, Ra_{T}) = (357, 1050, 0), (c) (Ma_{C}, Ma_{T}, Ra_{T}) = (1428, 1050, 143.37), (d) (Ma_{C}, Ma_{T}, Ra_{T}) = (1428, 1050, 0).

5.7 Effect of solutal Marangoni convection at S = 1.1

The solutal Marangoni convection is considered for S = 1.1 at Ma_{T} = 1750 and Ra_{T} = 239 as shown in the snapshots of Figure 5.14. The snapshots of Figure 5.14 (a-b) show that the concentration patterns are 2D steady axisymmetric when Ma_{C} is small (Ma_{C} = 0 and Ma_{C} = 714). The concentration patterns become oscillatory with an azimuthal wave number (m = 6) at the higher values of Ma_{C}as shown in the snapshot of Figure 5.14 (c). At small

Ma_{T} values, the temperature field is almost steady with an axisymmetric structure due to the very low Pr number of the melt [78]. At higher Ma_{T} value, both thermal and solutal Marangoni flows become notable, and the regime becomes more complex, which is highly dependent on the Marangoni ratio ($Ma_{\mathrm{C}}/Ma_{\mathrm{T}}$) and the quantitative relationship between Ma_{C} and Ma_{T}.

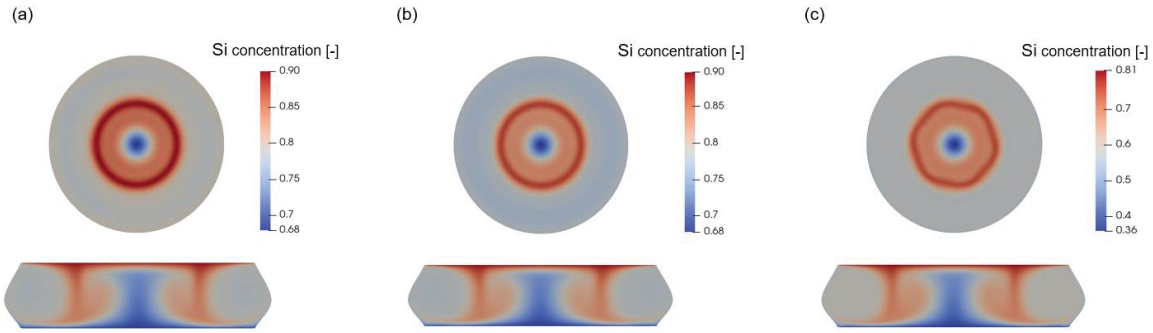

Figure 5.14 Snapshots of computed Si concentration distribution for S = 1.1 at (Ma_{T}, Ra_{T}) = (1750, 239) in the r-θ plane at z = 2.5 mm and the vertical r-z plane: (a) Ma_{C} = 0, (b) Ma_{C} = 714 and (c) Ma_{C} = 1428.

CHAPTER 6

CONCLUISIONS AND FUTURE PERSPECTIVES

6.1 Study of the effect of liquid depth on the stability of thermal Marangoni convection in a shallow cavity

A series of three-dimensional numerical simulations were conducted to investigate the effect of liquid depth on the thermal Marangoni convection instability of silicone oil in shallow rectangular cavities subject to perpendicular temperature gradients.

(1) When the thermal Marangoni number is small, the basic flow is steady. Uniform flow patterns develop at relatively large range of thermal Marangoni numbers for the thinner film (0.041), while the critical thermal Marangoni numbers are large compared with those of the thicker film (0.082). Therefore, thinner films are suitable for enhancing the appearance of polishing applications.

(2) When the thermal Marangoni number exceeds a critical value for the thicker film (0.082), an oscillatory flow appears first, and then it becomes chaotic. The critical thermal Marangoni numbers are relatively low, and the flow quickly destabilizes for thicker films compared with for thinner films.

(3) The chaotic flow behavior has a significant impact on spreading and mixing properties; therefore, thicker films are suitable for lubrication and mixing applications.

6.2 Study of the effect of deformed free surface on the thermo-solutal Marangoni convection in a shallow cavity

The present numerical study carried out for a shallow cavity has the following key findings.

(1) In the relatively low *Pr* number fluids, the effect of volume ratio on temperature distribution is insignificant under steady conditions. Once Marangoni convection becomes unsteady, the effect of volume ratio becomes significant for the temperature field. The volume ratio affects the flow velocity distribution under both steady and unsteady conditions. Furthermore, under steady Marangoni conditions, particularly compared with unsteady Marangoni conditions, maintaining an appropriate volume ratio is highly favorable for achieving uniform temperature and flow velocity distributions.

(2) For a high *Sc* - low *Pr* number fluid, the effect of volume ratio on concentration distribution is more significant than temperature distribution in a low *Pr* number fluid under the steady Marangoni condition. This shows that the volume ratio plays a key role in both concentration and velocity distributions in the steady Marangoni condition. At the high-volume ratios ($S = 1$, $S = 1.2$) we observe more regular and periodic concentration and flow velocity patterns than those at the low volume ratio ($S = 0.8$) under unsteady Marangoni conditions.

(3) For a high *Pr* number fluid, the effect of volume ratio on the temperature field is higher than that of a low *Pr* fluid under the steady thermal Marangoni condition. It is seen that the temperature and flow velocity distributions in the high *Pr* fluid

are highly depended on the volume ratio under the steady and unsteady Marangoni convections.

(4) For a high *Sc* and *Pr* number fluid, the effect of volume ratio on temperature, concentration, and flow velocity distributions under the steady Marangoni condition is significant. Under steady conditions, we observe uniform concentration and flow velocity distributions in fluids with low *Pr* and high *Sc* numbers and high *Pr* and high *Sc* numbers on the flat free surface. Under the unsteady Marangoni condition for a high *Pr* and high *Sc* number fluid, regular concentration and flow velocity fluctuations were observed at high volume ratios ($S = 1$ and $S = 1.2$) compared with those in the case of $S = 0.8$. When comparing the flow structures of a high *Sc* and high *Pr* number fluid with those of a high *Sc* and low *Pr* number fluid under the unsteady Marangoni condition, we see that the *Pr* number is a significant factor affecting the flow structures. Higher *Pr* number gives rise to uniform concentration and flow velocity fluctuations in the fluid.

One can conclude that the volume ratio of a shallow cavity is a critical parameter influencing temperature, concentration, and flow velocity distributions. The present study also highlights the role of fluid properties and Marangoni conditions influencing flow characteristics, which are essential for optimizing various industrial processes such as material welding, glass production, painting, and crystal growth. The study has focused on fluids of low and high Prandtl and specific Schmidt numbers, exploring their significance on process outcomes. Furthermore, it is hoped that the present study would provide valuable insights into the design and production of higher-quality industrial products. Such a focused approach would also allow for targeted improvements in production processes, ensuring both efficiency and quality enhancement in industrial settings.

6.3 The effects of zone volume and gravity on thermo-solutal Marangoni convection instability in a half-zone model of float-zone growth of SiGe

The present study examines numerically the effects of volume ratio and gravity on the onset and characteristics of thermo-solutal Marangoni convection in the molten zone of FZ of SiGe ($Pr = 6.37\times10^{-3}$ and $Sc = 14$) by using a half-zone model. The critical conditions of the thermal-solutal Marangoni convection under 1-g and 0-g are determined.

(1) The stability curve of the thermal-solutal Marangoni convection is calculated at 1-g. Its relative magnitude explains the dependence of the critical solutal Marangoni numbers on the shape of the liquid bridge. Compared to the threshold of the primary bifurcation, the volume ratio is a sensitive parameter for the thermal-solutal Marangoni instability since it influences the critical solutal Marangoni numbers and the critical wave number. The critical solutal Marangoni region takes a minimum at $S = 1.1$. The numerical results have shown that for a constant aspect ratio, the critical azimuthal wave number can be shifted to a higher value at $S = 1.1$ (convex shape) or to lower values at $S = 0.9$ (concave shape). The behavior has been explained considering the basic vortex, and hence, its stability is mainly determined by the hydrostatic free surface deformation and the hydrostatic pressure. Due to qualitative enlargement in the free surface area, the random-periodic pattern has been studied only for the $S = 1.1$.

(2) The effect of gravity on the critical condition is mainly driven by hydrostatic deformation and thermal-solutal Marangoni convection. The results show that the $S = 1$ stability region and m are approximately the same under normal and zero gravity conditions. Therefore, gravity has a lesser impact on the threshold of the Marangoni convection. However, in zero gravity, the free surface shape remains symmetric with respect to the mid-plane.

(3) The effect of pure natural convection on flow structure is less important. The results show that buoyancy has a marginal influence (at S = 1.1) on flow patterns compared to that of the Marangoni convection. For the small dynamic Bond number, Marangoni forces are dominant. As a result, the flow pattern shifts to a random-periodic mode at the high Ma_{C} and Ma_{T} values.

(4) The predicted flow transition mechanism depends on hydrostatic deformation and thermal-solutal Marangoni values. The effect of Marangoni flows is highly dependent on the Marangoni ratio and the quantitative relationship between Ma_{C} and Ma_{T} in each volume ratio. The flow develops into various regimes depending on the values of Ma_{C} and Ma_{T}. The predicted flow transition mechanism depends on Ma_{C}. When Ma_{C} increases, the transition occurs, and 2D steady axisymmetric flow becomes oscillatory, then quasi-periodic in the lower and middle range of Ma_{T} values for all three volume ratios. For S = 0.9 and S = 1 when increasing Ma_{C} at high Ma_{T} values, flow patterns show oscillatory behavior. We observe only random-periodic structure at S = 1.1.

6.4 Future perspectives

This thesis numerically demonstrated the instabilities of Marangoni convection in a shallow rectangular cavity and half-zone model with various geometrical conditions under microgravity and normal gravity. However, several aspects warrant further study due to limited time and the significant computational workload.

(1) The present work considers the cavity and half-zone model with a deformed surface. In thin film process, top and bottom surface deformation in a shallow cavity is also important. For two deformed surfaces applied together with

Marangoni convection, the flow behavior becomes more complex than that of one deformed surface in zero-gravity conditions. It is important to study flow instabilities under zero-gravity conditions by considering the shallow cavity's top and bottom surface deformation.

(2) In the future, it is also essential to investigate the onset of the Marangoni convection in the deformed free surface of the full-zone liquid bridge under zero-gravity and normal-gravity conditions.

(3) Numerical results in a half-floating zone with a deformed free surface indicate the presence of unsteady flow patterns, manifesting in either quasi-periodic or random-periodic modes. These patterns can adversely affect the uniformity of the growing crystal. Therefore, applying external conditions, such as rotating the top or bottom plane in a deformed free surface with the full-zone model, is anticipated to control or suppress these unsteady flow patterns.

REFERENCES

[1] X. Chen and X. Wang and P. G. Chen and Q. Liu "Thermal effects of substrate on Marangoni flow in droplet evaporation: response surface and sensitivity analysis", *Int. J. Heat Mass Transfer*, **113**:354–365, 2017.

[2] D. C. Venerus and D. N. Simavilla "Tears of wine: New insights on an old phenomenon", *Sci. Rep*., **5**(1):1–10, 2015.

[3] J. Park and J. Ryu and H. J. Sung and H. Kim "Control of Solutal Marangoni-driven Vortical Flows and Enhancement of Mixing Efficiency", *J. Colloid Interface Sci.,***561**:408-415, 2020.

[4] A. Chengara and A. Nikolov and D. Wasan "Surface Tension Gradient Driven Spreading of Tri siloxane surfactant Solution on Hydrophobic Solid", *Colloids Surf, A Physicochem Eng Asp.*", **206**:31-39, 2002.

[5] D. Camel and P. Tison and J. P Garandet "Experimental study of Marangoni flows in molten and solidifying Sn and Sn-Bi layers heated from the side", *Eur*. *Phys. J. Appl. Phys*., **18**(3):201–219, 2002.

[6] Y. Y. Teng and J. C. Chen and C. W. Lu and C. Y Chen, "The carbon distribution in multicrystalline silicon ingots grown using the directional solidification process", J. *Cryst. Growth*, **312**(8):1282–1290, 2010.

[7] Q. Kang and D. Wu and L. Duan and J. He and L. Hu and L. Duan and W. Hu, "Surface configurations and wave patterns of thermocapillary convection onboard the SJ10 satellite", *Phys. Fluids*, **31**:1-20, 2019.

[8] Y. R. Li and L. Peng and Y. Akiyama and N. Imaishi, "Three-Dimensional Numerical Simulation of Thermocapillary Flow of Moderate Prandtl Number Fluid in an Annular Pool", *J. Cryst. Growth*, **259**:374-387, 2003.

[9] C. Nienhüser and H. C. Kuhlmann, "Stability of thermocapillary flows in non-cylindrical liquid bridges", *J. Fluid Mech*., **458**:35-73, 2002.

[10] J. C. Chen and J. C. Sheu and S. S. Jwu, "Numerical computation of thermocapillary convection in a rectangular cavity", *Numer. Heat Transf.; A: Appl.*, **17**:287-308, 1990.

[11] M. Tsai and S. Kou, "Marangoni convection in weld pools with a free surface," *Int. J. Num. Methods Fluids* **9**, 1503–1516 (1989).

[12] Marcello Lappa. “CHAPTER 1- Space research”. *In. Fluids, Materials and Microgravity*. Ed. by Marcello Lappa. Oxford: Elsevier, 2004, pp. 1–37.

[13] M. K. Smith and S. H. Davis, “Instabilities of dynamic thermocapillary liquid layers. Part 1. convective instabilities”, *J. Fluid Mech*., **132**:119–144, 1983.

[14] Y. R. Li and L. Peng and Y. Akiyama and N. Imaishi, “Three-dimensional numerical simulation of thermocapillary flow of moderate Prandtl number fluid in an annular pool”, *J. Cryst. Growth*, **259**(4):374–387, 2003.

[15] Y. R. Li and L. Peng and S. Y. Wu and D. L. Zeng and N. Imaishi, “Thermocapillary convection in a differentially heated annular pool for moderate Prandtl number fluid”, *Int. J. Therm. Sci*., **43**(6):587–593, 2004.

[16] T. Azami and S. Nakamura and M. Eguchi and T. Hibiya, “The role of surface-tension-driven flow in the formation of a surface pattern on a czochralski silicon melt”, *J. Cryst. Growth*, **233**(1-2):99–107, 2001.

[17] D. Schwabe, “Buoyant-thermocapillary and pure thermocapillary convective instabilities in czochralski systems”, *J. Cryst. Growth*, **237**:1849–1853, 2002.

[18] M. A. Pelacho and J. Burguete, “Temperature oscillations of hydrothermal waves in thermocapillary-buoyancy convection”, *Phys. Rev. E*, **59**(1):835, 1999.

[19] J. Burguete and N. Mukolobwiez and F. Daviaud and N. Garnier and A. Chiffaudel, “Buoyant-thermocapillary instabilities in extended liquid layers subjected to a horizontal temperature gradient”, *Phys. Fluids*, **13**(10):2773–2787, 2001.

[20] D. Schwabe and A. Zebib and B. C Sim, “Oscillatory thermocapillary convection in open cylindrical annuli. Part 1. experiments under microgravity”, *J. Fluid Mech.,* **491**:239, 2003.

[21] B. C Sim and A. Zebib and D. Schwabe, “Oscillatory thermocapillary convection in open cylindrical annuli. Part 2. Simulations”, *J. Fluid Mech*., **491**:259, 2003.

[22] H. Liu and Z. Zeng and L. Yin and Z. Qiu and L. Qiao, “Influence of aspect ratio on the onset of thermocapillary flow instability in annular pool heated from inner wall”, *Int. J. Heat Mass Transfer*, **129**:746–752, 2019.

[23] L. Zhang and Y. R Li and C. M. Wu, “Effect of surface heat dissipation on thermocapillary convection of low Prandtl number fluid in a shallow annular pool”, *Int. J. Heat Mass Transfer*, **110**:460–466, 2017.

[24] H. Liu and Z. Zeng and L. Yin and Z. Qiu and L. Zhang, "Effect of the Prandtl number on the instabilities of the thermocapillary flow in an annular pool", *Phys. Fluids,* **31**(3):034103, 2019.

[25] N. Imaishi, S. Yasuhiro and Y. Akiyama and S. Yoda, "Numerical simulation of oscillatory Marangoni flow in half-zone liquid bridge of low Prandtl number fluid," *J. Cryst. Growth,* **230**:164–171, 2001.

[26] K. Li and N. Imaishi and C. Jing and S. Yoda, "Proper orthogonal decomposition of oscillatory Marangoni flow in half-zone liquid bridges of low-Pr fluids," *J. Cryst. Growth,* **307**:155-170, 2007.

[27] K. Li and B. Xun and N. Imaishi and S. Yoda and W. Hu, "Thermocapillary flows in liquid bridges of molten tin with small aspect ratios," *Int. J. Heat Fluid Flow*, **29**:1190–1196, 2008.

[28] T. L Bergman, "Numerical simulation of double-diffusive Marangoni convection", *Phys. Fluids*, **29**(7):2103–2108, 1986.

[29] K. Arafune and A. Hirata, "Thermal and solutal Marangoni convection in In–Ga–Sb system", *J. Cryst. Growth*, **197**(4):811–817, 1999.

[30] K. Arafune and A, "Hirata. Interactive solutal and thermal Marangoni convection in a rectangular open boat", *Numer. Heat Transfer*, Part A, **34**(4):421–429, 1998.

[31] K. Arafune and K. Yamamoto and A. Hirata, "Interactive thermal and solutal Marangoni convection during compound semiconductor growth in a rectangular open boat. Int. J. Heat Mass Transfer, **44**(13):2405–2411, 2001.

[32] Y. Okano and S. Umemura and Y. Enomoto and Y. Hayakawa and M. Kumagawa and A. Hirata and S Dost, "Numerical study of Marangoni convection effect on the melting of Gasb/Insb/Gasb", *J. Cryst. Growth*, **235**(1-4):135–139, 2002.

[33] Y. Okano and T. Suzumura and S. Sakai and Y. Hayakawa and M. Kumagawa and A. Hirata and S. Dost, "Oscillatory behaviour in melting of a Gasb/Insb/Gasb system", *Mech. Res. Commun*., **31**(5):605–610, 2004.

[34] M. A. Sheremet and I Pop, "Marangoni natural convection in a cubical cavity filled with a nanofluid", *J. Therm. Anal. Calorim*., **135**(1):357–369, 2019.

[35] Z. W. Chen and Y. S. Li and J. M. Zhan, "Double-diffusive Marangoni convection in a rectangular cavity: Onset of convection", *Phys. Fluids*, **22**(3):034106, 2010.

[36] J. M. Zhan and Z. W. Chen and Y. S. Li and Y. H. Nie, “Three-dimensional double-diffusive Marangoni convection in a cubic cavity with horizontal temperature and concentration gradients”, *Phys. Rev. E*, **82**(6):066305, 2010.

[37] J. J. Yu and C. M. Wu and Y. R. Li and J. C. Chen, “Thermal-solutal capillary-buoyancy flow of a low Prandtl number binary mixture with a-1 capillary ratio in an annular pool”, *Phys. Fluids*, **28**(8):084102, 2016.

[38] J. J. Yu and Y. R. Li and J. C. Chen and Y. Zhang and C. M Wu, “Thermal-solutal capillary-buoyancy flow of a low Prandtl number binary mixture with various capillary ratios in an annular pool”, *Int. J. Heat Mass Transfer*, **113**:40–52, 2017.

[39] R. L. Agampodi Mendis and A. Sekimoto and Y. Okano and H. Minakuchi and S. Dost, “The relative contribution of solutal Marangoni convection to thermal Marangoni flow instabilities in a liquid bridge of smaller aspect ratios under zero gravity”, *Crystals*, **11**(2):116, 2021.

[40] R. L. A. Mendis and A. Sekimoto and Y. Okano and H. Minakuchi and S. Dost, “Global linear stability analysis of thermo-solutal Marangoni convection in a liquid bridge under zero gravity,” *Microgravity Sci. Technol*. **32**:729–735 (2020).

[41] R. L. A. Mendis and A. Sekimoto and Y. Okano and H. Minakuchi and S. Dost, “A numerical study on the exact onset of flow instabilities in thermo-solutal Marangoni convection driven by opposing forces in a half-zone liquid bridge under zero gravity,” *J. Chem. Eng. Japan*, **54**:424–430 (2021).

[42] H. Minakuchi and Y. Takagi and Y. Okano and S. Gima and S. Dost, “The relative contributions of thermo-solutal Marangoni convections on flow patterns in a liquid bridge,” *J. Cryst. Growth*, **385**:61–65 (2014).

[43] H. Minakuchi and Y. Okano and S. Dost, “Effect of thermo-solutal Marangoni convection on the azimuthal wave number in a liquid bridge,” *J. Cryst. Growth*, **468**: 502–505 (2017).

[44] H. Minakuchi and Y. Okano and S. Dost, “The hysteresis phenomena of flow patterns due to thermal and solutal Marangoni convections in a liquid bridge under zero gravity,” *Fluid Mech. Res. Int.*, **2**:00018 (2018).

[45] Z. M. Tang and K. Li and W. R. Hu, “Influence of free surface curvature of a liquid layer on the critical Marangoni convection”, *Int. J. Heat Mass Transf.*, **51**: 5102- 5107, 2008.

[46] P. Luzzatto-Fegiz and K.R. Helfrich, “Laboratory experiments and simulations for solitary internal waves with trapped cores”, *J. Fluid Mech.,* **757**:354–380, 2014.

[47] R. Seemann and J. B. Fleury and C.C. Maass, “Self-propelled droplets”, *Eur. Phys. J.*, **225**:2227–2240, 2016.

[48] Q. Yang and Y. Liu and X. Jia and T. Zhang, “Numerical study of the thermocapillary instability in a thin liquid-air film”, *Phys. Fluids*, **34**:1–17, 2022.

[49] Weerakoon Rathnayake, Neranjan Nayanajith and Y. Okano and H. Minakuchi and S. Dost, “The Effects of Zone Volume and Gravity on Thermo-Solutal Marangoni Convection Instability in a Half-Zone Model of Float-Zone Growth of SiGe”, *J. Chem. Eng. Japan*, **57**:2364780, 2024.

[50] J. N. Koster, “Early Mission Report on the Four ESA Facilities: Biorack; Bubble, Drop and Particle Unit; Critical Point Facility and Advanced Protein Crystallization Facility Flown on the IML-2 Spacelab Mission”, *Microgravity News From ESA Report*, **7**:2-7, 1994.

[51] J. Xu and A. Zebib, “Oscillatory two- and three-dimensional thermocapillary convection”, *Phys. Fluids*, **364**:187–209, 1998.

[52] S. Rosenblat and S.H. Davis and G.M. Homsy, “Nonlinear Marangoni convection in bounded layers. Part 1. Circular cylindrical containers”, *J. Fluid Mech.*, **120**:91–122, 1982.

[53] T. R. Anthony and H. E. Clint, “Surface Rippling Induced by Surface Tension Gradients during Laser Surface Melting and Alloying”, *J. Appl. Phy*., **48**:3888-3894, 1977.

[54] A. K. Sen and S. H. Davis, “Steady Thermocapillary Flows in Two-Dimensional Slots”, *J. Fluid Mech*., **121**:163-186, 1982.

[55] S. M. Pimputkar and S. Ostrach, “Transient Thermocapillary Flow in Thin Liquid Layers”, *Phys. Fluids*, **23**:1281-1285, 1980.

[56] A. Zebib and G. M Homsy and E. Meiburg, “High Marangoni Number Convection in a Square Cavity”, Phys. Fluids, **12**:3467-3476, 1985.

[57] C. Cuvelicr and J. M. Driessen, “Thermocapillary Free Boundaries in Crystal Growth”, *J. Fluid Mech*., **169**:1-26, 1986.

[58] T. Yamamoto and Y. Takagi and Y. Okano and S. Dost, “Numerical investigation for the effect of the liquid film volume on thermocapillary flow direction in a thin circular liquid film”, *Phys. Fluids*, **25**:1-19, 2013.

[59] I. Ueno and S. Tanaka and H. Kawamura, “Oscillatory and chaotic thermocapillary convection in a half-zone liquid bridge”, *Phys. Fluids*, **15**:408–416, 2015.

[60] Y. S. Li and Z. W. Chen and J. M. Zhan, “Double-Diffusive Marangoni Convection in a Rectangular Cavity: Transition to Chaos”, *Int. J. Heat Mass Transfer*, **53**: 5223–5231, 2010.

[61] G. Chen and B. Roux, “An analytical study of thermocapillary flow and surface deformations in floating zones”, *Microgravity Q. 1*, **2**:73-80, 1991.

[62] H. C. Kuhlmann and C. Nienhu¨ser, “Dynamic free-surface deformations in thermocapillary liquid bridges”, *Fluid Dyn. Res*., **31**:103-127, 2002.

[63] J. Zhang and Y. Okano and S. Dost, “Numerical simulation of Marangoni convection in a shallow rectangular cavity with a linear solutal boundary condition”, *Int. J. Heat Mass Transf*., **178**:1-13, 2021.

[64] C. F. Chen and C. L. Chan, “Stability of Buoyancy and Surface Tension Driven Convection in a Horizontal Double-Diffusive Fluid Layer”, *Int. J. Heat Mass Transfer*, **53**:1563–1569, 2010.

[65] M. Stojanovic and H. C. Kuhlmann, “Stability of Thermocapillary Flow in High-Prandtl-Number Liquid Bridges Exposed to a Coaxial Gas Stream”, *Microgravity Sci. Technol*., **32**:953-959, 2020.

[66] M. Wanschura and V. M. Shevtsova and H. C. Kuhlmann and H. J. Rath, “Convective instability mechanisms in thermocapillary liquid bridges”, *Phys. Fluids*, **7**:912-925, 1995.

[67] Z. Kozhoukharova and S. Slavchev, “Computer Simulation of the thermocapillary convection in a Non-cylindrical floating Zone”, *J. Cryst. Growth*, **74**:236-246, 1986.

[68] V. M Shevtsova and H. C. Kuhlmann and H. J. Rath and L. Ratke and H. Walter and B. Feuerbacher, “Materials and Fluids Under Low Gravity”, *Springer, Berlin*, 323-329, 1995.

[69] W. R. Hu and J. Z. Shu and R. Zhou and Z. M. Tang, “Influence of liquid bridge volume on the onset of oscillation in floating zone convection I. Experiments”, *J. Cryst. Growth*, **142**:379-384, 1994.

[70] J. Masud and Y. Kamotani and S. Ostrach, “Oscillatory thermocapillary flow in cylindrical columns of high Prandtl number fluids”, *J. Thermophys. Heat Transf.*, **11**:105-111, 1997.

[71] V. Shevtsova, “Thermal convection in liquid bridges with curved free surfaces: Benchmark of numerical solutions”, *J. Cryst. Growth*, **280**:632-651, 2005.

[72] V. M. Shevtsova and J. C. Legros, “Oscillatory convective motion in deformed liquid bridges”, *Phys. Fluids*, **10**:1621-1634, 1998.

[73] Q. S. Chen and W. R. Hu and V. Prasad, “Effect of liquid bridge volume on the instability in small-Prandtl-number half zones”, *J. Cryst. Growth*, **203**:261-268, 1999.

[74] M. Lappa and R. Savino and R. Monti, “Three-dimensional numerical simulation of Marangoni instabilities in non-cylindrical liquid bridges in microgravity”, *Int. J. Heat Mass Transf.*, **44**:1983-2003, 2001.

[75] M. Lappa and S. Yasushiro and N. Imaishi, “3D numerical simulation of on ground Marangoni flow instabilities in liquid bridges of low Prandtl number fluid”, *Int. J. Numer. Methods Heat Fluid Flow*, **13**:309-340, 2003.

[76] K. Li and S. Matsumoto and N. Imaishi and W. R. Hu, “Marangoni flow in floating half zone of molten tin”, *Int. J. Heat Mass Transf.*, **83**:575-585, 2015.

[77] Y. Okano and M. Itoh and A. Hirata, “Natural and Marangoni Convections in a Two-Dimensional Rectangular Open Boat”, *J. Chem. Eng. Japan*, **22**:275-281, 1989.

[78] C. Jin and A. Sekimoto and Y. Okano and H. Minakuchi and S. Dost, “Characterization of the thermal and solutal Marangoni flows of opposite directions developing in a cylindrical liquid bridge under zero”, *Phys. Fluids*, **32**:1-11, 2020.

[79] Y. Takagi and Y. Okano and S. Dost, “A numerical simulation study on the effects of crucible rotation and magnetic fields in growth of SiGe by the traveling heater method”, *J. Heat Transfer*, **134**:1-7, 2012.

[80] M. Lappa, “Combined effect of volume and gravity on the three-dimensional flow instability in noncylindrical floating zones heated by an equatorial ring”, *Phys. Fluids,* **16**:331-343, 2004.

[81] M. Curak and N. Saranjam and S. Chandra, “Colour Variation in Drying Paint Films”, *J. Porgcoat.*, **136**:105173-105181, 2019.

[82] Y. Li and N. Imaishi and T. Azami and T. Hibiya, “Three-Dimensional Oscillatory Flow in a Thin Annular Pool of Silicon Melt”, *J. Cryst. Growth*, **260**:28-42, 2004.

[83] Y. R. Li and L. Peng and W. Y. Shi and N. Imaishi, “Convective Instability in Annular Pools”, *Fluid Dyn. Mater. Process*., 153-165, 2006.

[84] J. C. Chen and L. Zhang and Y. R. Li and J. J. Yu,” Three-Dimensional Numerical Simulation of Pure Solutocapillary Flow in a Shallow Annular Pool for Mixture Fluid with High Schmidt Number”, *Microgravity Sci. Technol*, **28**:49-57, 2016.

[85] J. C. Chen and Y. R. Li and J. J. Yu and L. Zhang and C. M. Wu, “Flow Pattern Transition of Thermal-Solutal Capillary Convection with the Capillary Ratio of -1 in a Shallow Annular Pool”, *Int*. *J. Heat Mass Transf.,* **95**:1-6, 2016.

[86] Q. Hu and Y. Ren and W. Liu and X. Chen and Y. Tao and H. Jiang, “Fluid Flow and Mixing Induced by AC Continuous Electrowetting of Liquid Metal Droplet”, *Micromachines*, **8**:119-134, 2017.

[87] N. Adkar and T. Yamamoto and Y. Takagi and Y. Okano and S. Dost, “Numerical Simulation of the Effect of Free Surface Shape on Marangoni Convection in a Liquid Film Sustained in a Circular Ring with Different Prandtl Numbers”, *Int. J. Microgravity Sci. Appl*., **33**:330309-330316, 2016.

[88] Weerakoon Rathnayake Neranjan Nayanajith and Agampodi Mendis Radeesha Laknath and Y. Okano and S. Dost, “Numerical Simulation Study of the Effect of Liquid Depth on the Stability of Thermal Marangoni Convection in a Shallow Cavity”, *J. Chem. Eng. Japan*, **55**:337-343, 2022.

[89] J. Zhang and A. Sekimoto and Y. Okano and S. Dost, “Numerical Simulation of Thermal-Solutal Marangoni Convection in a Shallow Rectangular Cavity with Mutually Perpendicular Temperature and Concentration Gradients”, *Phys. Fluids*, **32**: 102108-102120, 2020.

[90] C. Le and L. Liu and Z. Li, “Numerical investigation of the effect of rotation on the oscillatory thermocapillary convection and dopant transport in a silicon liquid bridge”, *J. Cryst. Growth*, **523**:1-10, 2019.

[91] M. Mundrane and J. Xu and A. Zebib, “Thermocapillary Convection in a Rectangular Cavity with a Deformable Interface”, *Adv. Space Res*., **16**:41-53,1995.

[92] M. Z. Saghir and R. Abbaschian and R. Raman, “Numerical Analysis of Thermocapillary Convection in Axisymmetric Liquid Encapsulated In-Bi”, *J. Cryst. Growth*, **169**: 110–117,1996.

[93] H. Minakuchi and Y. Takagi and Y. Okano and T. Nososko and S. Gima and S. Dost, “Three-dimensional Numerical Simulation of Thermal and Solutal Marangoni Convection in a Liquid Bridge under Zero-gravity Field”, *Trans. JSASS Aerospace Tech. Japan*, **10**:15-20, 2012.

[94] J. Zhang and Y. Okano and S. Dost, “Effect of radiative heat transfer on thermal-solutal Marangoni convection in a shallow rectangular cavity with mutually perpendicular temperature and concentration gradients”, *Int. J. Heat Mass Transf*., **183**:1-13, 2022.

[95] C. Le and L. Liu and Z. Li, “Oscillatory thermocapillary convection in deformed half zone liquid bridges of low Prandtl number fluids”, *Int. Commun. Heat Mass Transf*., **127**:1-11, 2021.

[96] M. Lappa, “Three-dimensional numerical simulation of Marangoni flow instabilities in floating zones laterally heated by an equatorial ring”, *Phys. Fluids*, **15**:776-789, 2003.

[97] M. Levenstam and G. Amberg, “Hydrodynamical instabilities of thermocapillary flow in a half-zone”, *J. Fluid Mech*., **297**:312-351, 1995.

[98] W. Shi and G. Li and X. Liu and Y. R. Li and L. Peng and N. Imaishi, “Thermocapillary Convection and Buoyant-Thermocapillary Convection in the Annular Pools of Silicon Melt and Silicone Oil”, *J. Supercond. Nov. Magn*., **23**:1169-1172, 2010.

ACKNOWLEDGMENTS

My study at the Okano Laboratory will soon end with the completion of my graduation thesis; I wish to express my sincere appreciation to all those who have offered me invaluable help at Osaka University.

First, I would like to express heartfelt gratitude to my supervisor, Prof. Yasunori Okano, who has offered me numerous valuable comments and suggestions with incomparable patience and encouraged me profoundly throughout PhD study. Completing this thesis was only possible with his painstaking teaching and insightful advice.

Secondly, I would like to thank Prof. Hisashi Minakuchi for his valuable comments and advice in my research on “Marangoni convection in a half zone with deformed free surface”. I must acknowledge Prof. Sadik Dost at the University of Victoria for carefully revising manuscripts, which improved my academic writing skills immensely.

I want to express gratitude to all my colleagues and friends in Japan, Dr. Radeesha Laknath Agampodi Mendis, who encouraged me throughout the period and also thanks to Dr. Jiangao Zhang, Dr. Yuto Takehara, Dr. Wang Liya, Dr. Kalum Chamara, Yuko Matsuzuki and other members of Okano Laboratory.

I am deeply indebted to my family, especially my wife, Dr. Imali Dissanayaka. Only with her selfless support, concern, and love can I overcome those difficulties and continue my studies. Her dedication and caring for my two sons are the sources of my strength.

The research work was financially supported by the Sigma Scholarship Foundation and Grant-in-Aid for Scientific Research (JSPS KAKENHI Grant No. JP20H00320) from the Ministry of Education, Culture, Sports, Science and Technology of Japan. The computational resources were provided by the Research Institute for Information Technology, Kyushu University, and Collaborative Research Program for Young Women Scientists provided by

the Academic Center for Computing and Media Studies, Kyoto University, and the Initiative on Promotion of Supercomputing for Young or Women Researchers provided by Information Technology Center, Tokyo University.

LIST OF PUBLICATIONS

[Papers]

- Neranjan Nayanajith Weerakoon Rathnayake, Radeesha Laknath Agampodi Mendis, Yasunori Okano, Sadik Dost: "Numerical Simulation Study of the Effect of Liquid Depth on the Stability of Thermal Marangoni Convection in a Shallow Cavity", *J. Chem. Eng. Japan,* **55**:337-343, 2022.

- Neranjan Nayanajith Weerakoon Rathnayake, Yasunori Okano, Hisashi Minakuchi, Sadik Dost: "A Numerical Simulation Study of the Effect of Deformed Free Surface on the Thermo-Solutal Marangoni Convection in a Shallow Cavity", *J. Chem. Eng. Japan,* **57**: 2421265, 2024.

- Neranjan Nayanajith Weerakoon Rathnayake, Yasunori Okano, Hisashi Minakuchi, Sadik Dost: "The Effects of Zone Volume and Gravity on Thermo-Solutal Marangoni Convection Instability in a Half-Zone Model of Float-Zone Growth of SiGe", *J. Chem. Eng. Japan*, **57**: 2364780, 2024.